THE STRONG TO WEAK COUPLING TRANSITION IN LOW MISORIENTATION ANGLE THIN FILM AND BULK $YBa_2Cu_3O_{7-x}$ BICRYSTALS

Nina F. Heinig

Under the supervision of Professor David C. Larbalestier

At the University of Wisconsin-Madison

High temperature superconductors, like $YBa_2Cu_3O_{7-x}$, show a transition from strongly to weakly Josephson coupled as the grain boundary misorientation angle increases. Low misorientation angle [001] tilt $YBa_2Cu_3O_{7-x}$ bulk scale and thin film bicrystals have been characterized by transport measurements in both low and high magnetic fields, and their properties compared to dislocation core overlap models of channel transport. Zero magnetic field measurements of the critical current density ratio, J_b/J_c, versus misorientation angle, θ, reveal that up to 7°, the best thin film bicrystals show almost no reduction in intergrain J_b with increasing angle. Above 7°, the data show a non-linear, exponential decrease in $J_b(\theta)$. The bulk scale bicrystals showed a slower decrease in J_b versus θ than the thin film samples. Nanovolt resolution voltage-current characteristics in large magnetic fields were used to identify strongly coupled components of the grain boundary. Measurements of the thin film bicrystals showed an intergrain irreversibility field, H*, that was essentially independent of θ up to 10°, and then showed

a rapid decrease between 10° and 15°, indicating the closure of strongly coupled channels in this angular region. Bulk scale bicrystals were not studied in such detail. However, strongly coupled channels clearly exist in a 14°[001] tilt bulk scale boundary. These results, along with the variation in electromagnetic properties between samples with the same misorientation angle, show that the present form of the dislocation core overlap model is inadequate to explain the data. Additional features of the grain boundary nanostructure must be introduced to explain the strong-to-weak transition in low angle $YBa_2Cu_3O_{7-x}$ grain boundaries.

Acknowledgements

There are many people who contributed to the work in this thesis. First of all, I would like to thank my advisor, Professor David Larbalestier, for his support and guidance throughout my graduate studies. I would also like to thank Dr. Debra Kaiser of NIST-Gaithersburg, for supplying the bulk scale bicrystals and for her hospitality when I spent the summer of 1993 at her laboratory; Dr. X.Y. Cai for introducing me to measuring the bulk scale bicrystals; Professor Susan Babcock, Dr. João Vargas, Na Zhang and I Fei Tsu, for their microstructural analysis of these bicrystal samples and patient explanations of what the images really meant; Ronald Redwing of Professor J.E. Nordman's group, who grew the thin film bicrystals, and explained the ins and outs of processing and Josephson junction behavior; Bruce Davidson, George Daniels, Ariane Holper, and Tuong Ngyuen, who also contributed to the progress of the thin film bicrystal studies; Alexander Pashitski and Dr. Anatolya Polyanski for their magneto-optic analyses of the films; Dr. Alexander Gurevich for helpful discussions; Bill Starch, Lloyd Lincoln, and Alexander Squitieri, for technical assistance and advice. In addition, I would like to thank past and present UW Applied Superconductivity Center members for their assistance, advice, and friendship.

TABLE OF CONTENTS

List of Tables

List of Figures

Chapter 1 : Introduction

In this chapter, the grain boundary coupling problem is discussed, as are the major results of previous bicrystal studies. The major microstructural models for low angle grain boundary coupling, and the current status of grain boundary microstructure investigations are outlined. Finally, the relationship of the electromagnetic measurements to the microstructure is discussed, and the motivation for the detailed electromagnetic characterization described in this thesis is presented.

Motivation

One of the biggest obstacles to bulk, high power applications of high temperature superconductors is weak superconducting coupling across grain boundaries of arbitrary misorientation angle. This weak-link problem is explored in this thesis by detailed study of the electromagnetic coupling across low angle $YBa_2Cu_3O_{7-x}$ [001] tilt grain boundaries as the misorientation angle, θ, increases from 0° to 20°. Over this angular range, the coupling changes from strong and single crystal-like to weak and Josephson junction-like. Both bulk scale flux-grown bicrystals and laser ablated thin-film bicrystals were measured to observe how θ, sample geometry, and processing affect the strong to weak coupling transition. In addition to electromagnetically characterizing the bicrystals, this thesis was part of a broader collaborative research effort studying the microstructural basis of the weak boundary coupling in the high temperature superconductors. The larger goal was to identify the microstructural features that degrade the superconducting properties at the grain boundary.

For bulk applications of superconducting technology, like magnets and high current carrying conductors, the most important properties of a superconductor are the critical current density, J_c, and the irreversibility field, H*. Within a single grain, the J_c is controlled by the flux pinning properties of the material. In polycrystalline $YBa_2Cu_3O_{7-x}$ (YBCO), weak electromagnetic coupling across grain boundaries (GBs), rather than the flux pinning properties, is the major factor limiting J_c. This transport J_c is defined by taking the measured critical current, I_c, and divided it by the entire cross-sectional area of the superconductor. Initial experiments by Dimos, Chaudhari and Mannhart [1] established that the J_c across thin film grain boundaries of YBCO was strongly dependent on the misorientation angle between the two crystals. Their data is summarized in Figure 1.1 and shows a rapid decrease in the GB critical current density, J_b, normalized by the intragrain J_c, with increasing angle. Later bicrystal thin film studies indicated that qualitatively similar behavior occurs in other high temperature superconductors (HTS), although the details differ between the different materials systems.

The magnetic field at which the entire type II superconductor is driven normal and vortices no longer exist discretely is called H_{c2}. For NbTi, $H_{c2}(4.2\text{ K}) \cong 10$ T [2], while for YBCO, $H_{c2}(4.2\text{K}) \cong 100$ T [3]. This large H_{c2} appears encouraging for high field applications of YBCO. However, it is not H_{c2}, but rather the irreversibility field, that defines the practical limitations of the superconductor. The irreversibility field, H*, is reached when a measurable voltage across the superconductor is generated at vanishingly small currents. Thus, H* defines a state for which there is no critical current and flux pinning is no longer effective. In the low temperature superconductors, H_{c2} and H* can be distinguished, although they are very nearly the same. In the HTS, H* and H_{c2} are substantially different. One attractive property of YBCO is that it has among the largest H*(T) values of any of the HTS.

The bismuth-based HTS, $Bi_2Sr_2CaCu_2O_x$ and $Bi_2Sr_2Ca_2Cu_3O_x$, have been the focus of most wire development research, because the grains' tendency to self-align allows for a good percolative supercurrent path. That this concentration on the bismuth HTS has occurred, despite relatively poor flux pinning and low H* values when compared to YBCO, indicates how detrimental weak coupling is to wire applications. Recently, however, there has been considerable success producing quasi-single crystalline thick films of YBCO on textured metal substrates with very high J_c values. These thick films can, in principle, be made in long lengths and consequently have the potential to be useful for high current applications. With a buffer layer between the nickel alloy and superconductor, and using ion beam assisted deposition (IBAD) to encourage grain alignment [4,5,6,7], a J_c(77K) of 0.9×10^6 A/cm^2 has been achieved. Another technique, rolling assisted biaxially textured substrates (RABiTS) [8] produces high J_c material by using a textured Ni or Cu substrate, an epitaxial layer of Pt, Pd, or Ag, and then the HTS layer, or a buffer and then a HTS layer. This technique yields J_c(77K) of 3×10^5 A/cm^2.

These accomplishments make a detailed understanding of how YBCO low angle grain boundaries affect current transport both scientifically and technologically interesting.

In order to better understand grain boundary coupling, this thesis describes low and high magnetic field measurements that were carried out on both bulk-scale and thin film YBCO bicrystals. Low field measurements were particularly useful for identifying any weak coupling behavior, while high field measurements studied how the irreversibility field changed with [001] tilt misorientation angle, θ. These results are then related to grain boundary microstructure by using a channel model of the grain boundary coupling.

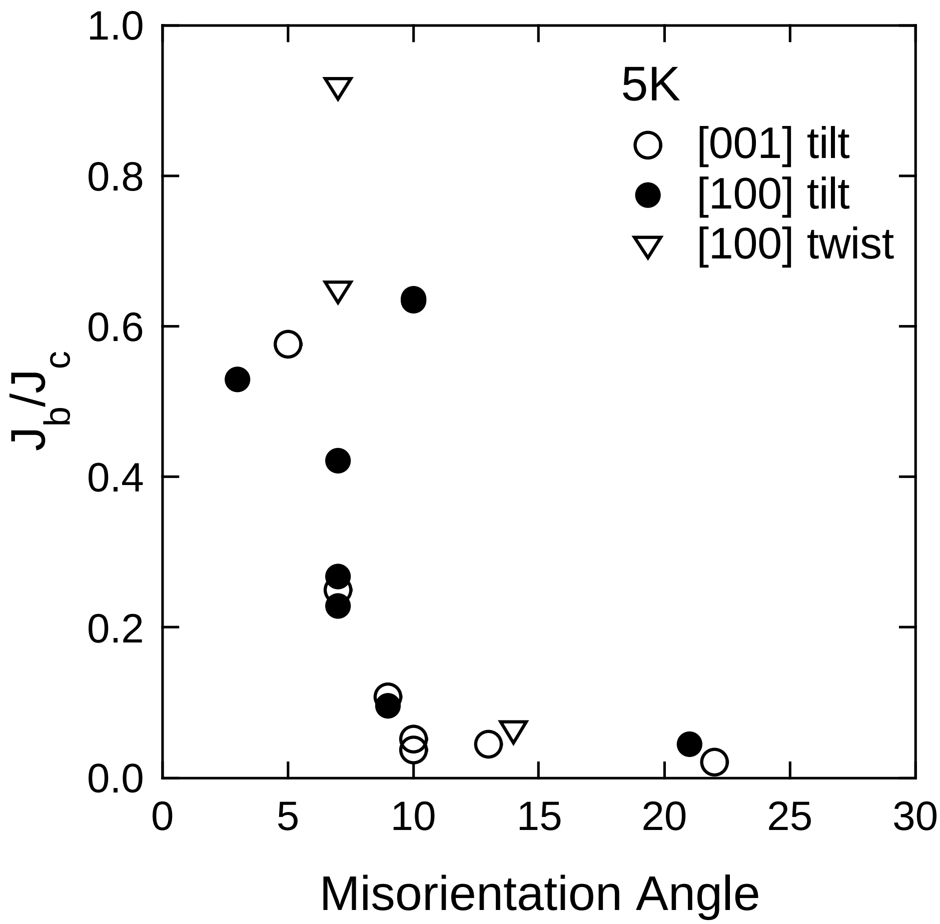

Figure 1.1 J_b/J_c versus grain boundary misorientation angle in $YBa_2Cu_3O_{7-x}$ /$SrTiO_3$ films at 5 K, from [1].

Previous Bicrystal Studies

The IBM bicrystal experiment [1] was of great interest to two different groups: those interested in bulk scale applications of HTS, and those interested in Josephson-effect based device applications. Most bulk-scale applications require high J_c values in large magnetic fields. Most Josephson device applications require large characteristic voltages (V_c, or I_cR_n), and strong sensitivity to small magnetic fields of less than a mT. Despite these disparate goals, both communities have a strong interest in understanding the nature of the grain boundary coupling in the HTS.

Dimos et al.'s experiment was on electron beam evaporated YBCO on $SrTiO_3$ bicrystal substrates. The substrates were made to be one of three types: [001] tilt, [010] tilt or [100] twist. These different GB orientations are illustrated in Figure 1.2, where the axes of the two crystals is given by [abc], and tilt or twist refers to the orientation of the GB plane with respect to the common axis of rotation. If the boundary plane is perpendicular to the common axis, it is a twist GB, while if the common axis lies in the boundary plane, it is a tilt GB. The GBs were also nominally symmetric, in that each crystal has the same misorientation with respect to the boundary plane. Assuming epitaxial growth of the YBCO onto the $SrTiO_3$, the critical current density can be measured with respect to all three types of misorientation angle. In Figure 1.1, the GB critical current density was measured at 5 K, and a rapid decrease in J_b with misorientation angle was seen. They also found that bicrystals with misorientation angles as low as 5° were sensitive to fields of much less than a mT, and otherwise appeared weakly coupled.

In the original electron-beam evaporated thin film bicrystals, the intragrain J_c was between 10^5-10^6 A/cm^2 at 4.2 K [1]. With time, there were major improvements in YBCO thin film quality, and intragrain J_c values of 10^6 A/cm^2 at 77 K became the standard. The group at Chalmers University in Sweden [9,10,11] repeated the YBCO work done by IBM, but used asymmetric yttria stabilized zirconia (YSZ) bicrystal substrates with [001] tilt GBs. They saw a rapidly decreasing J_b, now measured at 77 K, which decreased exponentially with θ between 0° and 45°. After some re-analysis, the IBM data also showed an exponential $J_b(\theta)$ [12]. The Chalmers group also saw curious "mixed" behavior in an 8° bicrystal [9]. The sample showed Shapiro steps under the influence of microwaves, typical of Josephson coupling, yet the bicrystal did not display the voltage-current characteristic, nor the magnetic field sensitivity of a true Josephson junction.

Additional measurements by other groups [13] confirmed the general exponential decrease in $J_c(\theta)$ seen in YBCO films, and in all cases clear signs of weak coupling were observed when $\theta \geq 10°$. Work was done to study [001] tilt film bicrystals of $Bi_2Sr_2CaCu_2O_x$ (Bi-2212) [14,15] , $TlBa_2Ca_2Cu_3O_x$ (Tl-1223) [14,16,17], $Tl_2Ba_2CaCu_2O_x$ (Tl-2212) [17], and $Tl_2Ba_2Ca_2Cu_3O_x$ (Tl-2223) [18]. While the number of misorientation angles studied was often small, a rapid decrease in J_b with θ was observed in all the HTS bicrystal films studied.

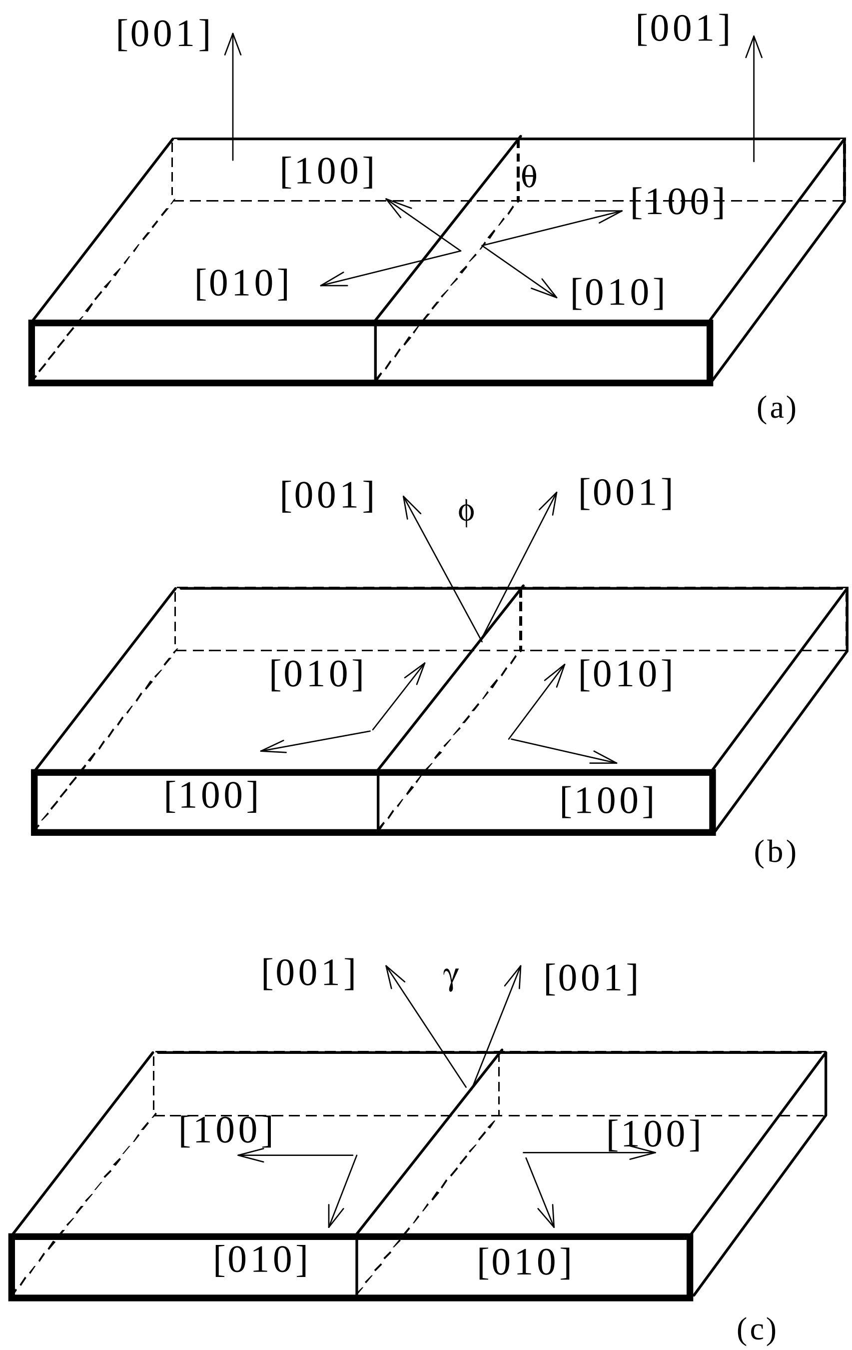

Figure 1.2 Bicrystal Misorientation Relationships: (a) [001] tilt, (b) [010] tilt, (c) [100] twist.

In addition to studying the low-to-high angle transition, considerable work has been done on a closely related problem: the precise nature of the weak coupling in high angle YBCO thin film junctions. The problem of whether the GB junction is SIS (superconductor-insulator-superconductor), SNS (superconductor-normal metal-superconductor), arrays of Dayem bridges (weak point contacts), or some more exotic combination like SNINS (superconductor-normal metal-insulator-normal metal-superconductor) is particularly relevant for developing HTS Josephson devices. The consensus in the literature [19,20,12,21,22] is that the electromagnetic properties remain spatially inhomogeneous, even in high misorientation angle junctions. Electromigration and $J_b(H)$ Fraunhofer oscillation studies [19,20] of high angle YBCO/MgO grain boundaries were construed to indicate that these GBs consist of weakly superconducting filaments in parallel with non-superconducting ohmic regions. This model of random shorts in high angle boundaries was proposed by Buhrman's group at Cornell. A similar model, proposed by Gross and Mayer [23,24,25], suggested that the observed junction properties were due to resonant tunneling produced by a large density of localized defect states in the dielectric barrier of the grain boundary. This model postulates a continuous inhomogeneous insulating barrier at the GB, with the resonant tunneling leading to the equivalent of a parallel path of resistive normal metal. The resonant tunneling path allows for proximity effect superconducting coupling across the GB.

Although most thin film bicrystal studies focused on low magnetic field properties, there have been some previous studies of thin film YBCO bicrystals in large magnetic fields [26,27,28]. The IBM group [26,27] found that even high angle, nominally weakly coupled thin film bicrystals had a residual critical current that persisted in fields of 5 Tesla at 4.2 K. They also found that the critical current density was dependent on magnetic field history, becoming much larger after ramping to high fields. Fröhlich et al. [28] studied the weakly coupled behavior of 24° thin film YBCO bicrystals, observing Josephson-like $J_b(H)$ oscillations in applied fields of up to 12 Tesla at 4.2 K.

In bulk scale bicrystal studies, the experiments are most often done in large magnetic fields of several Tesla. The primary reason for this is that the strong, not the weak coupled, behavior of the GB is of the greatest interest. Bulk scale applications depend on parameters like H*, which cannot be determined from zero field data. At UW-Madison, research has been done on the properties of bulk scale, flux-grown YBCO bicrystals [29,30], and one significant result was that most bicrystals with a misorientation angle of 90° between the c-axes appear strongly coupled. This was confirmed in later work on a-axis oriented films [31]. A more recent result [32] was the discovery of vortex matching effects in several weakly coupled bulk bicrystals. Peaks in J_b were observed in magnetic fields on the order of a Tesla, corresponding to the GB facet spacing subsequently seen during microstructural analysis.

These bicrystal experiments show that there is still much to be learned about the strong-to-weak coupling transition in YBCO grain boundaries. How do the strong-to-weak transitions in thin film and bulk bicrystals compare? How does the "residual current" seen at high θ and high fields by the IBM group change as the misorientation angle is decreased? What microstructural models of the grain boundary are consistent with the observed electromagnetic behavior? Developing a consistent microstructural model that explains the grain boundary coupling behavior requires comprehensive and detailed electromagnetic measurements in conjunction with microstructural analysis.

Channel Conduction Models

In the original IBM study [1], it was proposed that the decrease in J_c with misorientation angle was due to grain boundary dislocation (GBD) cores disrupting the supercurrent. The GBD density increases with misorientation angle, and above a critical misorientation angle, θ_c, the GBD cores would overlap, producing a continuous layer of "bad" material, capable of supporting only weak coupling. A later paper by Chisholm and Pennycook [33] extended this model to include the strain fields surrounding the GBD cores as also being disruptive to the coupling, proposing that the GBD strain fields drove out oxygen.

The GBD core model hypothesizes that, up to some critical misorientation angle of about 5-10°, the critical current across the boundary will decrease with increasing θ, as the channels of good superconductor between the cores become smaller. This model predicts that the inter- to intra-grain critical current density,

$$J_b/J_c = (D - 2r_m)/D, \qquad \text{Equation (1.1)}$$

where the dislocation spacing, $D = |\mathbf{b}|/(2\sin(\theta/2))$, and r_m is the effective dislocation core radius. In the low angle limit, this simplifies to,

$$J_b/J_c = 1 - 2r_m\theta/|\mathbf{b}| \qquad \text{Equation (1.2)}$$

The dislocation spacing is derived from Frank's formula, and depends only on the Burgers vector, **b**, which is obtained from analysis of high resolution transmission electron micrographs of the grain boundary. The core radius, r_m, depends on the electrical cross-section of the dislocation core, and is not known a priori. Conventionally, however, the core radius of a GBD is taken to be ≈ |**b**|. Consistent with this, Gao et al. [34] analyzed high resolution transmission electron micrographs of well separated GBDs in thin film YBCO, and found the cation disordered region to be about 0.5 nm in radius.

The channel models [1,33] of low angle GBs consist of strong and non-superconducting segments in parallel, and do not include the contributions from weak coupling across the two superconducting grains. If the size of a "good" channel is close to the coherence length, only weak point-contact coupling should occur. In addition, if the "bad" channel is a normal metallic conductor, and not an insulator, proximity effect coupling will occur, allowing the "bad" channel to carry a significant supercurrent. A recent paper by E.Z. Meilikhov [35] also indicates that the summation of the quasi-periodic strain fields due to the GB dislocations can vary considerable depending on how ideally the GBDs are spaced along the boundary. These effects complicate simple correlations between the microstructure and the electromagnetic properties.

Microstructural Results

In the HTS, the superconducting characteristic lengths, the penetration depth, λ, and the coherence length, ξ, are quite small. In YBCO, $\lambda_{ab}(0) = 150$ nm, $\xi_{ab}(0) = 2$ nm, and $\xi_c(0) = 0.4$ nm, while in NbTi, $\lambda(0K) = 300$ nm and $\xi = 4$ nm [36]. Thus, compared to conventional low temperature superconductors, very small microstructural features can affect the superconducting properties in the HTS.

Extensive microstructural studies have been done on both thin film and bulk YBCO grain boundaries. The theme that emerges is that the grain boundaries are heterogeneous on many length scales, including length scales comparable to λ and ξ. Low angle, high symmetry YBCO GBs, like those studied in this thesis, are particularly well suited to microstructural analysis, since it is possible to image both grains simultaneously in the transmission electron microscope, making it possible to directly image and analyze the GBDs that subdivide the boundary.

Flux Grown Bicrystals

Within our Materials Research Group, extensive studies of the grain boundary microstructure in flux-grown bulk bicrystals have been done by I Fei Tsu, Na Zhang, João Vargas, and Prof. S.E. Babcock. They found evidence of heterogeneity on both the micro- and nanometer scale. The majority of boundaries were free of any second phase, and appeared very narrow (less than 1 nm) in high resolution transmission electron microscopy (HRTEM). In a comprehensive cataloging effort, primarily carried out by Na Zhang, polarized light microscopy showed the bulk bicrystals have macroscopically curved or faceted boundaries, both in the a-b plane, and along the c-axis.

Chemical composition variations across and along YBCO grain boundaries have been studied by high spatial resolution techniques like STEM-EDX (Scanning transmission electron microscopy - energy dispersive x-ray spectroscopy) and PEELS (Parallel electron energy loss spectroscopy) [37]. Copper enrichment and oxygen depletion at the GB have been observed, as well as quasi-periodic composition variations along the boundary. STEM-EDX studies of the GB composition variations of a near 7° [001] tilt bulk bicrystal [38] show enhanced Cu signal and increased strain contrast at positions along the GB with an average spacing of about 70 nm. The boundary was faceted along the (110) and (100) planes, and the enhanced Cu and strain contrast corresponded to the positions of the shorter facets.

While it is well known that the superconducting properties of YBCO depends strongly on the oxygen deficiency, oxygen is difficult to measure using most high spatial resolution techniques. PEELS was used to determine the local oxygen content across the GB [39] by observing the local hole depletion. Both low and high angle GBs were oxygen depleted when compared to the bulk, although the high angle, weakly coupled GB appeared to have a wider oxygen depleted region. PEELS data taken along, rather than across, the GB showed the oxygen content could be highly variable as the position along the boundary changed.

Since the supercurrent can be disrupted by features on the order of the coherence length, ξ, microstructural characterization of the GB on the nanometer and sub-nanometer scale is essential to identify the features that cause weak coupling. A recent paper by I F. Tsu et al. [40] on the GB topography and GB dislocation networks of a low angle bulk 6° [001] bicrystal illustrates how complex are even such nominally simple boundaries. This boundary was faceted, with facet planes of lengths in the tens of nanometers. Further sub-faceting of some of these facet planes was observed, with sub-facet lengths of a few nanometers. Strong strain contrast, stronger and larger than that seen at individual GB dislocations, was seen at the facet junctions. Several different kinds of GBDs were observed, and their spacing was not constant, but varied with position along the facet plane. The most common type of GBD was a partial GBD with Burgers vector, $\mathbf{b}$ = 1/2[110], which has $|\mathbf{b}|$ = 0.27 nm. These dislocations are formed by the dissociation of a primary GBD into two partial GBDs separated by a stacking fault. This complex GBD and strain field structure means that simplistic structural models that correlate the microstructure and electromagnetic character may be inadequate.

Some of these above features can be seen in Figure 1.3, where a HRTEM image of a 10° bulk scale bicrystal is shown. The partial dislocations with $\mathbf{b}$ = 1/2[110] are well separated, and calculating $D = |\mathbf{b}|/(2\sin(\theta/2))$ gives a GBD spacing, D = 1.55 nm, which appears close to the average of the observed dislocation spacings.

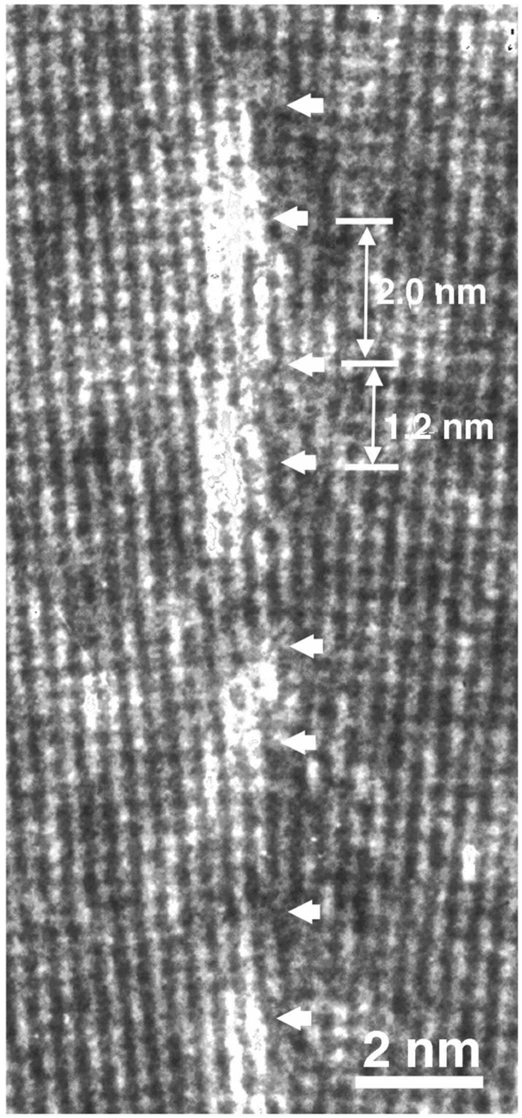

Figure 1.3 A high resolution transmission electron micrograph of a 10° bulk scale bicrystal. The arrows indicate the locations of the GB dislocations, with b = 1/2[110]. Courtesy I Fei Tsu.

Thin Film Bicrystals

The GB microstructure of epitaxial films grown on bicrystal substrates may seem more ideal than flux grown, bulk bicrystals, given that both θ and the macroscopic boundary plane can be pre-determined. However, all microstructural studies have found the film boundary plane meanders considerably from that of the substrate boundary, resulting in a microscopically “wavy” boundary [41,42,43,44]. This “wavy” morphology appeared in all the YBCO films examined, regardless of substrate or deposition technique. Similar to what has been seen in bulk scale bicrystals, extensive GB faceting with associated extended strain fields, and cation non-stoichiometry at dislocations have been observed in YBCO/MgO films by Gao et al. [34]. Because thin film GBs are “wavier” than flux-grown bulk GBs, they are more heavily faceted, and the facet junction strain fields may be proportionately more important to the transport properties of thin film bicrystals. However, the transport properties very clearly depend on misorientation angle, and thus far, the relationship between the facet strain fields and misorientation angle is unclear.

In our low angle YBCO/STO bicrystal thin films, the film boundary was also observed to wander from the grain boundary plane established by the substrate bicrystal. This can be seen in Figure 1.4, where a HRTEM micrograph of a 10° thin film bicrystal is shown. The arrows indicate the grain boundary dislocations, which appear to be dislocations with Burgers vector, **b** = [100] or **b** = [010]. As discussed in I Fei Tsu’s thesis [45], the narrow spacing of the {200} lattice spacing means that it is not possible to distinguish if these primary dislocations have further dissociated into two partial dislocations. By using the Burgers vector of these primary dislocations in Frank’s formula, one calculates a dislocation spacing, D = 2.24 nm for $\theta = 10°$, and if they have dissociated into partial dislocations of **b** = ½[100], one calculates a dislocation spacing of

D = 1.12 nm. It is important to note that both these dislocation spacings are different from that observed for the 10° bulk bicrystal in Figure 1.3, for which **b** = ½[110], and the dislocation spacing was 1.55 nm.

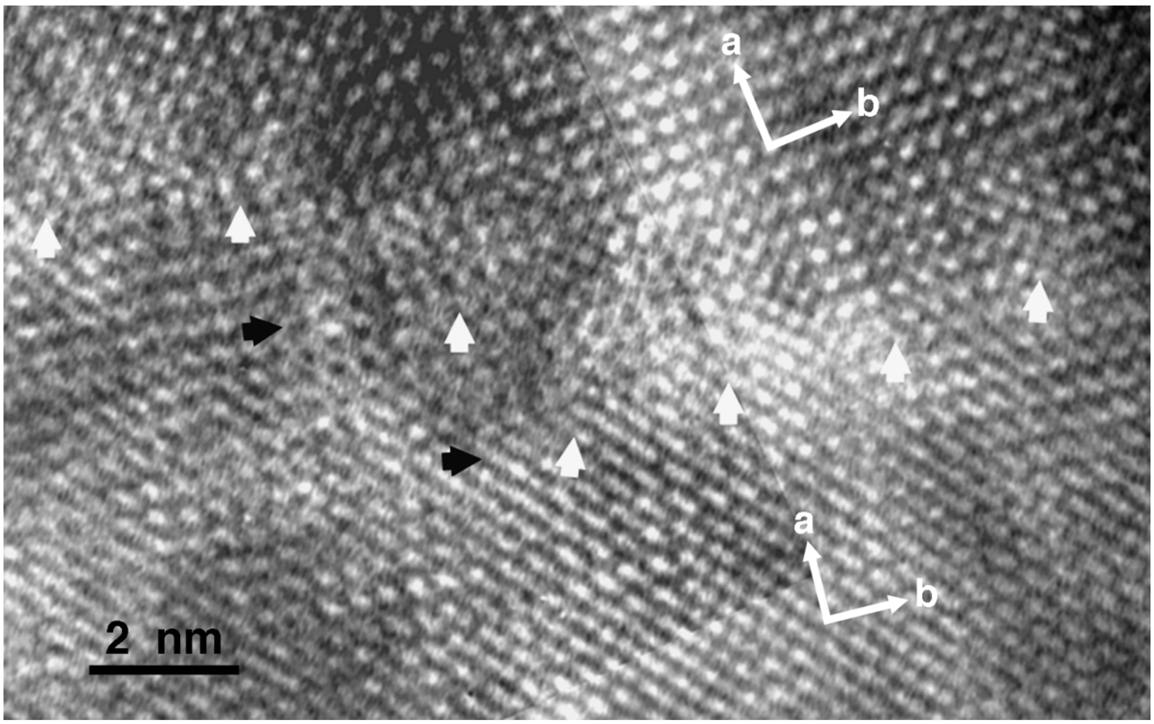

Figure 1.4 A high resolution transmission electron micrograph of a 10° thin film grain boundary. The arrows indicate the positions of the GB dislocations. Courtesy I Fei Tsu.

Another area of investigation is the microstructure of the thin film intragranular, single crystal regions. Unlike bulk scale, flux grown material, YBCO films have very high zero field J_c values, and a number of groups have studied single crystal film growth and microstructure to determine the reason for these high J_c values. Studies of the initial formation and evolution of film morphology indicate that YBCO films grow by island nucleation [46,47]. Scanning tunneling, and atom force microscopy of sputtered films on

MgO and STO show a clear spiral growth morphology [48]. Growth spirals of this sort form around screw dislocations, and these dislocations have a spacing of approximately 100-400 nm. This spacing appears too large for these dislocations to be the only pinning centers. There are additional microstructural analyses in the literature [49, 50], showing the presence of Y_2O_3 nanoparticles, and diffusion of Sr and Ti in laser ablated YBCO films on $SrTiO_3$ [51]. These features may also act as pinning centers, accounting for the higher critical current densities found in the films. While no evidence has yet been seen, it appears likely that these impurities and second phase nanoparticles would segregate preferentially to the thin film grain boundaries.

Summary

The problem of weak coupling at grain boundaries is a very important one, both for the development of HTS applications, and for a basic understanding of these novel materials. From the beginning, the short superconducting characteristic lengths, λ and ξ, and the complex chemistry of these materials have suggested that inhomogenieties along the grain boundary would play a key role in controlling the properties, and microstructural studies have reinforced this viewpoint. By measuring the properties of low angle YBCO grain boundaries as the misorientation angle increases, an in-depth study of the transition from strong to weak coupling is possible. By looking at two very different forms of YBCO; flux-grown bulk scale bicrystals, and thin film bicrystals, the effects of geometry and growth mode on the grain boundary coupling can be clearly seen. At present, grain boundary dislocations appear a likely source for the disruption in the supercurrent across low angle grain boundaries, although the specific relationship between the grain boundary microstructure and transport properties remain unclear.

Chapter 2 : Sample Growth and Processing

The two types of $YBa_2Cu_3O_{7-x}$ samples studied are bulk scale bicrystals grown from a Cu-rich flux, and pulsed laser ablated bicrystal films grown on $SrTiO_3$. The different growth modes of these samples lead to significant differences in the microstructure and electromagnetic properties of both the intragrain and intergrain regions. In this chapter, growth and processing of the samples are outlined, with particular emphasis on how the two types of samples differ from each other.

Bulk Scale Bicrystals

Growth

The bulk scale $YBa_2Cu_3O_{7-x}$ bicrystals were provided by Dr. Debra Kaiser of NIST-Gaithersburg [52,53], using a method in which free standing bulk bicrystals form from a mixture of high purity (Johnson Mathey Spectrapure) sintered $YBa_2Cu_3O_{7-x}$, CuO, and $BaCuO_2$. The 1.5 gram mixture is heated in Au crucibles to about 985°C in air, cooled to 950°C at 5°C/hour, and then slowly cooled to 830°C at 2°C/hour. Liquid creeps along the inner and outer walls of the crucible, and regular rectangular crystals form where the Cu-rich flux flows away from the growing crystals. Single crystals, bicrystals, and multicrystals are all produced in these growth runs. The c-axes of the bicrystals are usually aligned, and the crystals range in size up to about $1000 \times 1000 \times 200\ \mu m^3$.

When the bicrystals are observed under polarized light, many twin boundaries are obvious. Twin boundaries occur when the a and b axes of the crystal switch. They form to relieve the distortion that occurs when YBCO undergoes the tetragonal to orthorhombic transition at approximately 540°C. Photographs of the twin boundary misalignment were used to estimate the misorientation angle, θ, of the [001] type bicrystals, with an accuracy of about 1°. The c-axis misalignment is typically less than 2° or 3°, and θ can be known to $\pm$ 2°. Determining θ to better than 2° is not possible because the large number of twin boundaries in each crystal leads to variations in θ as one moves along the grain boundary. Because of the different lengths of the a and b axes, the twin domains are misoriented by 89°. Thus, the bicrystal misorientation angle varies along the grain boundary depending on which orientation of twin domain in each crystal intersect at the grain boundary.

The as-grown bicrystals are oxygen deficient. They are annealed for 150 hours at 420°C in high purity flowing oxygen in order to maximize T_c. However, these highly perfect crystals have very slow oxygen uptake kinetics [54,55,56], and may still not be fully oxygenated even after this extensive annealing time.

Processing

After annealing, selected bicrystals were ground and polished flat, mounted on an unpolished sapphire substrate, and the current and voltage leads were applied with Ag epoxy (Amicon C-850-5A). Not all the bicrystals were ground and polished before measuring. Gold or silver wires, 25 μm or 50 μm in diameter, were used to make contact to these very small samples, and 100 μm Ag wire was used to connect these wires to the measurement rig. The epoxy was cured for 5 to 10 minutes on a hot plate set at approximately 300°C, and then cured for another hour in flowing oxygen at 420°C to reduce the contact resistance.

Figure 2.1 shows a bicrystal that has been wired for measurement. The current leads should be placed on a face perpendicular to the a-b planes, so that current is injected into all the a-b planes as evenly as possible. As is clear from the figure, the irregular position of the measurement leads means that current percolation and distribution effects will be a concern during measurement [57,58,59].

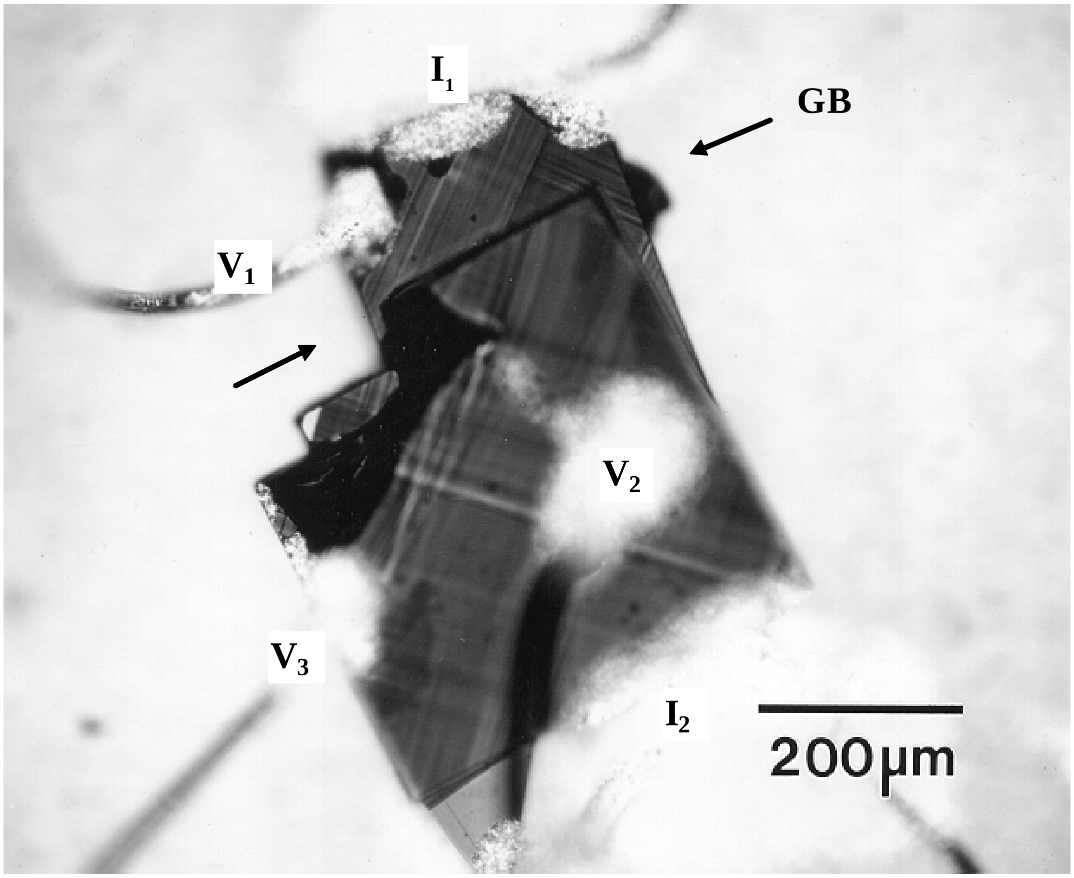

Figure 2.1 A 4° [001] tilt bulk bicrystal, showing 3 voltage and 2 current leads.

Thin Film Bicrystals

Growth

The thin film YBCO bicrystals were grown by Ronald Redwing in Prof. J.E. Nordman's group, using pulsed laser ablation onto $SrTiO_3$ (STO) bicrystal substrates purchased from the Shinkosha Co. [i]. Pulsed laser ablation is a relatively fast and cost effective way to produce high quality oxide films. The method also allows one to oxygenate the films in-situ. Optimization of J_c and T_c was carried out on single crystal substrates of $LaAlO_3$ and STO before any bicrystal films were deposited.

$LaAlO_3$ (LAO) is a good lattice match to YBCO [60], and high quality YBCO/LAO films can be produced. LAO substrates are much cheaper than STO substrates, but they are heavily twinned, and LAO bicrystal substrates are not commercially available. Potential bicrystal substrate materials include yttria-stabilized ZrO_2 (YSZ), STO, and MgO. However, the YBCO/YSZ combination produces interfacial layers between the substrate and film, and the lattice match between MgO and YBCO is rather poor, so STO bicrystal substrates were chosen for this study.

The as-bought STO bicrystal substrates were 1x1 cm, and were cut into smaller pieces before growth. The samples for electromagnetic characterization were cut to be 1x0.5 cm, and the samples for transmission electron microscopy and magneto-optic investigation were cut to be 1x0.25 cm. Before being sliced by a wafer saw, the polished side of the substrate was protected by a layer of photoresist, and the substrates were mounted on a graphite block with wax. After cutting, the substrates were thoroughly cleaned before being put into the ablation chamber. Hot (50°C) acetone, photoresist stripper, de-ionized water, acetone, and isopropyl alcohol were sequentially used to clean the substrates before growth.

As illustrated in Figure 2.2, film growth by pulsed laser deposition is conceptually simple. A pulsed laser beam is focused onto a sintered target of YBCO, vaporizing tens

---

[i] through Nikko HiTech International, Inc., San Jose, CA 95110; tel. (408) 894-1115.

of nanometers of surface material, which form a “plume” of atoms, ions, and molecules. The “plume” deposits material onto the substrate, which is kept at a temperature of approximately 730-760°C, allowing the plume to rearrange to form an epitaxial layer of YBCO. The KrF laser system operates at 5 Hz and a wavelength of 248 nm. The temperature is controlled with heat lamps, and an optical pyrometer monitors the temperature of the substrate faceplate, outside the range of the plume. The temperature read by the optical pyrometer, T_{op}, is somewhat higher than the actual substrate temperature, because of the temperature gradient between the faceplate and the substrate. Ablation takes place in an oxygen environment of a few hundred mTorr, ensuring a fully oxygenated film without a separate oxygen anneal. After growth, the films are cooled to room temperature in about an hour and a half, in 800 Torr of oxygen.

In practice, this apparently simple process can be difficult to carry out. The main factors controlling film quality are substrate temperature, substrate-to-target distance, and oxygen pressure. Other factors include laser fluence, laser-spot uniformity, target quality, vacuum system quality and time spent at growth temperature. Poor control over any of these can lead to non-stoichiometric, non-epitaxial, or contaminated films.

One difficulty that we had with bicrystal film growth was getting the substrates off the faceplate after growth. Initially, Ag epoxy was used to fix the substrates to the faceplate, so that they were in good thermal contact during growth. However, very often the epoxy would set so strongly that it would be impossible to get the bicrystals off the faceplate without breaking them. Adjusting the epoxy composition by the addition of ~

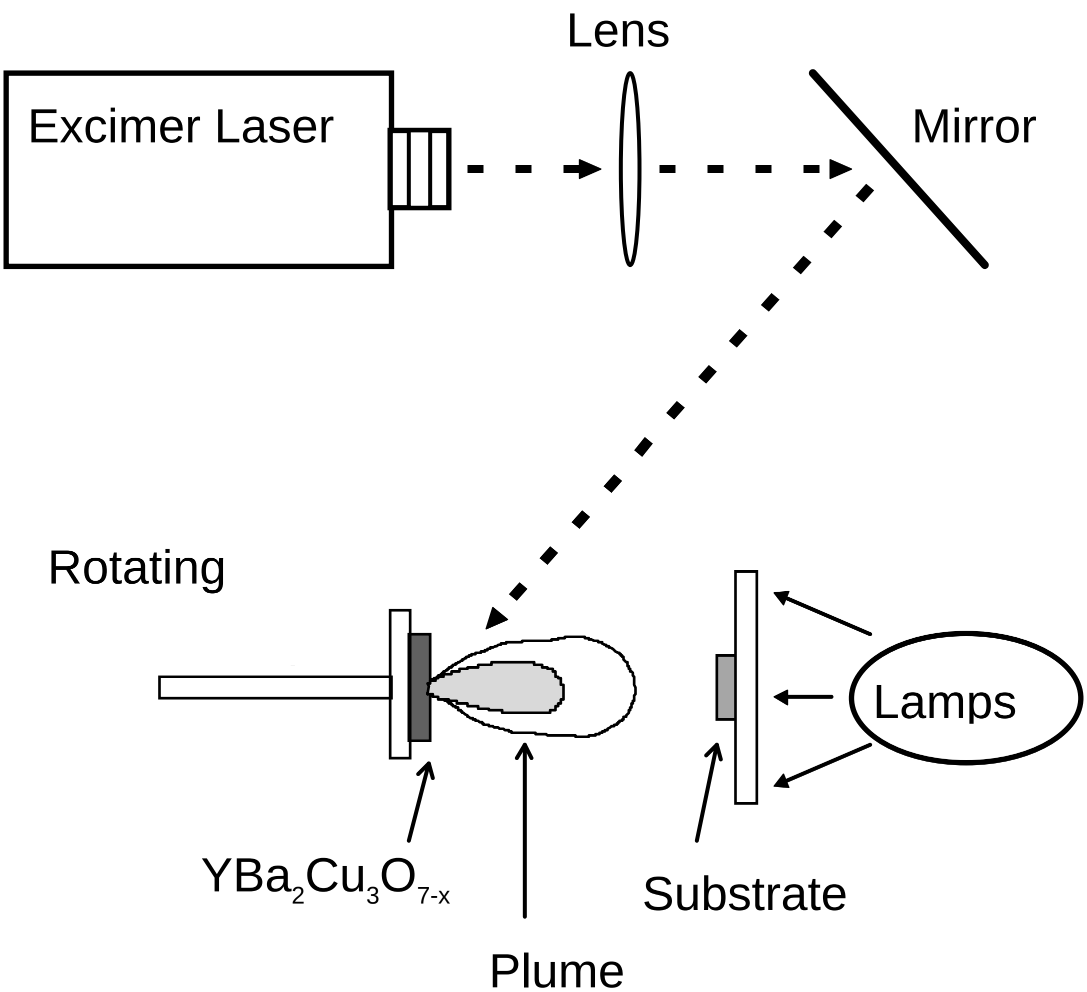

Figure 2.2 Diagram of the pulsed laser ablation growth arrangement.

10 μm Ag flake and n-butyl acetate often helped, but not consistently. Eventually, a clamping system was introduced. Inconel clamps held the substrate onto the faceplate, and Au foil was put between the faceplate and substrate to improve thermal contact. This worked well and eliminated substrate breakage. However, the degree of thermal contact between substrate and faceplate seemed a little less reproducible with the clamping arrangement. Both bicrystals grown with Ag epoxy, and those grown with clamps are included in this study.

Processing

After growth, the films were patterned in order to make well-defined links for measurement. Using Ag epoxy to attach the leads, as was done with the bulk samples, would be too damaging to these more delicate films, and would also limit the number of times a film could be measured before the epoxy and contact wire ripped off. The goal in patterning the bicrystals was to produce reliably reproducible circuits, while limiting damage to the films.

Contact pads were first made by sputtering Au onto the bicrystals. The pads were defined, and the grain boundary and intragrain link region were protected, by a stainless steel shadow mask. To improve the adhesion of the Au, a surface layer of YBCO was removed by ion beam milling before sputtering the Au. To minimize heating damage during milling, the films were cooled to approximately -25°C, by flowing liquid nitrogen through the Cu sample holder.

The films were patterned using either AZ1350 or AZ5214 photoresist. After spinning the photoresist onto the sample, it was cured by heating to 90°C for 30 minutes in a forced air oven. After photolithographic patterning, the photoresist was developed using water-based developer, and excess YBCO was removed by ion beam milling. The photoresist protected the test links from contact with the developer. After ion beam milling, the remaining photoresist on the film was removed by ultrasonic cleaning in either acetone or n-butyl acetate, and finally, the film was rinsed in isopropyl alcohol.

The pattern designed for the high field superconductor property evaluation consisted of 18 contact pads and 6 test links. This pattern is shown in Figure 2.3. The entire pattern is seen in Figure 2.3(a), and Figure 2.3(b) shows an enlargement of the grain boundary region. One link was reserved to test the intragranular properties of the film, and it was 10 μm wide with 500 μm between the voltage leads. The other five intergranular links were all 100 μm between the voltage leads. Different intergranular links had different widths: 5 μm, 10 μm, 20 μm, 50 μm and 100 μm. This was done so that a reasonably large value of the critical current could be measured for all the bicrystals, despite the expectation that the critical current density would vary by several orders of magnitude over the angular misorientation range studied. The pattern was designed so that current and voltage leads could be separated, so that even if different links used some of the same contact pads, the current pads would not be used as voltage pads, and vice versa. This was because the wires leading to the sample in the high field magnet testing rig were twisted together to reduce inductive pick-up. Twisting current and voltage wires together could lead to the current wires warming the voltage wires, inducing thermal voltages in the voltage leads. Since a significant component of the electromagnetic testing was to measure the extended electric field - current density characteristics from the nV level, this was an important consideration.

To make electrical contact to the patterned bicrystals, Pogo™ pins, spring-loaded contact pins, mounted in a phenolic head, were used. The spring mechanism inside the pins were found to be made from a magnetic nickel based alloy, which often led to residual fields of about 0.1 mT. Degaussing the measurement rig before each low field measurement made it possible to reduce the residual field to a few hundredths of a mT. The magnetic pins did not seem to affect the high magnetic field measurements.

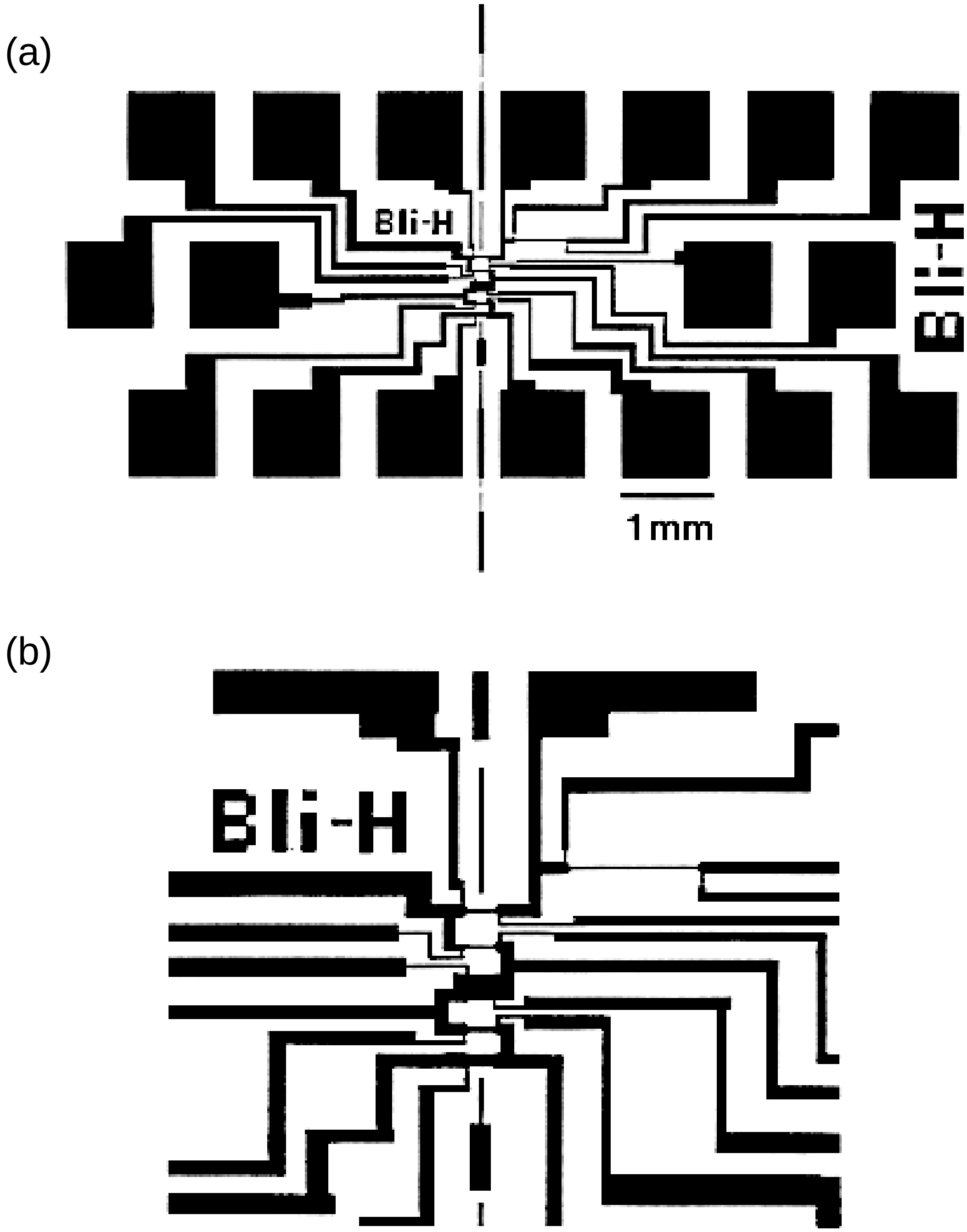

Figure 2.3 Bicrystal film pattern, including 6 possible measurement links, where the upper figure is the entire pattern, and the lower is an enlargement of the GB region.

Comparing Bulk and Thin Film Bicrystals

Although all the experiments discussed in this thesis involve nominally [001] tilt YBCO bicrystals, it should be noted that there are significant differences between bulk scale and thin film samples. Bulk scale bicrystals are slowly grown, and their grain boundary structure should be significantly closer to equilibrium than the thin films. In addition, because of the growth method, and the much larger sample thickness, impurity segregation to the GB is less likely to occur. In this sense, bulk scale bicrystals are more “ideal” than the thin films in that they more closely approximate idealized GB microstructures.

However, because the growth of the bulk scale bicrystals is unconstrained, each bulk bicrystal has a unique geometry and macroscopic GB plane, leading to different lead arrangements on each sample. These differences in GB cross sectional area and percolative path effects in the transport current make precise comparisons between bulk samples difficult.

In contrast, thin film bicrystals are highly engineered materials that are grown in a short time. They are therefore unlikely to be close to equilibrium. They are also susceptible to contamination from the substrate and from other environmental factors. Despite this, the thin film bicrystals have a number of advantages. Because the film geometry is constrained by the substrate, the macroscopic GB plane is fixed. The lead arrangement problem does not occur in thin films, because each thin film bicrystal has the same pattern of current and voltage pads, and a well defined current path. Comparisons between different samples, and between intragrain and intergrain properties, are thus more quantitative than for bulk bicrystals.

Chapter 3 : Low Magnetic Field Characterization

Introduction

Both the bulk scale and the thin film bicrystals were measured in low magnetic fields by resistance versus temperature (R-T), by voltage versus current (V-I), and by current or voltage versus field (I_c-H). The bicrystal measurements were done in close collaboration with Dr. X.Y. Cai, who extensively characterized the higher angle bulk bicrystals, and R.D. Redwing, who carried out detailed low field characterization of the high angle thin film bicrystals, such as measuring $J_b(T)$.

In this chapter, the bulk scale bicrystal low field experiments are discussed, and the results of the low misorientation angle dependence of J_b are compared to the predictions of the dislocation core overlap models.

For the thin film bicrystals, this chapter contains an overview of both the film (intragranular), and the grain boundary (intergranular) properties. The ratio of the grain boundary J_b to that of the film J_c is plotted versus misorientation angle, and is compared to dislocation core overlap models. Finally, the low field properties of the bulk scale and thin film bicrystals are compared and contrasted, and the implications are discussed.

Bulk Scale Bicrystals

Experimental Details

The bulk bicrystal measurement rigs consisted of a Cu-mounting block, a heater, a Si-diode thermometer, and 6 measurement leads. A copper magnet provided small magnetic fields of up to 20 mT. The sapphire substrate, with sample, was mounted onto the copper block with silver paint, with magnetic field applied parallel to the c axes of the bicrystal. Current was supplied by a 2 Ampere bipolar operational amplifier (BOP) power supply, and voltage was measured using a Keithley 150B nullmeter. The 150B had a sensitivity of about 0.25 μV. Later equipment improvements allowed for nanovolt level sensitivity, but this did not occur until after most of this data had been collected. The data was collected on an Amiga personal computer, using the *Chart* program written by J. McKinnell.

One type of measurement was resistance versus temperature (R-T). A constant measuring current, either ac or dc, of between 0.1-1 mA was passed through the sample and the voltage measured while the sample was cooled down from room temperature. The ac R-T was measured using a lock-in at a frequency of 47 Hz, and both ac and dc measurements gave equivalent results. The superconducting transition temperature, T_c, occurs when the resistance goes to zero. Transport R-T is a percolative measurement, in that it determines the T_c of the best connected path through the sample.

In weakly coupled bicrystals, a "foot" in the resistivity below the intragrain T_c was sometimes visible which depended on the amplitude of the measurement current. Gross et al. [61,12] have proposed that the foot is due to thermally activated phase slippage (TAPS) across a Josephson coupled GB. TAPS is similar to the thermal noise rounding seen in Josephson junction V-I curves, and is usually discussed in terms of the Ambegaokar-Halperin model [62]. TAPS has a dissipation magnitude which depends on the grain boundary resistance, R_n, the critical current, I_c (not the critical current density!), and the temperature.

Transport J_b is measured from the V-I curve at some arbitrarily defined criterion. In bulk wires, J_b is conventionally defined at a 1 μV/cm electric field criterion. In the bicrystal experiments, an electric field criterion is difficult to apply, since a highly non-uniform electric field, peaked at the GB, exists in the superconductor. It is the electric width of the boundary, and not the distance between the voltage taps, that is the relevant distance for calculating the electric field. However, the electric width of the boundary is unknown. In the bulk bicrystals, uncertainties in the size and position of the contacts, and an irregular sample geometry complicate accurate determination of the electric field. For these reasons, J_b of the bulk bicrystals is defined by a voltage criterion of 1 μV.

Voltage-current curves were measured by sweeping the current while measuring the voltage. Both increasing and decreasing, and positive and negative current sweeps were made. Strongly coupled bicrystals had large J_b, no low field dependence to J_b, and a rapidly increasing voltage with current above the critical current density. Weakly coupled bicrystals had smaller J_b, strong dependence of J_b on fields of less than 20 mT, and an approximately linear increase of voltage with current. Resistive bicrystals had no measurable J_b.

Results

In the following figures, data characteristic of strongly and weakly coupled bulk bicrystals are shown. In Figure 3.1(a), the R-T transition for a strongly coupled bulk [001] tilt 6° bicrystal is shown. $T_c(0) = 93$ K, and the normal state resistivity shows the linear behavior characteristic of transport along the a-b plane. The inset shows the transition region in greater detail. Typical intragrain $T_c(0)$ ranged from 90 to 95K, and the strongly coupled bulk bicrystals had intergrain T_c values that would also lie in this range. The flux grown bicrystals had room temperature intragrain resistivities on the order of 500 μΩ-cm, although the irregular bicrystal geometry and non-isotropic transport [57,58,59] made accurate calculations difficult. This uncertainty in the resistivity is the reason Figure 3.1 plots resistance instead of resistivity. Figure 3.1(b) shows the R-T curve for a weakly coupled 16° bicrystal. The curve looks much the same as Figure 3.1(a), as the normal state transport is dominated by contributions from the intragrain region. However, the “foot” characteristic of weak coupling can be seen in the inset, just below the intragrain T_c.

In Figure 3.2(a), V-I curves at 0, 1, and 10 mT of a 6° [001] tilt bulk bicrystal are shown. The magnetic field is applied parallel to the macroscopic GB plane (parallel to the c axes). The curves have different voltage offsets, so that they can be distinguished. This is a strongly coupled bicrystal, as can be seen from (i) the smooth and rapid increase in voltage above I_c and (ii) the low-field insensitive V-I curves.

In Figure 3.2(b), the V-I curves of a weakly coupled bicrystal are shown. This 17° [001] tilt bicrystal shows an almost linear increase in voltage with current above I_c, and the V-I curves are very sensitive to low magnetic fields. The approximately linear increase of voltage with current typical of weak coupling is also visible. This slope, dV/dI, is often referred to as the dynamic grain boundary resistance, R_n.

Low field dependence can also be seen in an I_c-H plot, shown in Figure 3.3. In this type of measurement, a constant current above I_c, is applied to the sample, and the voltage is monitored as the magnetic field is swept. In the weakly coupled bicrystals, the voltage at a given current is approximately inversely proportional to the critical current, so this type of plot indicates the dependence of I_c with applied field. Figure 3.3 shows a number of field sweeps overlaid on one another, showing that the data is repeatable. A large hysteresis is seen in the curve, indicating magnetic history dependence of the GB flux profile. Both the oscillations of I_c in field and the hysteretic behavior are characteristic of a Josephson junction.

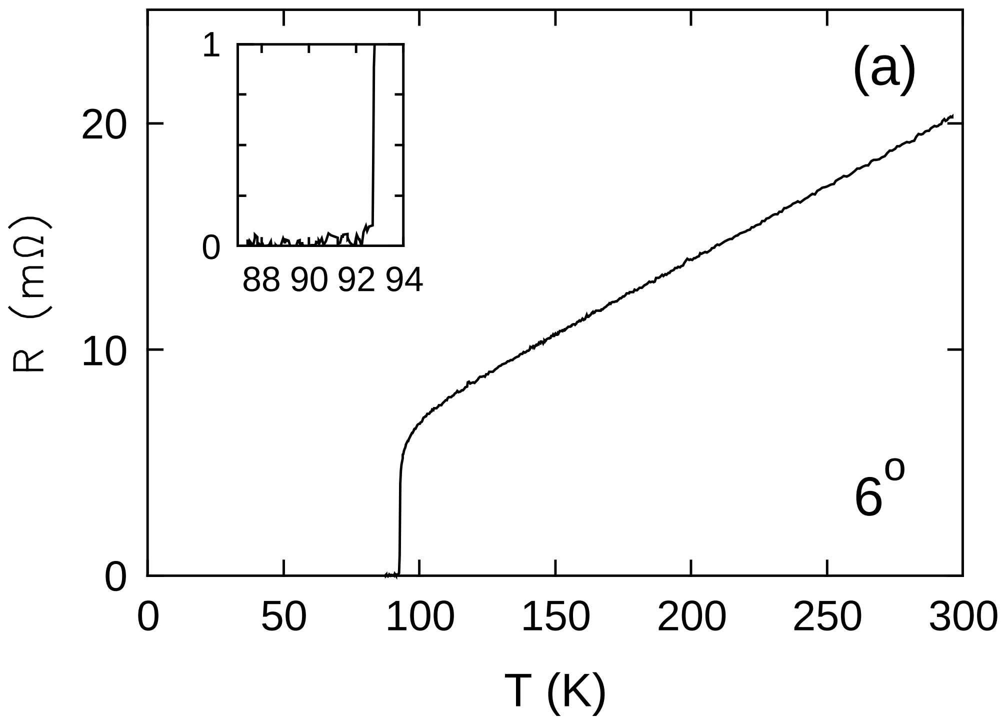

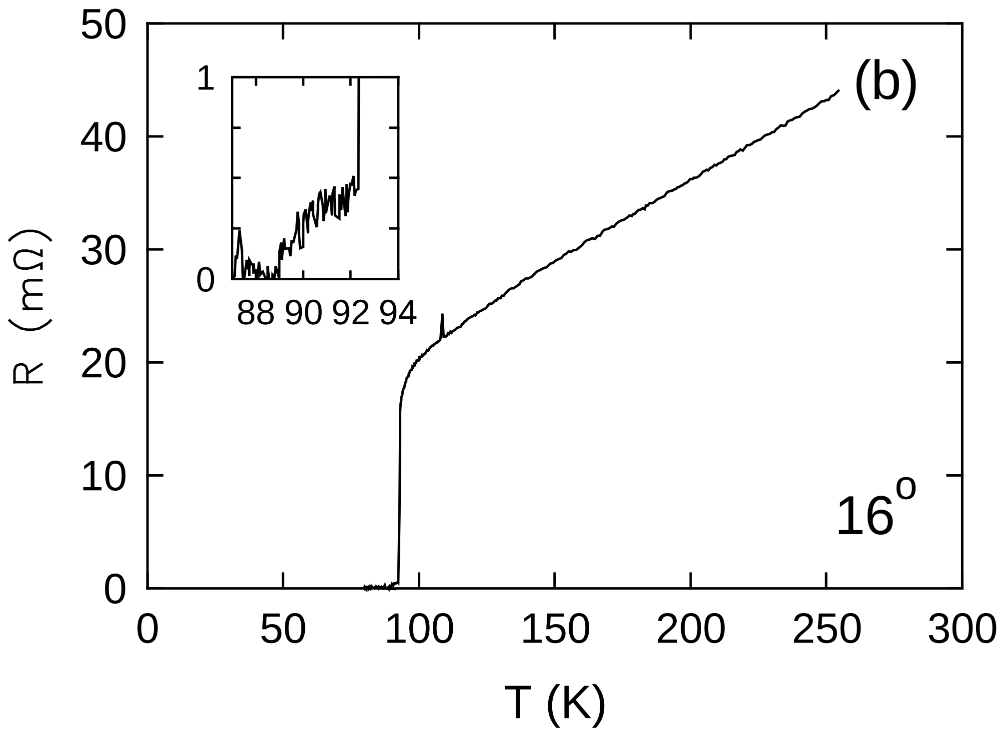

Figure 3.1 Resistance versus temperature for (a) a strongly coupled 6°[001] tilt, and (b) a weakly coupled 16°[001] tilt bulk scale bicrystal.

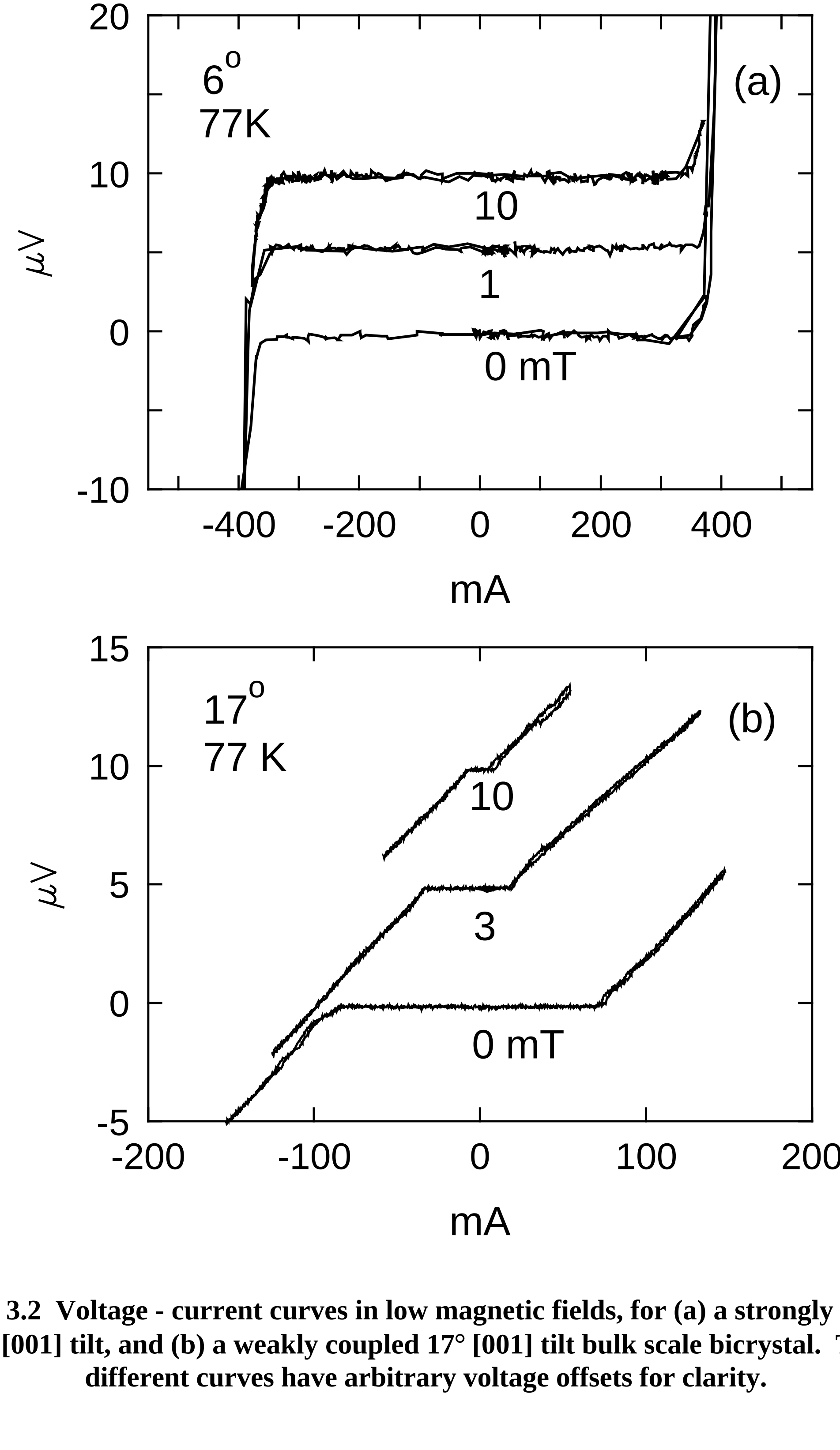

Figure 3.2 Voltage - current curves in low magnetic fields, for (a) a strongly coupled 6° [001] tilt, and (b) a weakly coupled 17° [001] tilt bulk scale bicrystal. The different curves have arbitrary voltage offsets for clarity.

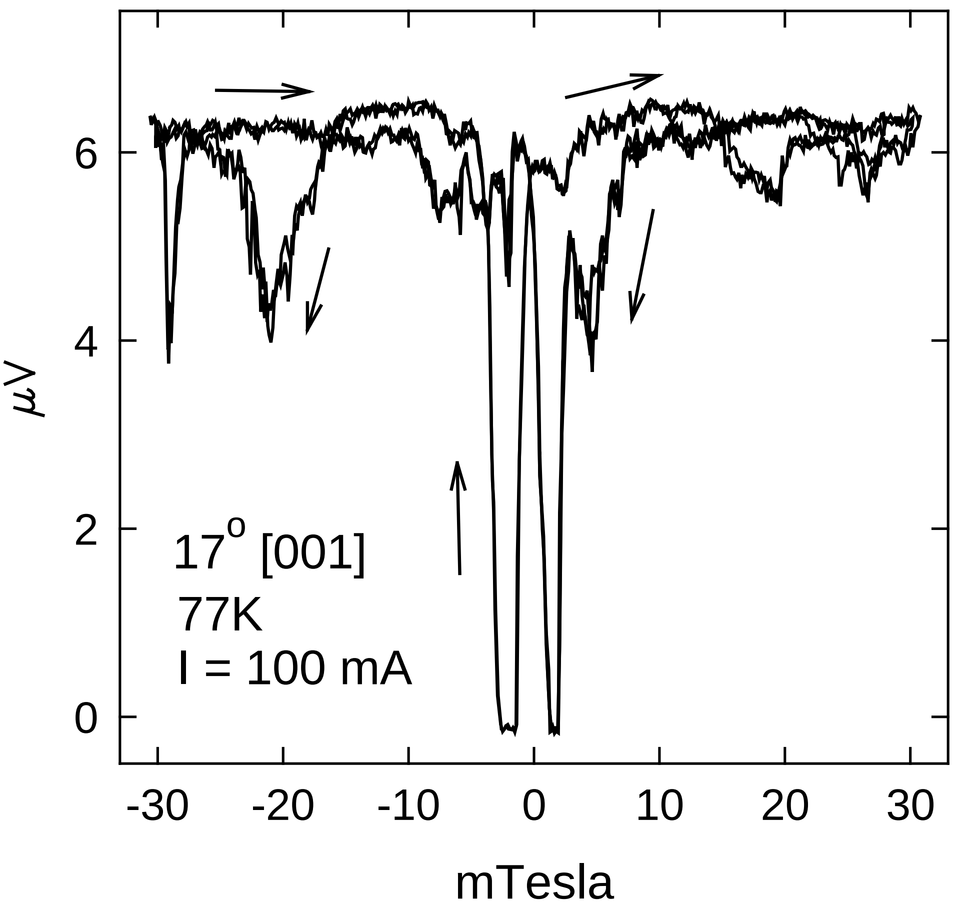

Figure 3.3 Voltage versus magnetic field at a fixed current, for a weakly coupled 16° bulk scale bicrystal.

The third type of boundary was resistive. The foot in the R-T curve extends to below 4.2 K, and no I_c was observed. Second phases, like CuO_2, were often observed along the boundary in such bicrystals.

Table 3.1 is a summary of the data on the low misorientation angle, bulk bicrystals, all taken at 77 K. The [001] misorientation angle is known to ± 2°, and the c axis misalignment is typically less than 2° or 3°. The grain boundary critical current density, J_b, is defined at a 1 μV criterion, and the range in J_b is due to variations in oxygen content between measurements. There are several points to be noted about Table 3.1.

All the bulk bicrystals with misorientation angles below 10° were strongly coupled, This is a larger transition angle than had been seen previously for the thin film bicrystals. Another observation is that all the bicrystals could be clearly characterized as being either strong, weak, or resistive. Little evidence of intermediate behavior was seen, even for misorientation angles near 10°, and this was also observed in the high field measurements discussed in the next chapter.

Table 3.1 Bulk Bicrystal Summary.

Sample	**[001] tilt angle**	**Character**	**T_c (GB)**	**J_b(77K)**
C3	3°	strong	93 K	3000 A/cm^2
0891C5	5°	strong	--	1544
0391C6	6°	strong	95	1100-3600
0592C4-CC6	7°	strong	93	680-1520
1291C9-Si	8°	strong	92.5	2300-4100
0593C10	10°	weak	92	600
0690P0C10-1	10°	strong	90.5	1700
0690C10-2	10°	weak	92	342
0891C14-1	14°	strong	92.5	850
0891C14-Ag	14°	resistive	< 4.2	0
1092C16	16°	weak	90.7	520
0193C16	16°	weak	90	113
081391C17	17°	weak	92	730
1092C18-Ca	18°	weak	93.5	375
0893C19	19°	weak	92	
0792C19	19°	resistive	<4.2	0

Figure 3.4 best summarizes the zero field bulk scale bicrystal data. Similar to what Dimos et al. plotted for their thin film bicrystals in Figure 1.1, in Figure 3.4 the bulk bicrystal J_c is plotted versus θ. The line on the graph is calculated from the dislocation

core model discussed in Chapter 1. It predicts a linear dependence of J_b/J_c on θ at low misorientation angles. The slope and intercept depend on the Burgers vector of the GBDs, **b**, and the effective GBD core diameter, $2r_m$. Since the low angle bulk boundaries that have been studied by HRTEM consist mainly of partial dislocations with **b** = 1/2[110], assuming an average |**b**| = 0.27 nm seems reasonable. The core diameter is unknown, so an estimate of $2r_m = 1$ nm was made. Since the intragranular J_c was seldom measured, an average intragrain $J_c = 3500$ A/cm^2 was chosen. Within the substantial scatter, the model is a reasonable fit to the data.

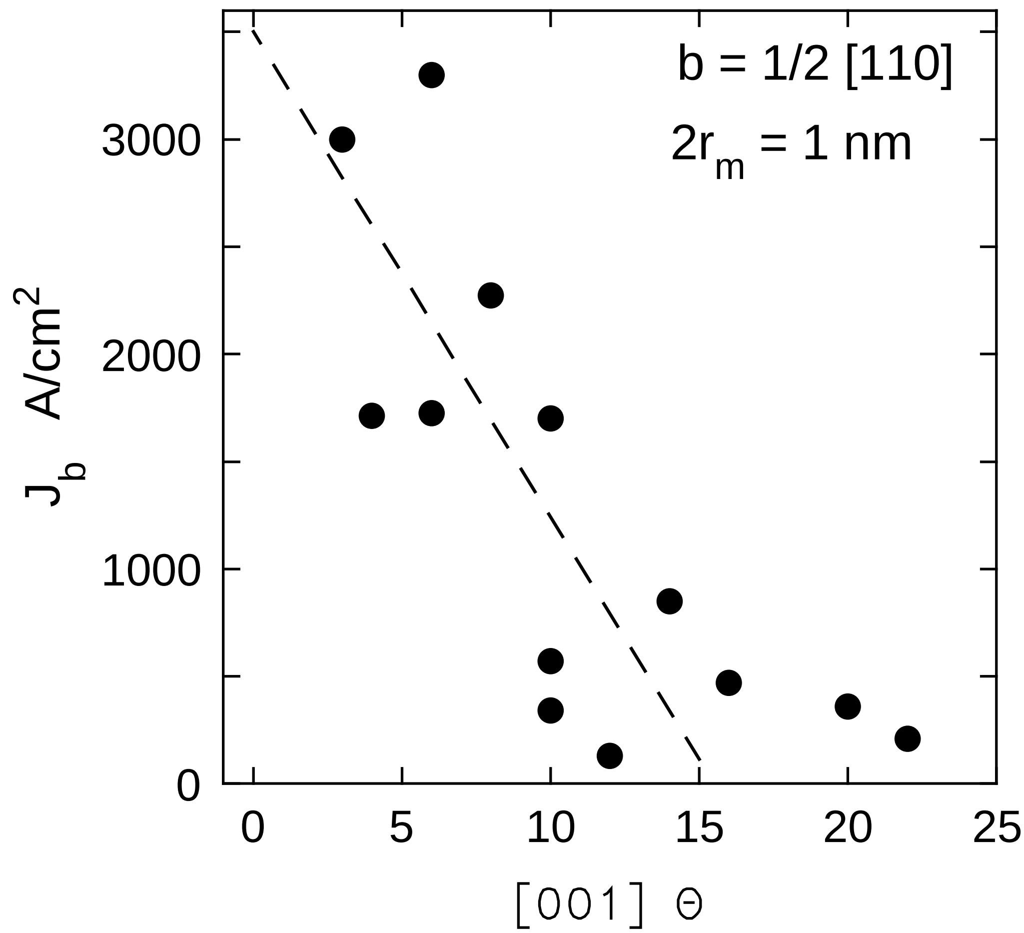

Figure 3.4 J_b versus θ for the bulk bicrystals at 77 K in zero field. The dashed line indicates the predicted behavior from the dislocation core model with |b| = 0.27 nm, $2r_m$ = 1 nm, and J_c = 3500 A/cm^2.

Thin Film Bicrystals

Experimental Details

The low field thin film measuring rig consisted of a Cu measuring block, heater, Si diode thermometer, and 18 Pogo™ pin terminated measurement leads. After alignment, the sample substrate was attached to the Cu block with Ag paint. During measurement, an overpressure of He gas was maintained to prevent cryopumping. A small magnet could produce fields of up to 4 mT.

Because the thin film bicrystals could be patterned into small links (5 - 100 μm wide), small currents fed into relatively large contact pads could be used to measure the V-I curve. Both factors reduced contact resistance and sample heating. On the other hand, a high accuracy, low noise current source, like the Keithley 224, was essential. Because this work was carried out in parallel with detailed low field characterization of high angle, weakly coupled thin film bicrystals, low field measurements on the film bicrystals were done in a screened room to reduce rf noise, and a mu metal shield was introduced to shield the earth's magnetic field.

The R-T curves were measured using an ac excitation current of 1-10 μA. The thin film bicrystal intergrain V-I curves were measured either by sweeping a dc current and measuring the voltage, or by an ac plus dc technique. By adding a constant ac signal to an increasing dc current and detecting the resulting ac voltage with a lock-in, one measures the dynamic resistance, dV/dI, as a function of applied dc current. The resulting dV/dI vs I curve was often a useful way to present the data, and it could also be integrated numerically to re-create the V-I curve. This hybrid technique allowed for good noise sensitivity, but was only suitable for samples with low critical currents.

The data was collected by a MacIntosh IIci running National Instruments' data acquisition package, *LabView*. The programs were written by Ron Redwing.

Intragrain Properties

One advantage of the films is that photolithographically defining the measurement links makes comparisons between different samples much more consistent. This section discusses the range of the thin film intragrain properties.

The patterned bicrystal films had a 500 μm x 10 μm intragrain link, and at room temperature the intragrain resistivities of this link ranged from 250-500 μΩ-cm. The intragrain current density, J_c, at 77 K was also measured, defined by an 1 μV criterion. The intragrain properties of the films were quite variable, as is seen explicitly in Figure 3.5. The properties summarized are the intragrain T_c, J_c, and RRR, where the RRR is the resistance at 300 K divided by that at 100 K. The lines are least square fits through the data. This data is also presented in Table 3.2, where the samples are listed in the chronological order in which they are grown, and the film thickness, t, is estimated from the growth time. In the literature, the best quality YBCO/STO films reported had an intragrain T_c of 90K, and a J_c of 5 MA/cm^2 at 77 K [63], so our bicrystal films are of quite high quality. In comparison to the flux grown bulk bicrystals, the T_c of the laser ablated films is somewhat depressed, but the J_c is 3 orders of magnitude higher.

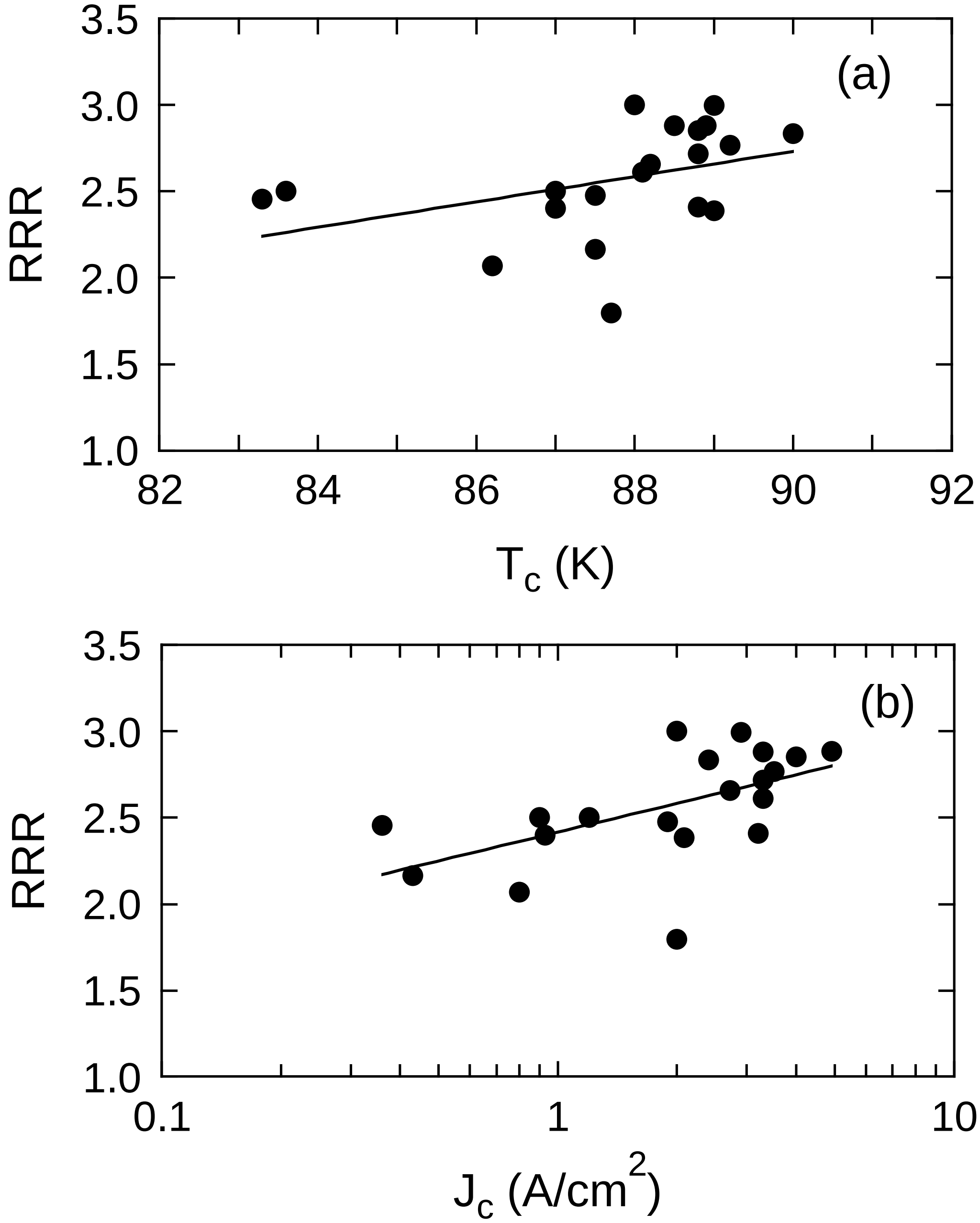

Figure 3.5 The intragrain properties of the YBCO/STO bicrystals: (a) T_c versus RRR, (b) J_c (77K) versus RRR. All data were taken in zero applied field.

Table 3.2 Summary of Intragrain Film Properties.

Sample	t (μm)	T_c (K)	J_c (MA/cm^2)	RRR
Y636sb20	0.14			
Y649sb5	0.14	89	2.9	2.996
Y664sb10	0.14	90	2.4	2.836
Y665sb15	0.14	87	0.93	2.4
Y666sb15	0.14	87.5	0.43	2.16
Y667sb36	0.14	80		
Y686sb36	0.22	87.8	1.89	2.48
Y691sb24	0.25	88.2	2.72	2.66
Y692sb7	0.25	87	1.2	2.50
Y695sb10	0.25	88.8	3.2	2.41
Y696sb3	0.25	86.2	0.8	2.07
Y698sb7	0.25	83.3	0.36	2.45
Y700sb15	0.25	89	2.08	2.39
Y708sb5	0.25	89.2	3.52	2.77
Y709sb24	0.13	83.6	0.9	2.50
Y711sb36	0.13	81		1.71
Y727sb7	0.10	88.8	4.0	2.85
Y728sb24	0.10			
Y738sb15	0.10	88.8	3.3	2.72
Y743sb5	0.10	88	2.0	3.00
Y745sb36	0.10		1.0	2.00
Y746sb36	0.10	88.1	3.3	2.61
Y747sb20	0.10	87.7	2	1.80
Y752sb7	0.10	88.9	3.3	2.88
Y777sb7	0.10	88.5	4.92	2.88

Intergrain Properties

This section, devoted to the results of intergrain thin film bicrystal measurements, gives examples of the different types of measurements, discusses how superconducting properties vary with sample geometry, and compares the low angle thin film bicrystal data to the dislocation core model.

In contrast to the bulk scale bicrystal measurements, the thin film bicrystals show a more gradual transition from strong to weak coupling. Evidence of some weak coupling can be seen even at 5°, and as θ increases, the sensitivity to low fields gradually increases. In Figure 3.6, the V-I curves for the inter and intragrain regions of a 5° bicrystal are displayed. For this particular film, Y695s-b(5°), a non-standard pattern was used, for which the intragrain link was 500 μm x 10 μm, and the intergrain link was 16 μm x 10 μm. While the intergrain voltage increases more rapidly than linearly with current, the intragrain link's V(I) dependence is even stronger, and a cross-over can be seen at about 100 μV. The inset is the intergrain I_c-H, calculated from individual V-I curves, showing the I_c dropping to 70 % of the zero field value in 4 mT. Since the intragrain link's I_c also decreases slightly in 4 mT, describing this 5° bicrystal as clearly weakly coupled could be misleading, particularly when this data is contrasted to that of a higher angle film.

Data from a more weakly coupled bicrystal, a 20 μm link across a 15° sample, are illustrated in Figure 3.7. In Figure 3.7(a), dV/dI is plotted versus I for applied magnetic fields of 0 and 0.2 mT. The insets show the corresponding V-I curves. The sharp peaks in dV/dI, just above I_c in the zero field curve, are characteristic of resistively shunted junction (RSJ) behavior. The RSJ model is used to describe the behavior of a Josephson junction, and a good fit to this model is often used as the criterion for a "good" weakly coupled junction. This can lead to some confusion in the definition of "goodness", as a small field dependence of I_c is more often used by those interested in bulk scale applications. R.D. Redwing [64] was involved in studying how well these YBCO/STO bicrystals behave with respect to this model. Bicrystals with θ < 10° could not be fit to the RSJ model. In addition to accentuating the structure of the V-I curve, an advantage of measuring dV/dI is that the grain boundary resistance, R_n, can be directly seen from the data.

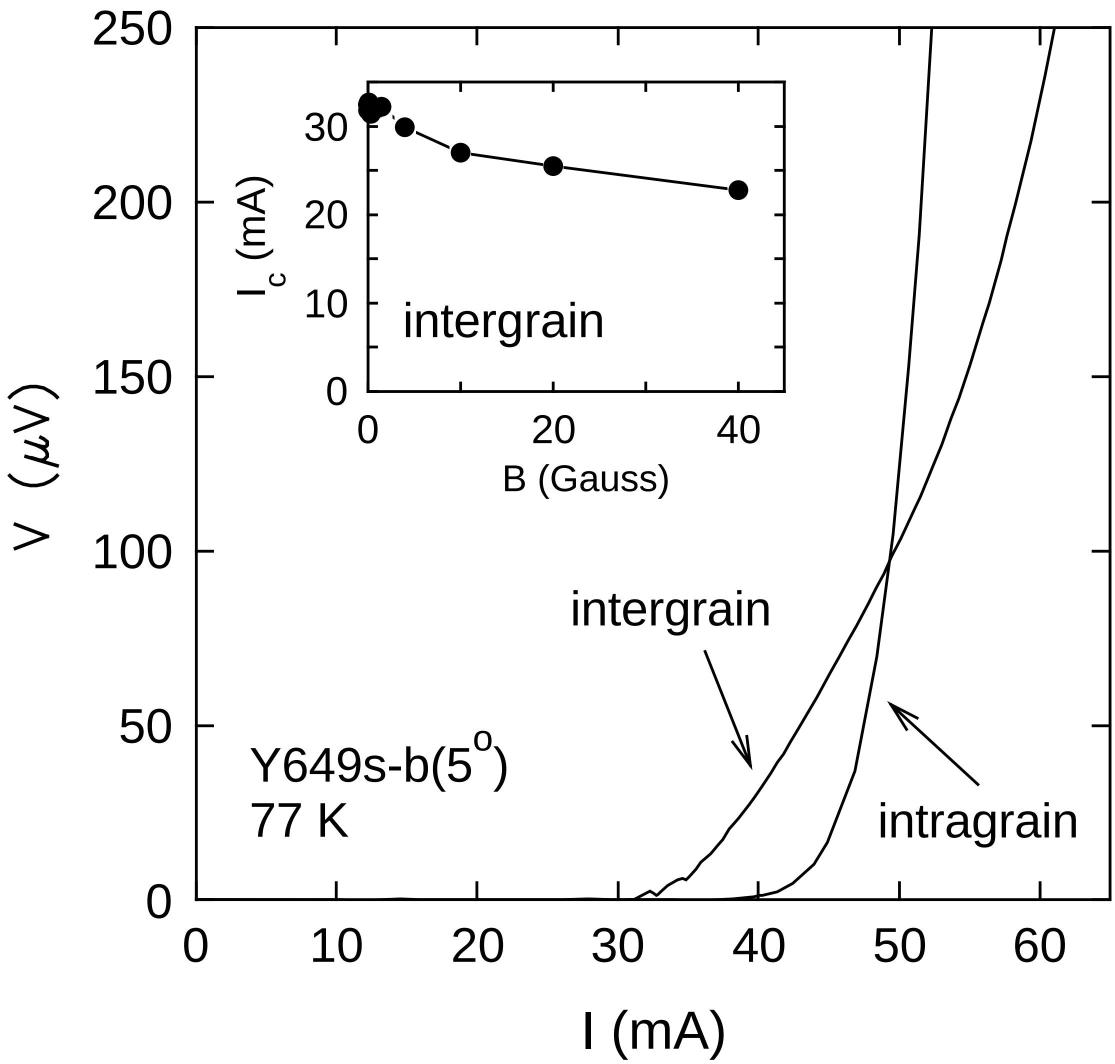

Figure 3.6 The V-I curves for inter- and intragrain regions of a 5°[001] tilt bicrystal film at 77 K and no applied field. Both intragrain and intergrain links were 10 μm wide. The inset shows I_c versus applied field for the intergrain link. I_c is defined by a 1 μV criterion.

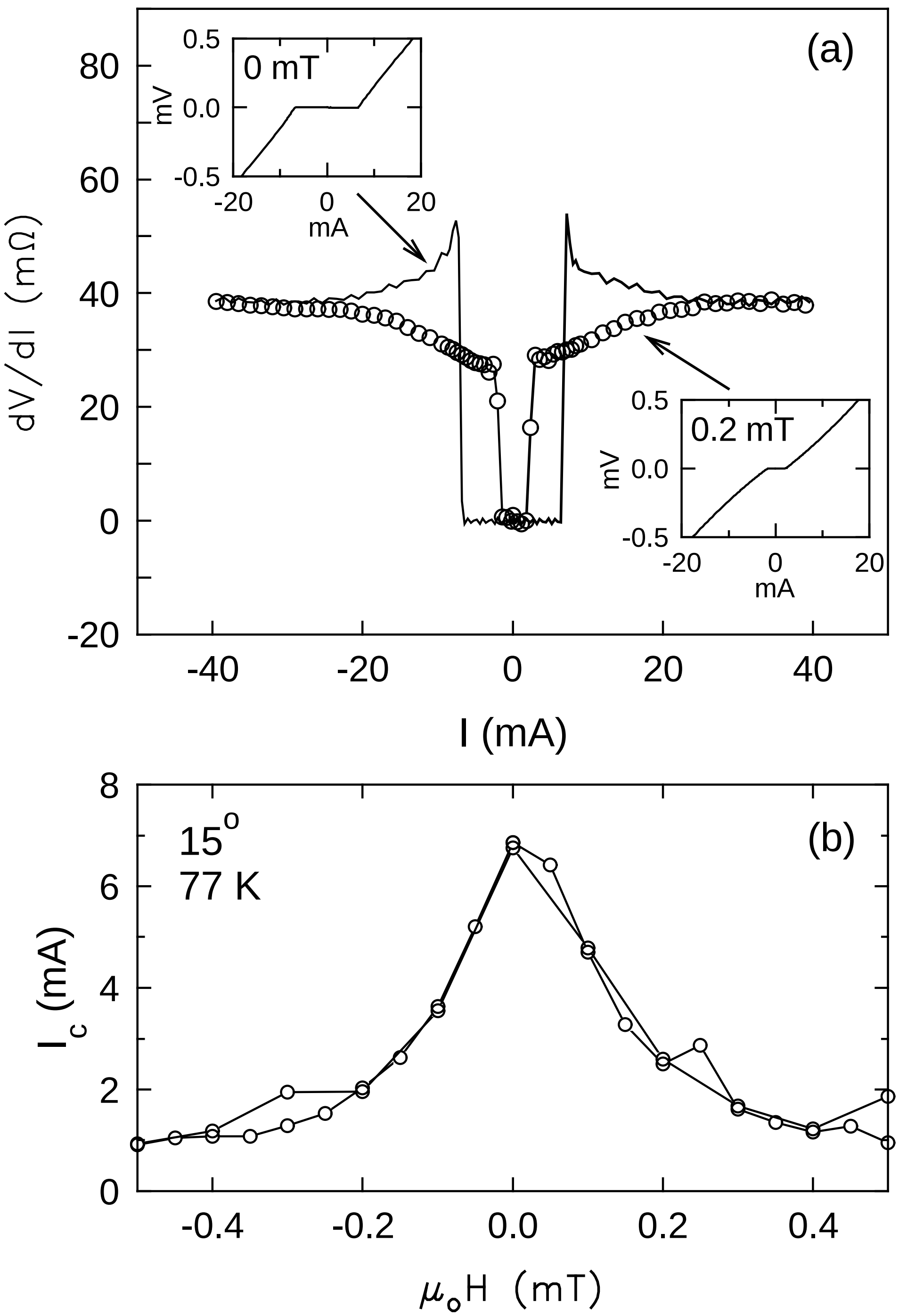

Figure 3.7 A weakly coupled 15°[001] tilt bicrystal. (a) dV/dI versus I, for fields of 0 and 0.2 mT. The insets show the respective V-I curves. (b) I_c -H shows the field dependence of I_c.

In Figure 3.7(b), the I_c vs. applied field B, for the same 15° link, is plotted. The sharp, almost triangular, central peak is characteristic of a long Josephson junction [65]. This plot should be compared to the inset in Figure 3.6. Studies of the main peak in $J_c(B)$, carried out by Ron Redwing, showed the peak width to be strongly dependent on misorientation angle, with the peak half width varying from 0.8 mT at 10° to less than 0.1 mT at 24°.

It is also possible to see how geometrical factors influence the transport characteristics. An example of how J_c and R_nA varies with the width of the link in a 10° boundary is given in Table 3.3. J_c and the normalized grain boundary resistance, R_nA, decreased as the link width increased, unless the link had been damaged. The decreased J_c occurs because of a more uneven current distribution across a wider link. The decrease in R_nA with increased width occurs because, in the RSJ model, a long junction approaches a final resistance value at much larger values of current than a short junction. Typically, one measures a final resistance value at five times I_c for a short RSJ junction, and this was not always possible in these low angle bicrystals.

Table 3.3 Width dependences of a 10° thin film grain boundary.

Link Width (μm)	J_b (A/cm^2)	R_nA (Ω-cm^2)
5	6.40×10^5	7.5×10^{-10}
10	3.74×10^5	
20	4.50×10^5	5.0×10^{-10}
50	3.20×10^5	4.7×10^{-10}
100	2.71×10^5	

Similar to Figure 3.4, the thin film bicrystal data was compared to the dislocation core model. In Figure 3.8, a plot of J_b /J_c versus θ is shown. Both intergrain J_b, and intragranular J_c at 77 K were measured for each bicrystal. Plotting J_b/J_c, instead of J_b, much reduced the scatter in the data due to film-to-film variations. Only 5 and 10 μm wide links are plotted, so the scatter is due to differences in film growth, and not to the width effects described above. As discussed in Chapter 1, microstructural studies show that the thin film GB consist of either dislocations with Burgers vector **b** = [100], or perhaps **b** = 1/2[100]. With these values of |**b**|, and assuming a GBD core diameter of 1 nm, the dislocation core model predicts the straight lines shown in the plot. The reduced scatter reveals that a linear decrease in J_b/J_c no longer fits the data very well. Rather, if one looks at the best (highest J_b/J_c) samples, there appears to be very little decline in J_b/J_c up to misorientation angles of 7°. At higher angles, J_b/J_c appears to decrease exponentially.

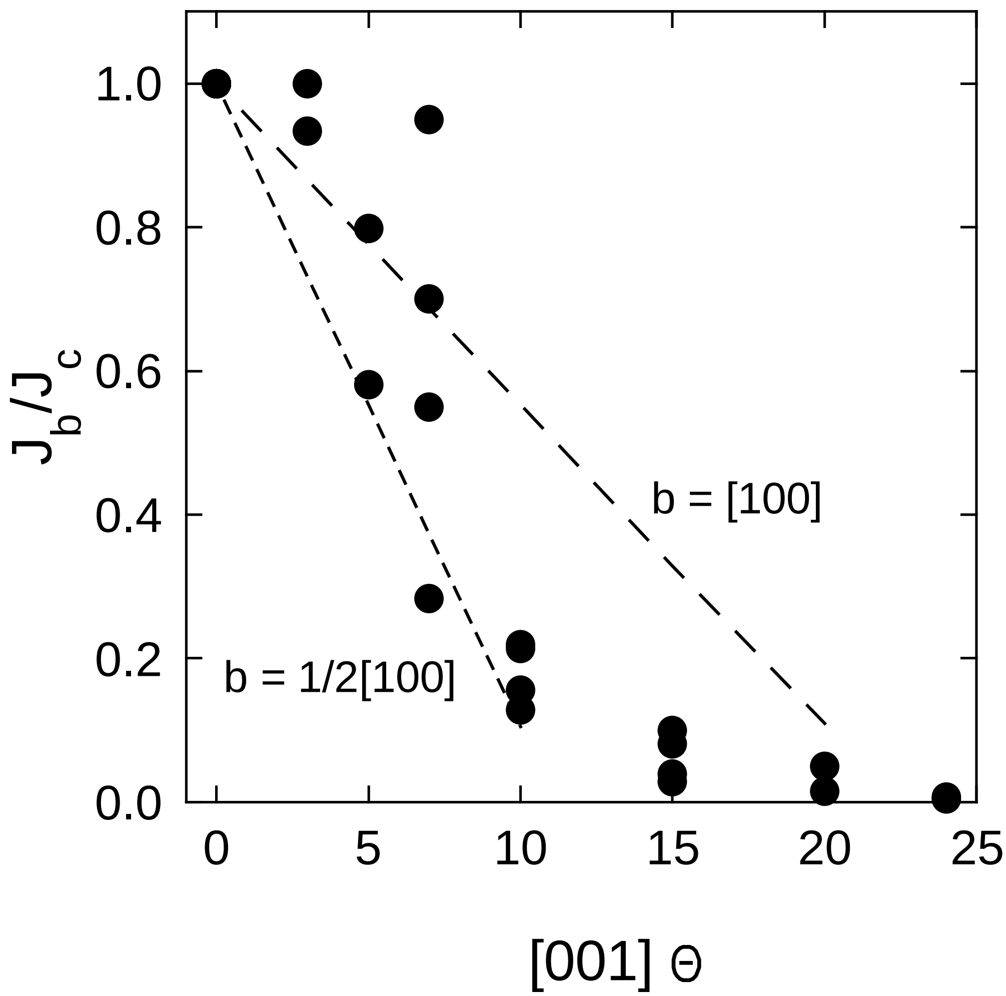

Figure 3.8 J_b/J_c versus [001] θ for the thin film YBCO/STO bicrystals, at 77 K and zero applied field. Only data from 5 and 10 μm wide links is shown. The dashed lines are fits to the dislocation core model, with b = 1/2[100] and b = [100], respectively.

Comparing Bulk and Thin Film Bicrystals

There are significant similarities and differences between the bulk scale and thin film bicrystals lying in the low misorientation angle region. In the bulk scale bicrystals, the transition between strong and weak coupling occurs at or above the somewhat large angle of 10°. Both strongly and weakly coupled 10° bulk scale bicrystals were seen. All the bulk bicrystals could be classified as either strongly, weakly or resistively coupled. In the thin film bicrystals, the transition between strong and weak coupling is less obvious, as evidence of some weak coupling behavior was seen at $\theta = 5°$, although true RSJ behavior was not observed at 77 K until θ was greater than 10°.

It is also possible to compare the bulk scale and thin film bicrystals over the entire misorientation range of $0° < \theta < 45°$ by compiling the results of data collected by X.Y. Cai, R.D. Redwing, and myself. Over the entire misorientation range there are some interesting differences between the bulk scale and thin film bicrystals, and these are discussed briefly below.

As discussed in Chapter 1, a number of other groups have studied higher angle YBCO [001] tilt thin film bicrystals as a function of θ [1,9,12]. A recent paper [66] on the microstructure and transport properties of bicrystal films of $Bi_2Sr_2CaCu_2O_x$ notes that an exponential slope of $J_b(\theta)/J_c \approx \exp(-0.2\ \theta)$ describes both YBCO and $Bi_2Sr_2CaCu_2O_x$ bicrystal thin films well. The authors' suggest that the similarities in the dependence of J_b with θ are due to a similar "wavy" morphology of the GB in both YBCO and $Bi_2Sr_2CaCu_2O_x$, which is a consequence of the island-plus-layer film growth seen in both types of films. Our data comparing the bulk and thin film bicrystals support this conclusion.

In Figure 3.9, J_b in zero field is plotted on a semi-logarithmic scale versus θ, for all our bulk and thin film bicrystals, all at 77K. While our film $J_b(\theta)$ is quite similar to that seen in the literature, the bulk bicrystal $J_b(\theta)$ has a much less pronounced θ dependence. After a decrease in J_b as the transition from strong to weak coupling occurs, in the higher angle region between 15° and 45° the bulk J_b remains virtually constant. When one recalls that unlike the thin films, bulk scale grain boundaries have a much less meandering boundary plane, even in the high angle, weakly coupled region, the hypothesis that the meander structure of the thin film boundary plane is responsible for the exponential decrease in the higher angle $J_b(\theta)$ appears quite reasonable.

Further interpretation of this data is made difficult by the almost 4 orders of magnitude between the bulk and thin film intragrain J_c, and the different geometries of the two kinds of samples. Some of the bulk samples were re-measured after being ground and polished (the "thinned" bulk), and in all cases J_b increased. This geometrical artifact appears analogous to the width effects seen in Table 3.3 . One comment regarding the difference in the thin film and bulk J_b, is that Dimos et al.'s original bicrystal experiments were carried out (at 4.2 K) on films with rather low J_c, and they also observed an exponential decline in J_b [12]. It thus appears likely that the exponential decrease seen in film bicrystal $J_b(\theta)$ is specific to the film morphology, and not an intrinsic feature of all YBCO grain boundaries.

The GB normalized resistance, or R_nA, is another quantity that was measured as a function of θ. The normalized resistance is found by measuring the slope of the V-I curve above I_c and then multiplying that resistance by the GB cross-sectional area. R_nA is not well defined in strongly coupled boundaries with V-I curves with flux-flow curvature, so R_nA is plotted only for weakly coupled bicrystals. R_nA is useful in that, unlike J_c, it has little magnetic field or temperature dependence.

Figure 3.10, R_nA for bulk and thin film bicrystals are plotted versus θ [67]. Again, the thin film and bulk scale data have very different θ dependence. Reflecting the

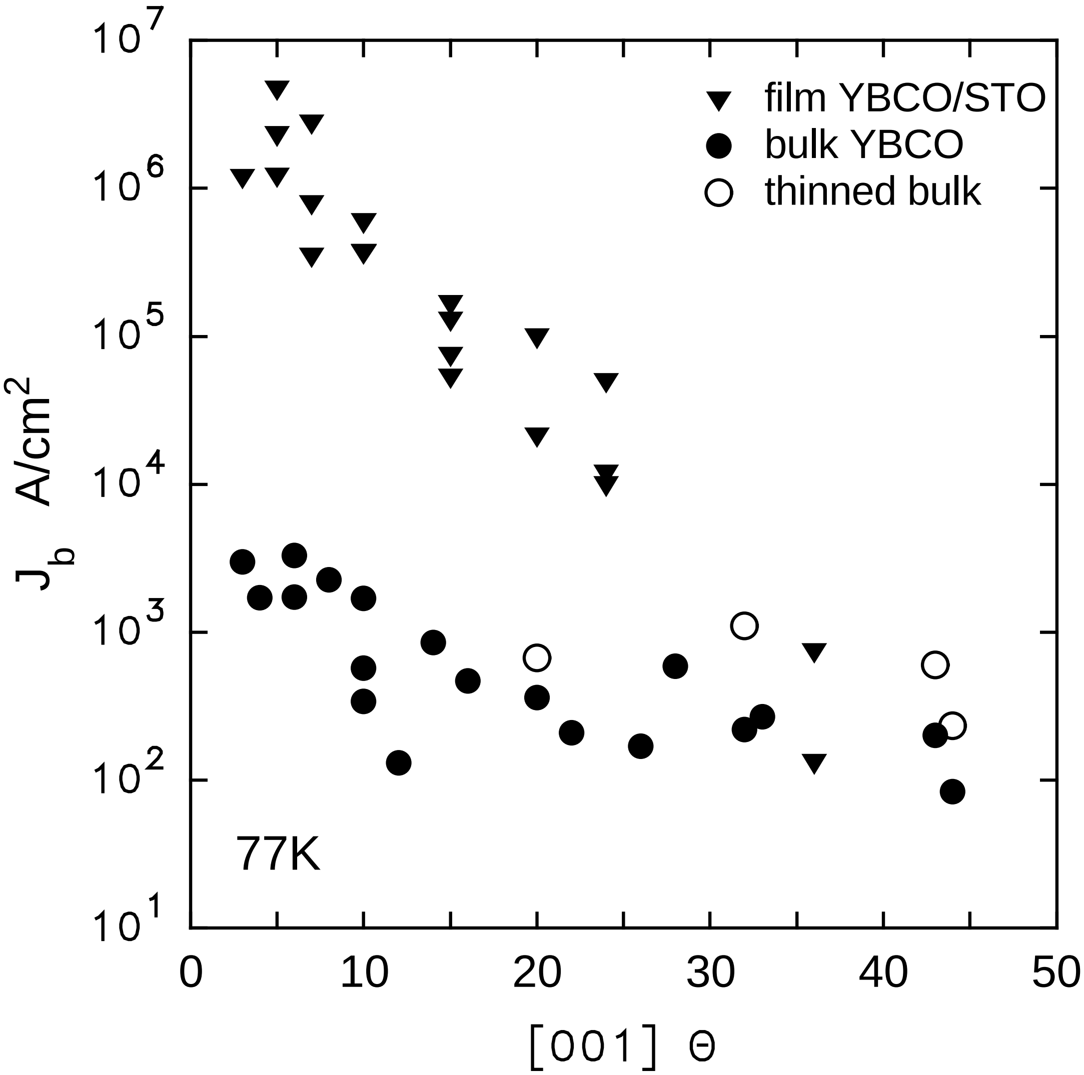

Figure 3.9 J_b versus θ for bulk scale and thin film bicrystals with misorientation angles lying between 0° and 45°. All data were taken at 77 K and zero applied field.

$J_b(\theta)$ data, the thin film bicrystals have values of R_nA which show a distinct, approximately linear dependence on θ. The bulk scale bicrystals' R_nA show little θ-dependence, except for a slight increase near 45°. The somewhat higher R_nA values in the bulk scale bicrystals is probably an artifact of the large GB cross sectional area.

Microstructural analysis by Na Zhang showed that near 45° bulk scale bicrystals tended to have a greater concentration of second phases at the GB than lower angle bicrystals, perhaps accounting for the upturn in R_nA at these high misorientation angles.

One conclusion that can be drawn from Figure 3.9 and Figure 3.10 is that the behavior of the thin film bicrystals does not reflect what occurs in the bulk scale bicrystals. The differences between the film and bulk scale grain boundary microstructures seen by HRTEM clearly affect the GB transport properties like J_b and R_nA. These discrepancies appear to be only partly due to differences in the thin film and bulk intragrain properties, because it is difficult to see how the different θ-dependences of R_nA and J_b could be simply a result of the variation in thin film and bulk intragrain properties.

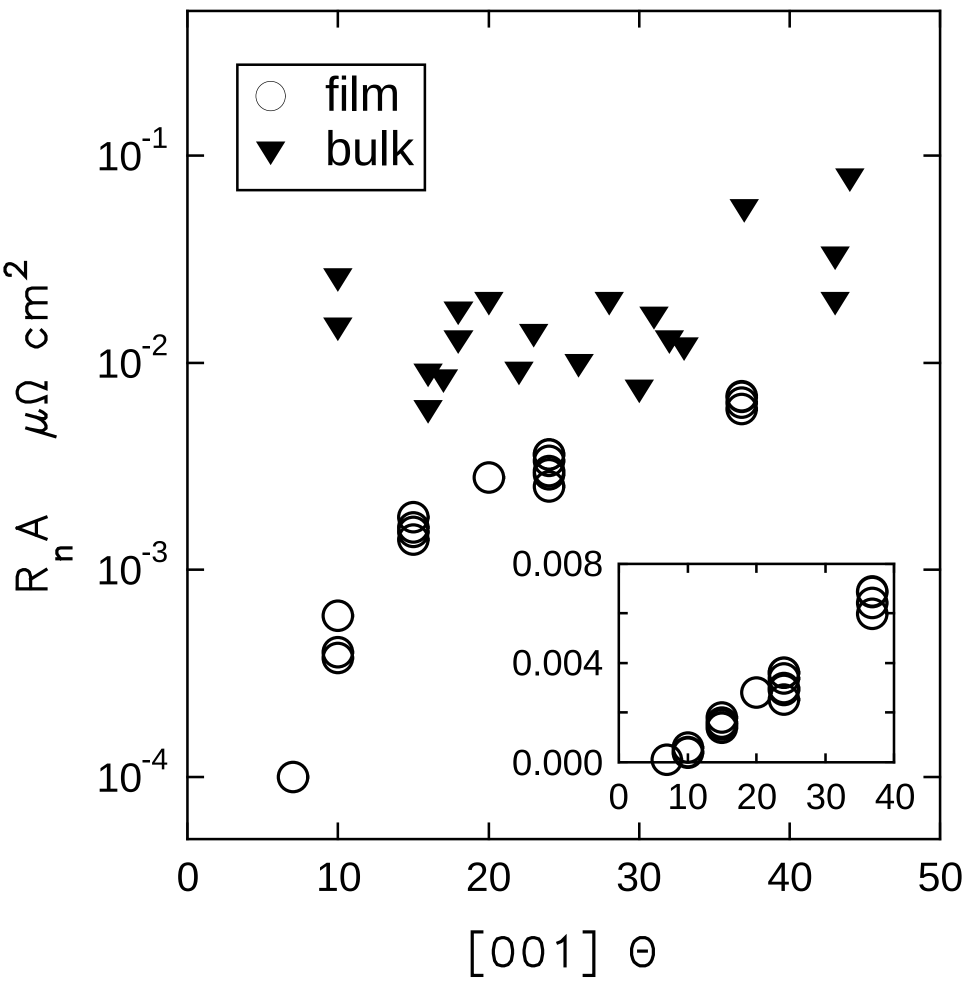

Figure 3.10 The normalized grain boundary resistance, R_nA, versus θ, for 7° < θ < 45°, at 77 K. The inset shows R_nA vs. θ of the thin films plotted on a linear scale.

Chapter 4 : High Field Bulk Bicrystal Measurements

Introduction

The voltage-current curves of a number of bulk scale bicrystals were measured in high magnetic fields. The experiments that I made focused on the high field properties of those bicrystals that low field measurements had established to be strongly coupled. This complemented the high field studies of weakly coupled bulk bicrystals that were led by Dr. Cai [68]. In the following chapter, $J_b(H)$ data for various strongly coupled bulk bicrystals are plotted, and compared to that of a typical weakly coupled bulk bicrystal. The effects of aging and oxygenation are investigated, and the ways in which these bulk scale data compare to the thin film measurements is discussed.

Experimental Details

The bulk bicrystals were measured in one of two superconducting magnets; an 8 Tesla, wide bore "Canadian" magnet, or a 14 Tesla magnet from Oxford Instruments. In the Canadian magnet, the bore was filled with a liquid nitrogen or helium bath, and the measurement rig had a vacuum can around the sample, filled with He gas to provide a good thermal contact with the bath. The Oxford magnet was equipped with a variable temperature insert (VTI) which allowed any temperature between 4.2 K and 300 K to be selected. The VTI works by controlling the flow of cold He gas from the magnet bath, and then heating the gas to the appropriate temperature.

Results

In Figure 4.1, J_b versus H at 77K is plotted for a strongly coupled 7° [001] tilt bulk bicrystal [69]. With the magnetic field applied parallel to the bicrystal c-axes, J_b decreases slowly and approximately linearly with field. The inset shows the V-I curves in the vicinity of the irreversibility field, H*. Because this data was relatively noisy (~ 0.3 μV noise levels), determining H* by the change of curvature in the extended V-I curves was not feasible. However, at or around 8 Tesla, there is no measurable non-dissipative supercurrent, and this value of H* = 8 T is about the same as for a flux grown YBCO single crystal [70]. This value of H* also corresponds to where the linear extrapolation of the $J_b(H)$ curve goes to zero. The V-I curves are rounded, and show the flux-flow, power-law shape typical of strongly coupled single crystals.

In Figure 4.2, J_b versus H at 77K is plotted for a number of bulk bicrystals that were classified as strongly coupled, based upon their low field V-I characteristics. All the samples show the same linear decrease in J_b with field, with no apparent trends with misorientation angle. The $J_b(H)$ curves are qualitatively similar, as shown in the normalized inset plot (except for the one bicrystal grown in a Si-doped melt which may have a slightly higher H*). The reasons for the variations in the magnitude of J_b are unclear. We attribute them to (i) errors estimating the GB cross-sectional area, and (ii) variations in the oxygen content. The impact of oxygen content on the transport properties may be inferred from Figure 4.3, where repeated high field measurements of a single strongly coupled bicrystal sample are plotted.

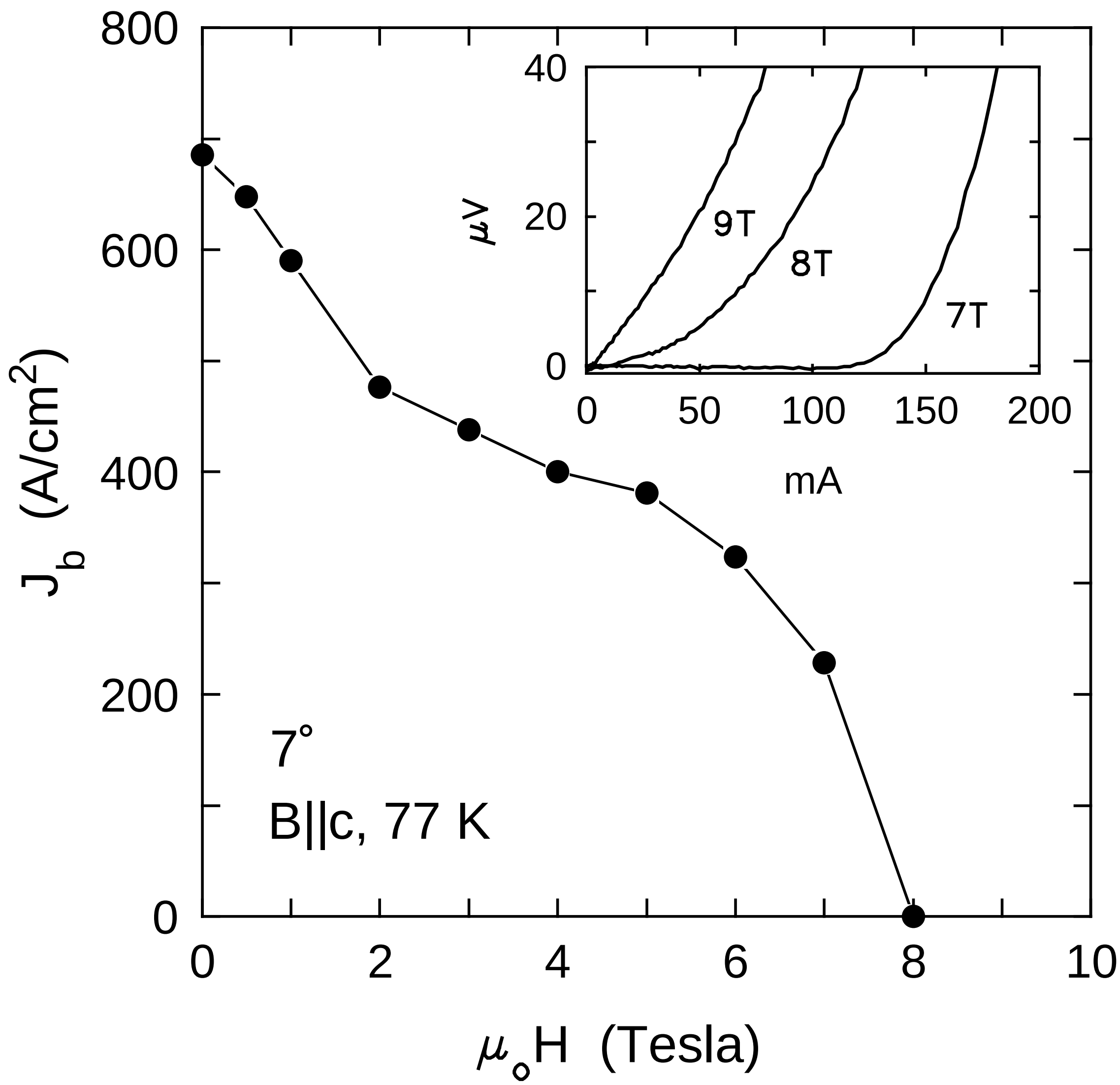

Figure 4.1 J_b versus applied field for a 7° [001] tilt bulk scale bicrystal at 77 K. The inset is of the V-I curves at 7, 8, and 9 T. The curves show a distinct change between 7 and 9 T, indicating that H* lies somewhere between those two fields.

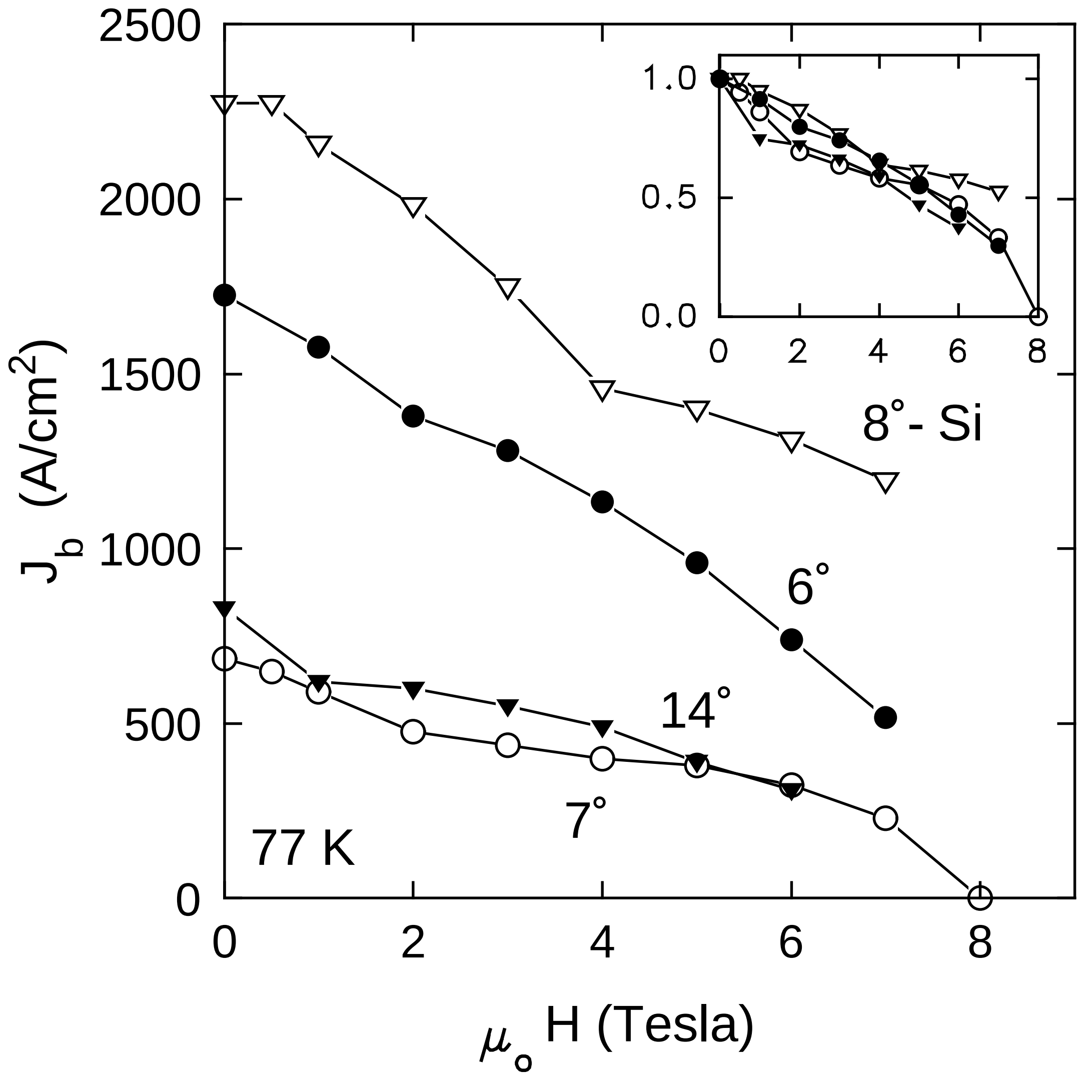

Figure 4.2 J_b versus applied field for several strongly coupled bulk scale bicrystals with misorientation angles of 7°, 14°, 6°, and 8°. The magnetic field is applied parallel to the bicrystals' c axes. The inset compares these normalized J_b - H curves.

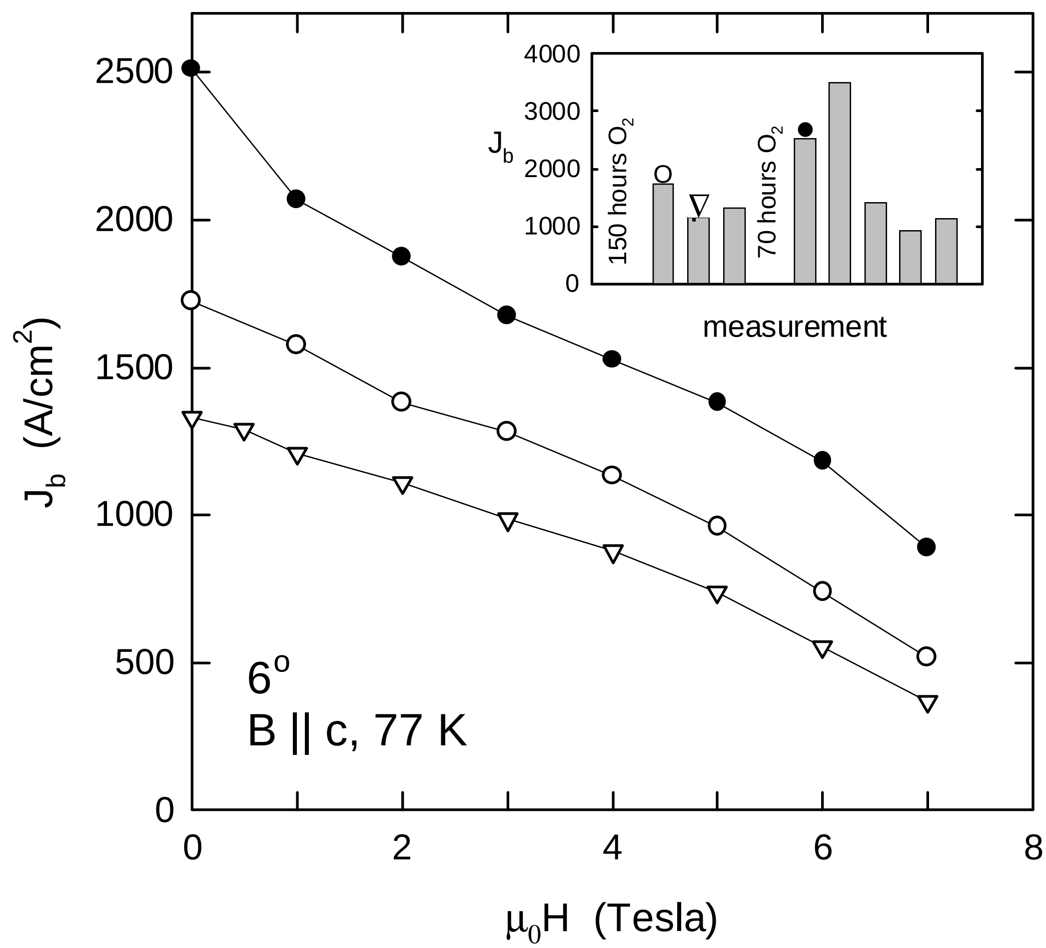

Figure 4.3 J_b versus applied field for a 6° [001] tilt bulk scale bicrystal measured on three different occasions. The inset shows how the zero field J_b can vary from measurement to measurement. The measurements occurred over a year.

For the 6° bicrystal data shown in Figure 4.3, there are substantial variations in the critical current density with time. In the inset, the zero field J_b values of the sample are displayed chronologically, showing how J_b varies from run to run. The measurements that were also done in high magnetic fields are indicated by the symbols. After an initial oxygenation at 420°C for 150 hours, J_b(0 T) = 1700 A/cm^2, which after sitting at room temperature for some time, dropped to J_b(0 T) = 1350 A/cm^2. Then, after an additional 70 hours of oxygenation at 420°C, the GB critical current density rose to J_b(0 T) = 2500 A/cm^2, indicating that the changes in J_b are probably due to variations in oxygen content. In the main plot, it can be seen that the variations in the magnitude of J_b had little effect on the shape of the J_b(H) curve for the strongly coupled bulk bicrystals.

In Figure 4.4, the same sample as in Figure 4.3 is measured at several temperatures: 74 K, 77 K, 85 K, and 90 K. By assuming here that the irreversibility field is the point where J_b(H) extrapolates linearly to zero, this plot illustrates the approximate variation of the irreversibility field with temperature. At 90 K, $H^* \approx 1.5$ T; at 85 K, $H^* \approx 4$ T; while at 77 K, $H^* \approx 8$ T. The similarity of the J_b(H) curves at the different temperatures should also be noted.

In Figure 4.5, the J_b(H) characteristics of a 16°, weakly coupled, bulk bicrystal is plotted. The applied field is again parallel to the c-axes. These data were taken at 40 K and 77 K. Even at this relatively low misorientation angle, the intergrain J_b decreases very quickly with field. At 77 K, there is no longer a measurable J_b at 0.3 T. At 40 K, J_b decreases almost an order of magnitude between 0 and 0.5 Tesla, and then remains roughly constant up to 5 Tesla. This behavior is in sharp contrast to that of the strongly coupled bulk bicrystals in Figure 4.1 and Figure 4.4.

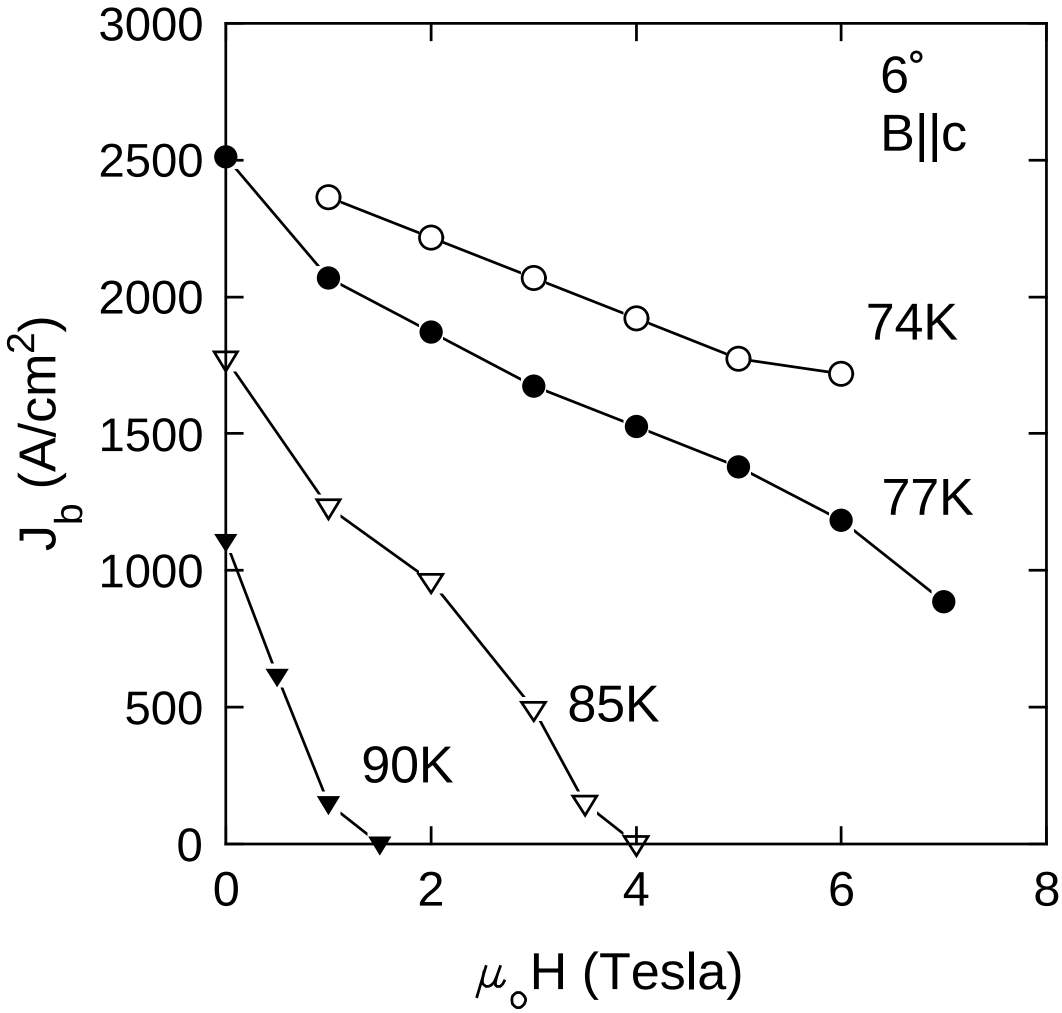

Figure 4.4 J_b versus applied field of a 6°[001] tilt strongly coupled bulk bicrystal at 90 K, 85 K, 77 K, and 74 K.

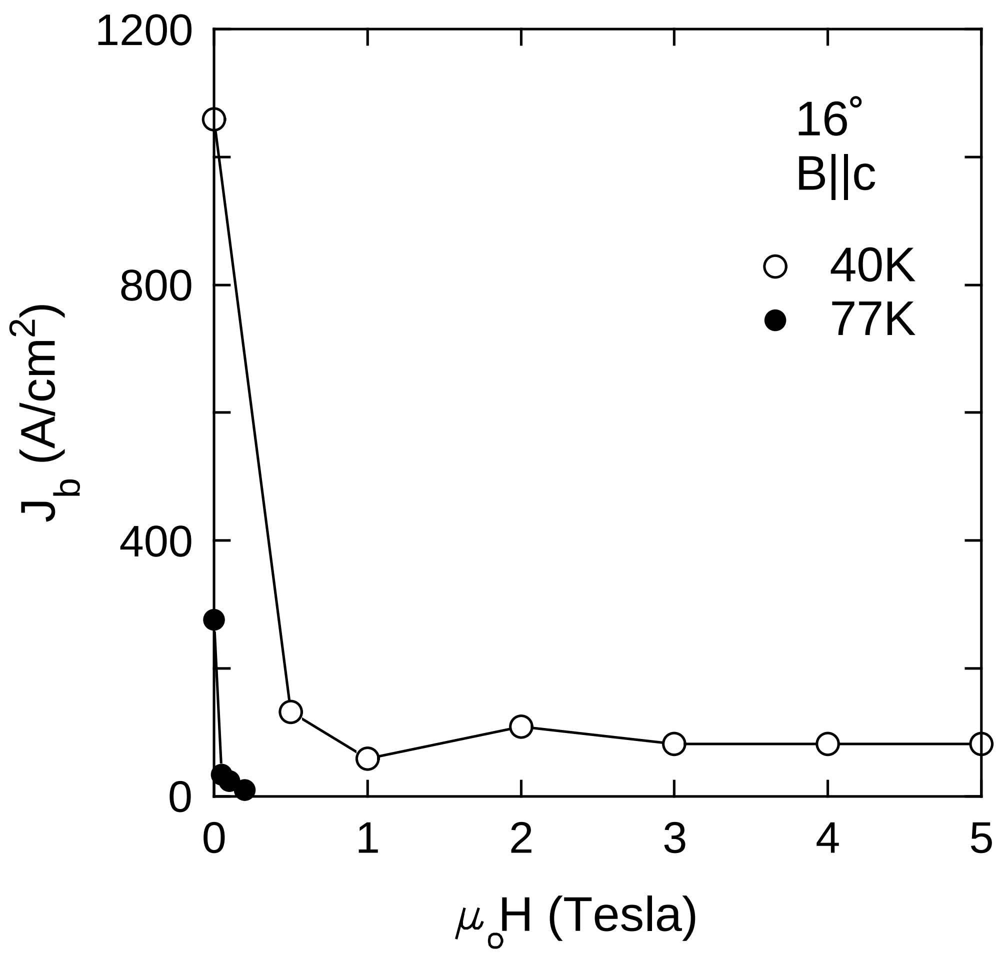

Figure 4.5 J_b versus applied field for a weakly coupled 16° [001] tilt bulk scale bicrystal, at 77 K and 40 K.

Discussion

The field dependence of the grain boundary critical current density, $J_b(H)$, has been measured as a function of misorientation angle, temperature, and aging. The strongly coupled bulk scale bicrystals have an approximately linear dependence of J_c with magnetic field, and an apparent irreversibility field, H*(77K), of about 8 Tesla. This should be compared to the exponential fall-off of $J_b(H)$ and the somewhat lower H* values that will be seen in the thin film bicrystal data in Chapter 5. Aging effects, most probably due to variations in oxygen content in the bulk bicrystal, can have a considerable impact on the magnitude of J_b, causing it to vary by as much as a factor of 3. Nevertheless, aging had little effect on the field dependence of J_b, at least for the strongly coupled bulk bicrystals, nor did it appear to affect H*(77 K).

These high field bulk bicrystal experiments show that there is an abrupt change as one undergoes the transition between strongly and weakly coupled bulk bicrystals. Between 4° and 14°, the J_c-B curves are approximately linear, with no evidence of any misorientation angle dependence. However, even a rather low misorientation angle 16° weakly coupled bulk scale bicrystal has completely different in-field behavior. For this weakly coupled bicrystal, J_b dropped off very rapidly in low magnetic fields before assuming an almost constant value in higher fields. This type of in-field behavior in bulk scale bicrystals with misorientation angles between 15° and 27° has also been seen by Dr. X.Y. Cai. This abrupt change in behavior between strong and weak coupling with increasing θ contrasts with the more continuous change in $J_b(H)$ that will be seen in the thin film bicrystals in Chapter 5.

Chapter 5 : High Field Film Bicrystal Measurements

Introduction

Like the bulk scale bicrystals, the V-I curves of the $YBa_2Cu_3O_{7-x}$/$SrTiO_3$ thin film bicrystals were measured in large magnetic fields. In contrast to the bulk scale bicrystal measurements, where a sharp distinction between strongly and weakly coupled behavior was easily identified, in the thin film bicrystals the strong-to-weak coupling transition is more gradual.

Unlike flux-grown bulk $YBa_2Cu_3O_{7-x}$, in the films even the intragrain links have J_c values that decreased in moderate fields. In the bulk, the intragrain J_c decreases approximately linearly in Tesla fields, while in the films, the decrease in the intragrain J_c with field is exponential. Variations in the intragrain H*(77 K) from film to film were much larger than the intragrain bulk scale bicrystal properties. These differences in properties lead to differences in how the bulk scale and thin film bicrystal data are measured and analyzed.

In this chapter, the measurement of the bicrystal film V-I curves with nanovolt sensitivity is discussed. Most of the measurements were carried out at 77 K, although some other temperatures were also studied. Intergrain and intragrain $J_c(H)$ curves for bicrystal films of varying misorientation angles are presented. Pinning force curves are derived from the $J_c(H)$ curves, fit to a shear-limited pinning model, and the observed behavior is explained in terms of an electric-field argument. Extended V-I curves are plotted on a double logarithmic scale to illustrate the evolution of the curve shape as the field and misorientation angle are increased. The inter- and intragrain irreversibility field, H*, are extracted from the extended V-I curves, and compared to one another [71]. Extended V-I curves at fixed field and varying temperature are also presented. These results are then related to a strong and weak coupled channel model of the GB coupling.

Experimental Details

The thin film bicrystals were measured in a gas cooled environment in a 14 Tesla Oxford Instruments superconducting magnet with the applied field perpendicular to the film surface. Some of the higher angle bicrystals were also measured in liquid nitrogen in a high stability 1 Tesla Cu magnet. The Cu magnet has magnetic field stability of $\pm$ 0.4 Gauss.

The thin film measurement rig, like the bulk bicrystal rigs, has a Cu mounting block, a manganin wire heater, and a carbon glass thermometer. The eighteen measurement leads terminate in spring loaded contact pins that are mounted in phenolic. After the bicrystal sample is aligned, the phenolic piece is screwed down to get good contact between the pins and the bicrystal contact pads. The measurement leads are all single strand Cu, and are thermally connected to the Cu mounting block between the room and the sample to reduce heat flow down the leads to the sample. In addition, the current and voltage leads are thermally isolated from each other with generous amounts of Teflon tape.

Achieving low dc noise levels was an important goal when designing the rig. A Keithley 224 high stability 100 mA current supply and a high sensitivity Keithley 1801 preamplifier and 2001 voltmeter combination were used to run these experiments. The data were collected using a GPIB IEEE interface with a PC computer running National Instruments' data acquisition package, *LabWindows*.

As discussed in the Keithley's *Low Level Measurements* [72], the main sources of dc voltage noise are thermoelectric voltages (thermal emfs), inductive noise from changing magnetic fields in the circuit, and ground loops. Ground loops are avoided by connecting all the instrument grounds to the same place. Inductive noise is minimized by twisting the measurement leads together to reduce the circuit area, and by keeping the leads immobile during measurement. Thermal emfs are usually the largest source of dc noise, and occur when different parts of the circuit are at different temperatures, or when dissimilar conductors are connected together. Thus, minimizing the number of solder joints and allowing the entire measurement circuit to come to thermal equilibrium decreases thermoelectric voltages.

Since easily switching between sample links was desirable, it was not possible to eliminate all the solder joints. For the thin film rig, in a straight dc measurement, a noise floor of about 50 nV was achieved. However, by using the quasi-dc measurement suggested in [72], noise levels of 2 to 5 nV were possible. Measuring a V-I curve using a quasi-dc technique means that for each current value, one applies a positive I^+, measures

V^+, applies a negative I^-, and measures V^-. Unlike the voltage across the superconductor, any thermoelectric voltage will not change sign when the current is reversed, so the real signal voltage is $V = (V^+ - V^-)/2$. The quasi-dc measurement also minimizes baseline drift, since each pair of voltages is measured within 0.3 to 0.6 seconds of the other. More rapid data acquisition increased the noise level since the preamplifier - voltmeter combination needed time to settle.

Results

J_c versus H

The thin film bicrystals with misorientation angles of 3°, 5°, 7°, 10°, and 15° were measured at 77 K with H||c in large magnetic fields of up to 12 T. Both the inter and intragrain critical current densities were measured for each film, allowing one to see how film growth and aging affected both the grain and grain boundary properties. Because each film had a number of intergrain links, all with different widths, it was also possible to see how geometry affected the $J_b(H)$ characteristic, as well as compare the intergrain and intragrain data in a quantitative way.

In Figure 5.1(a), the intergrain and intragrain critical current densities at 77 K are plotted versus magnetic field for the 3° bicrystal film, Y696s-b(3°). The nominal electric field criterion selected to define J_c was 1 μV/cm. This corresponds to a voltage criterion of 0.05 μV across the intragrain link, and 0.01 μV across the intergrain links. An approximately exponential decrease in the intragrain $J_c(H)$ is seen. For $\theta = 3°$, the GB has no apparent effect on the high field transport properties. This is consistent with the low field transport data (Chapter 3), as well as magneto-optic studies of a similarly grown 3° film bicrystal (Appendix A, [73]).

In Figures 5.1(b),(c), and (d), intergrain and intragrain J_c values are plotted for 5°, 10°, and 15° bicrystal films. Even in the 5° bicrystal, the GB has a clear effect on the $J_c(H)$ curves. The intergrain $J_c(H)$ initially decreases more rapidly than the intragrain J_c, but at higher fields the decrease slows until the intergrain J_c is again comparable to the intragrain values. This "plateau" in higher fields becomes more pronounced at larger θ, being particularly obvious in the 10° bicrystal. By 15°, evidence of a plateau has disappeared.

Figure 5.1 should be compared to the bulk bicrystal data presented in Figures 4.4 and 4.5, where (i) the intragrain J_c decreases approximately linearly with field, and (ii) an abrupt change in the shape of the $J_b(H)$ curves occurs as the strong-to-weak coupling transition is made.

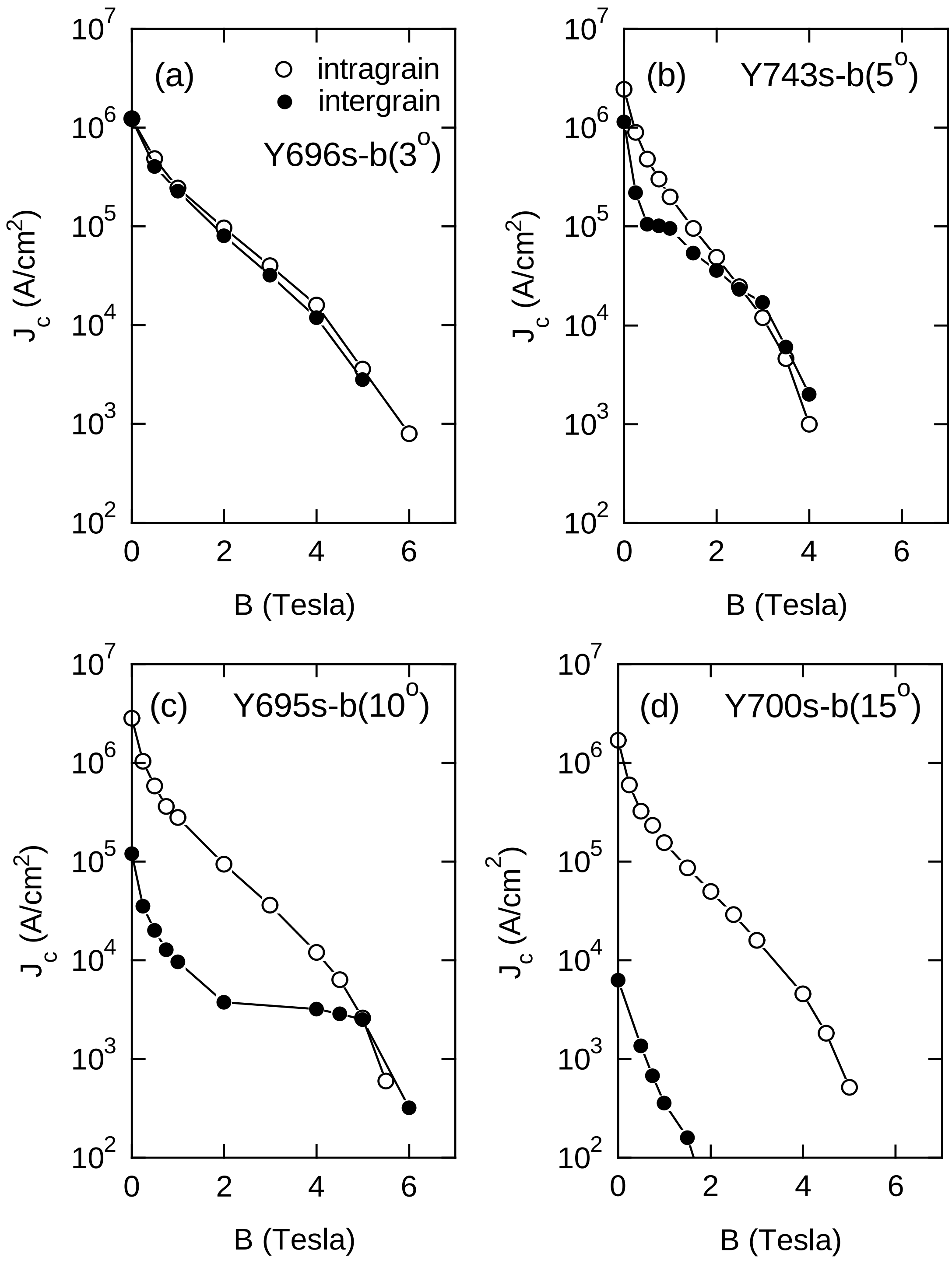

Figure 5.1 Intergrain and intragrain J_c at 77 K, H||c, for (a) 3°, (b) 5°, (c) 10°, and (d)15° thin film bicrystals.

Another point is that the exponential decrease in the intragrain $J_c(H)$ varies significantly from film to film. Since improvements and adjustments were continually being made to the laser ablation system, these differences appear to be primarily due to differences in growth and processing, although some degradation of the films as they are thermally cycled also occurs. This can be illustrated by Figure 5.2, where the $J_c(H)$ curves for three different 7° thin film bicrystals, Y692s-b(7°), Y727s-b(7°), and Y752s-b(7°), are shown. While all the intragrain regions show an approximately exponential decrease in $J_c(H)$, the rate of this decrease can vary considerably from film to film. Table 5.1 indicates whether the bicrystals were attached to the faceplate with Ag epoxy or clamps during growth, and what the faceplate temperature was during film growth, T_{op}, as well as the initial zero field parameters T_c and J_c. These initial J_c values were measured some time before the high field experiments discussed here. These zero field parameters can also be found in Table 3.2. The varying intragrain $J_c(H)$ dependencies of Y727s-b(7°) and Y752s-b(7°) is apparently due to the different growth methods, growth temperatures, and film thicknesses selected.

Table 5.1 Film Growth Parameters

Sample	Date of Growth	Growth Method	T_{op} (°C)	Film thickness	T_c (K)	J_c(0,77K)
Y692s-b(7°)	11/15/94	clamps	871	0.25 μm	87	1.2 MA/cm^2
Y698s-b(7°)	12/13/94	clamps	870	0.25 μm	83.3	0.4 MA/cm^2
Y727s-b(7°)	3/30/95	Ag epoxy	823	0.10 μm	88.8	4.0 MA/cm^2
Y752s-b(7°)	6/22/95	clamps	881	0.10 μm	88.9	3.3 MA/cm^2

The different 7° samples also have varied grain boundary properties, despite having the same misorientation angle. Although a rapid decrease below 1 Tesla and a flattening in high fields is seen in the intergrain $J_c(H)$ of Y727s-b(7°) and Y752s-b(7°), this is not observed in Y692s-b(7°). Instead, as shown in Figure 5.2(a), the inter- and intragrain properties of Y692s-b(7°) appear very similar. As will be seen later, this similarity in $J_c(H)$ corresponds to similarities in the shape of the measured V-I curves.

Another unusual feature of Figure 5.2(b) is that Y727s-b(7°) has a zero field intragrain J_c that is *lower* than the intergrain J_c. In earlier measurements on the same bicrystal, the reverse was true, indicating that the intragrain link had been damaged during testing, perhaps because its longer length, 500 μm versus 100 μm, made it more susceptible to damage.

In Figure 5.3, the effect of aging and/or thermal cycling is shown explicitly when two sets of data on the same bicrystal are compared to each other. Y695s-b(10°) was measured in high fields in March and September, and the deterioration in the interim is clear. The intragrain link showed more damage than the intergrain link, which may reflect the different link geometries. The intragrain link is 10 μm x 500 μm, and the intergrain link shown in Figure 5.3 is 50 μm x 100 μm.

Another issue is the width dependence of the intergrain J_c, which was discussed in Chapter 3. In Figure 5.4, both 10 μm and 50 μm wide intergrain links are shown for Y727s-b(7°). Because of the larger critical currents in the 50 μm link, the wider link's $J_c(H)$ curve has less experimental scatter. For this reason, as bicrystals with increasing misorientation angle were measured and the intergrain J_b(0 T) decreased, wider links were used to measure the in-field properties. In zero applied field the narrower link has a higher J_b, but in high fields the wider link has a larger J_b. This higher J_b in the wide link can be attributed to (i) less processing damage and, (ii) proportionately less thermal noise rounding (TAPS). In zero field, an uneven current distribution causes the larger links to have smaller J_b, but this becomes less important above H_{c1}, when the entire sample is fully penetrated by vortices.

Although most of the high field measurements were taken at 77 K, some experiments were done at other temperatures. In Figure 5.5, the magnetic field is varied at a constant temperature of 65 K, 72 K, 77 K, or 82 K for a 10° thin film bicrystal. The intergrain and intragrain J_c is taken at the same *nominal* electric field value of 1 μV/cm. There are two features of particular interest. One is the cross-over, in high magnetic fields, of the intergrain and intragrain critical current density. This can also be seen in Figure 5.3, and may be due to a combination of the higher electric field at the boundary, and damage to the intragrain link. The other feature is the change in shape with temperature of the "plateau" in the intergrain J_b. At lower temperatures, the change in J_b with magnetic field is the smallest, and the slope gradually increases as the temperature

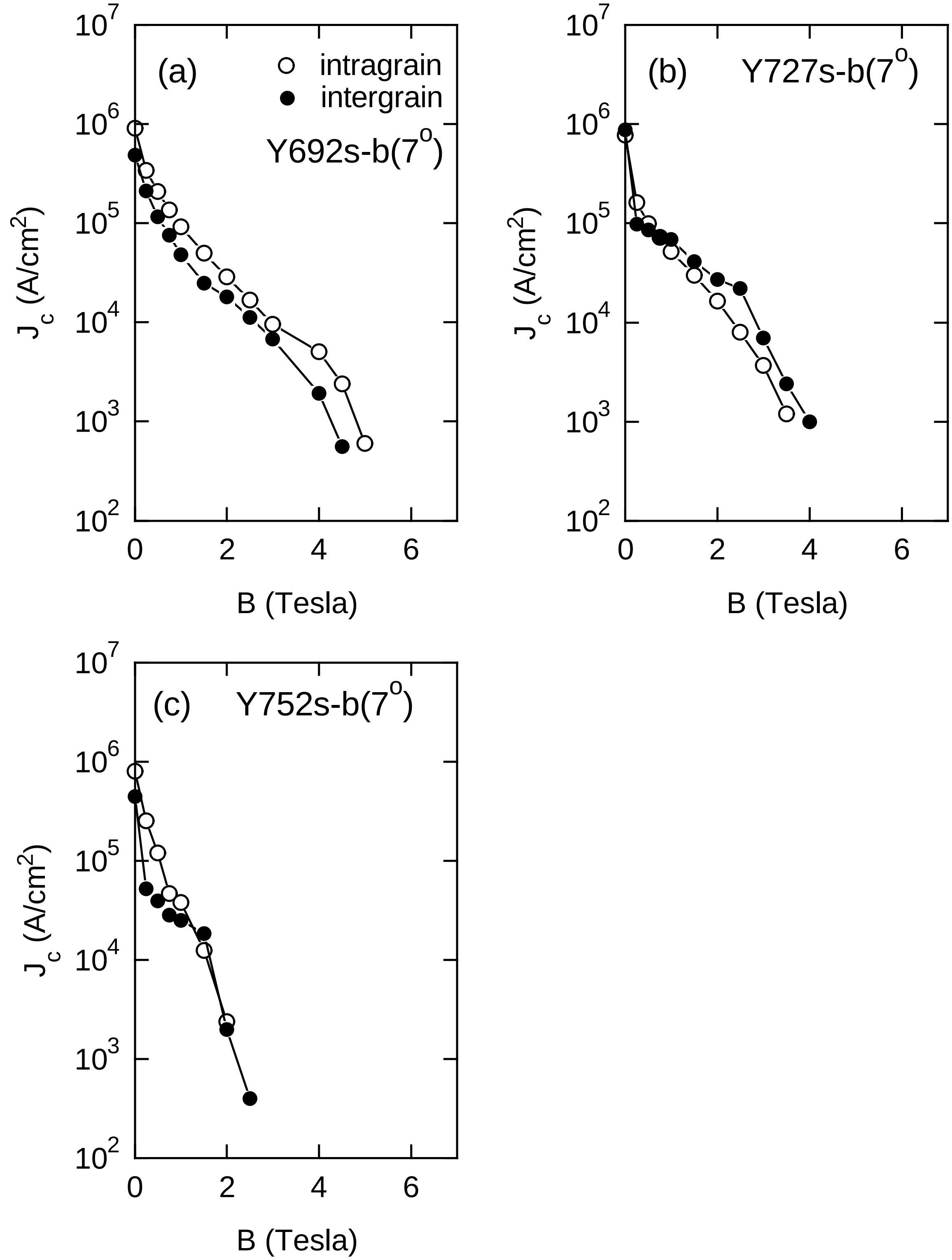

Figure 5.2 Intergrain and intragrain J_c for three different 7° bicrystal films.

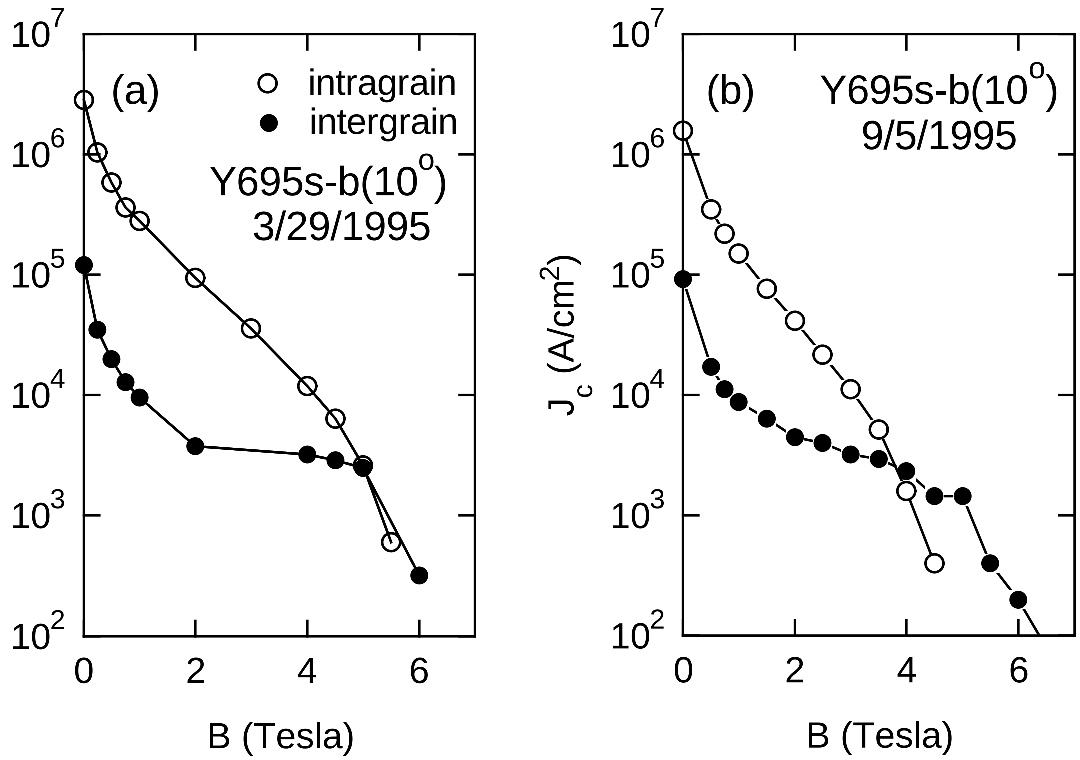

Figure 5.3 A comparison of intergrain and intragrain J_c for a 10° bicrystal film measured at two different times. T = 77 K, H||c.

increases. This may be related to work done by R.D. Redwing et al. [64], on this and a similar 10° thin film bicrystal, which showed a cross-over from RSJ (Resistively Shunted Junction) to flux-flow type behavior as the temperature decreased from 87 K to 75 K. It was conjectured that this change in behavior was due to the change in the relative size of the coherence length with respect to any strongly coupled channels across the boundary.

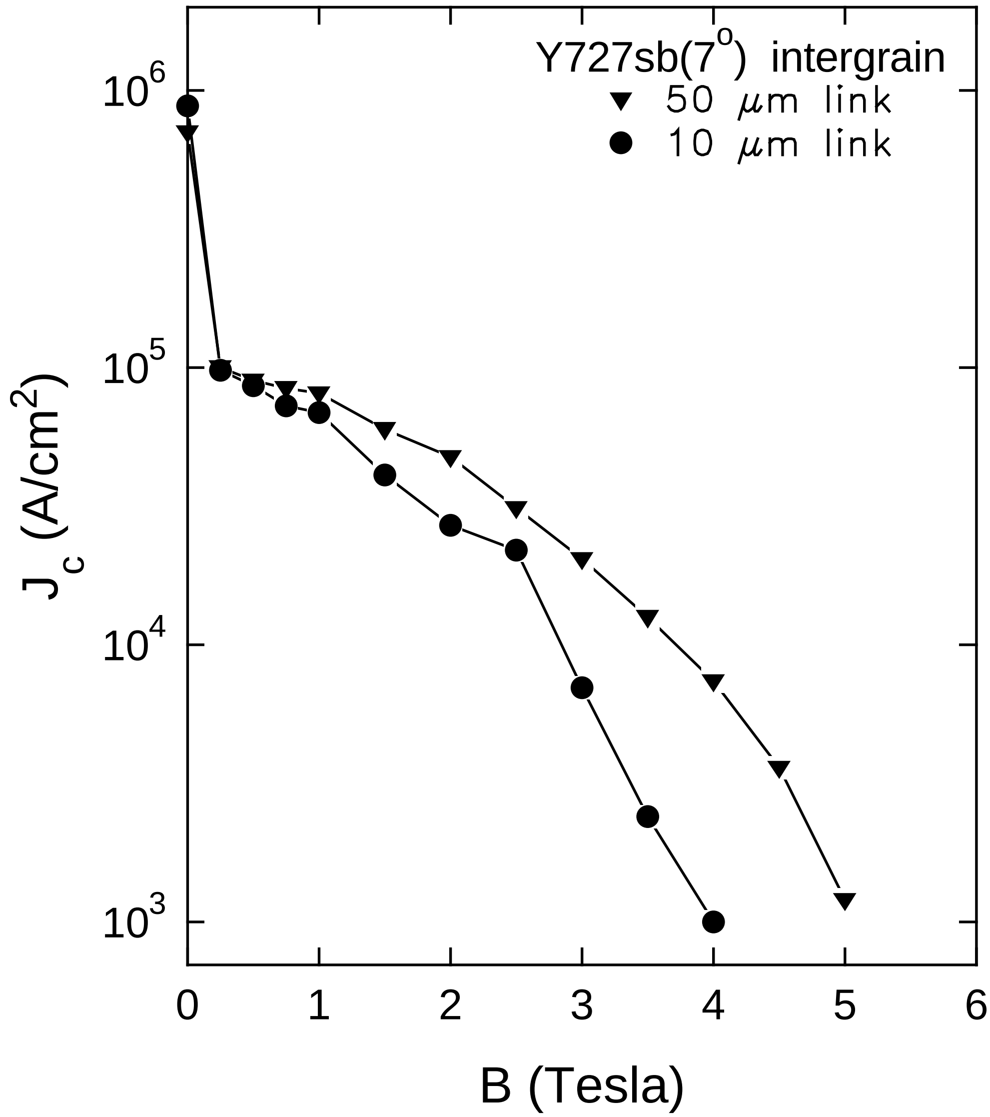

Figure 5.4 The $J_b(H)$ characteristic of a 10 μm and a 50 μm wide intergrain links of Y727s-b(7°), measured at the same time, at 77 K and H||c.

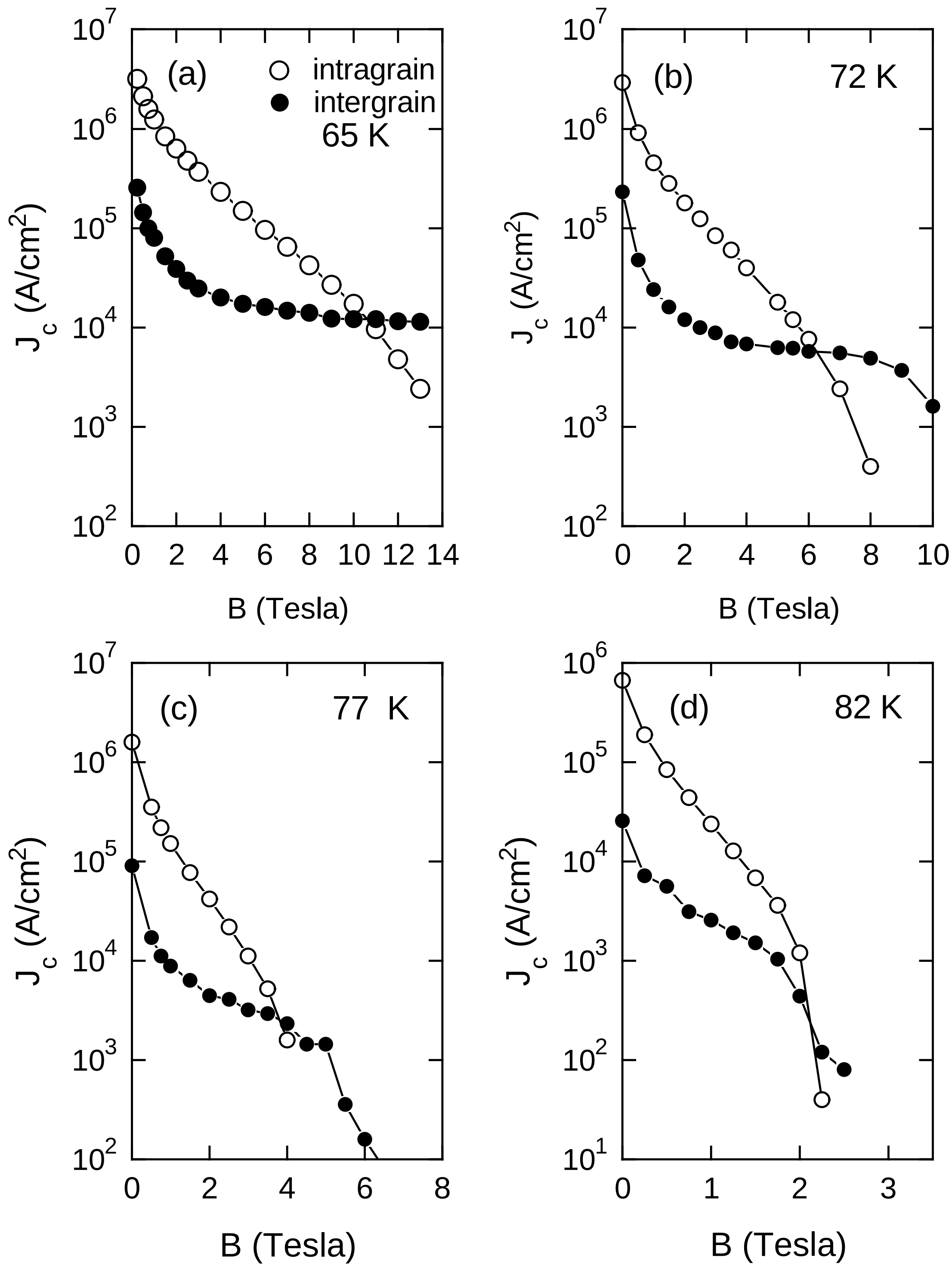

Figure 5.5 Intergrain and intragrain J_c versus applied field, for Y695s-b(10°) at four different temperatures: (a) 65 K, (b) 72 K, (c) 77 K, and (d) 82 K.

Summary of J_c(H) data

The J_c versus H curves at 77 K for bicrystal films with misorientation angles between 3° and 15° are presented. A gradual, progressive change in the J_b(H) curve with increasing misorientation angle can be seen. While the 3° and one of the 7° bicrystals had similar inter and intragrain J_c(H) curves, most intergrain curves had a rapid decrease in J_c in lower fields, followed by a slower decrease, or "plateau" in higher fields. This contrasts with the intragrain J_c, which decreased exponentially with field. No evidence of a "plateau" was observed in the 15° bicrystal. As will also be seen in the analysis of V-I curves, this behavior is consistent with the closure of any strongly coupled channels across the grain boundary between 10° and 15°. These general trends with increasing θ occur despite considerable variations in J_b(H) and J_c(H) from sample to sample and run to run. The geometry of the links also affected the J_c(H) curve, leading to smaller in-field J_b values for the narrower links. While these channels remain open, the evolution of the shape of the J_c(H) curve with angle can be understood in terms of an electric field argument, which will be discussed in the next section.

The Electric Field and Pinning Force curves

With increasing θ, the intergranular J_b(H) curves deviate increasingly from the shape of the corresponding intragranular J_c(H). What causes the more rapid decrease in J_b(H) in low fields, and the "plateau" feature in higher fields typical of these grain boundaries? From the zero field data discussed in Chapter 3, there is clear evidence of weak coupling at misorientation angles of 10° and 15°, and there is some evidence of weak coupling at 5° and 7°. This weakly coupled contribution to J_b is expected to decrease very rapidly with applied magnetic field, but it is not clear what proportion of the total J_b is due to weak coupling. One motivation for studying these bicrystals in high magnetic fields was to reduce effects due to weak coupling and thus to emphasize the contribution from the strongly coupled regions of the grain boundary.

In the simple channel model of a low angle grain boundary discussed in Chapter 1, contributions to J_b from any weakly coupled regions are neglected. The boundary consists of "good" channels, with the same superconducting properties as the intragranular region, and "bad" channels that are not superconducting. A consequence of this model is that as the percentage of good channels decreases, voltage dissipation becomes more localized at the grain boundary, instead of being distributed across the entire link, as would occur in an intragranular transport measurement. Thus, a given voltage drop for an intergrain link corresponds to a much higher electric field across the grain boundary than it does across the intragranular link.

One way to study high field transport is by looking at the pinning force curves, F_P versus B, where $F_P = J_c \times B$. The advantage of studying $F_P(H)$ instead of $J_c(H)$ is that attention is naturally focused onto the flux pinning component of the transport properties because the low field data, which have a significant weakly coupled component, are de-emphasized. By comparing the intragrain F_p versus B curves taken at different voltage criteria, one can see the peak in F_p moves to higher magnetic fields as the electric field increases. In the intergrain $F_p(H)$, there is also a trend for the main peak in F_p to move to higher B as the misorientation angle increases, up to about 10°. This agrees with the channel model of the grain boundary, where, at a constant voltage drop, the electric field should become higher at the grain boundary as the number and size of good channels decreases.

In the intragranular regions of our thin films, the pinning force curve best fits the form $F_p \propto b^{0.5}(1-b)^2$, where $b = B/B_n$ is the reduced magnetic field, and this functional form is characteristic of shear-limited pinning [74]. This form has earlier been shown to be appropriate for $YBa_2Cu_3O_{7-x}$ films [75]. The change in the peak position of $F_p(H)$ with increasing electric field is illustrated in Figure 5.6, where F_p versus B of a single intragrain link in Y727s-b(7°) is shown for J_c defined at different voltage criterions. As the voltage criterion for J_c is increased, the peak in the pinning force curve moves to higher magnetic fields. All the curves were fit to $F_p = Ab^{0.5}(1-b)^2$, where A is a fit parameter, and $b = B/B_n$, and the results are shown in Table 5.2. The peak in F_p, B_{max}, is then found, by differentiation, to occur at $B_n/5$. The peak field, and the electric field that corresponds to that B_{max}, are also shown in Table 5.2.

Table 5.2 Pinning Force Curve Data for Y727s-b(7°)

Voltage Criterion	A	B_n (T)	B_{max} (T)	E Field Criterion
0.1 μV	2.12	4.32	0.864	2 μV/cm
1 μV	3.42	5.47	1.09	20 μV/cm
10 μV	5.70	6.91	1.38	200 μV/cm
100 μV	9.87	8.74	1.75	2000 μV/cm

In Figure 5.7, the normalized intergrain F_p vs. H curves for films with θ ranging from 3° to 10° are shown. These curves have more scatter, in part because of the lower critical currents, and clearly do not have the same shape. The main peak in $F_p(H)$ moves out to higher fields as the misorientation angle is increased, consistent with an increasing electric field across the good, open channels of the grain boundary. The irregularities in the low field regions of the 5° and 10° curve can be attributed to contributions to J_b from weakly coupled regions of the GB.

It is possible to estimate the effective width of the grain boundary by assuming that transport across low angle grain boundaries is via good channels having the same properties as the bulk. The peak position, B_{max} in the intergranular pinning curve corresponds to an electric field across the GB similar to what is seen in Table 5.2. Once the electric field is known from B_{max}, one can calculate the effective width of the boundary. For the Y727s-b(7°) intergrain link, $B_{max} \approx 2.0$ T, at a voltage criterion of 0.01 μV. Extrapolating from the intragrain values shown in Figure 5.8 and Table 5.2, this corresponds to an electric field of about 1 x 10^6 μV/cm and an effective grain boundary width is 1-10 nm. These estimates could be improved by taking the intragrain curves out to higher voltages. Unfortunately, because each film has a different intragrain pinning curve, each bicrystal would have to be analyzed independently.

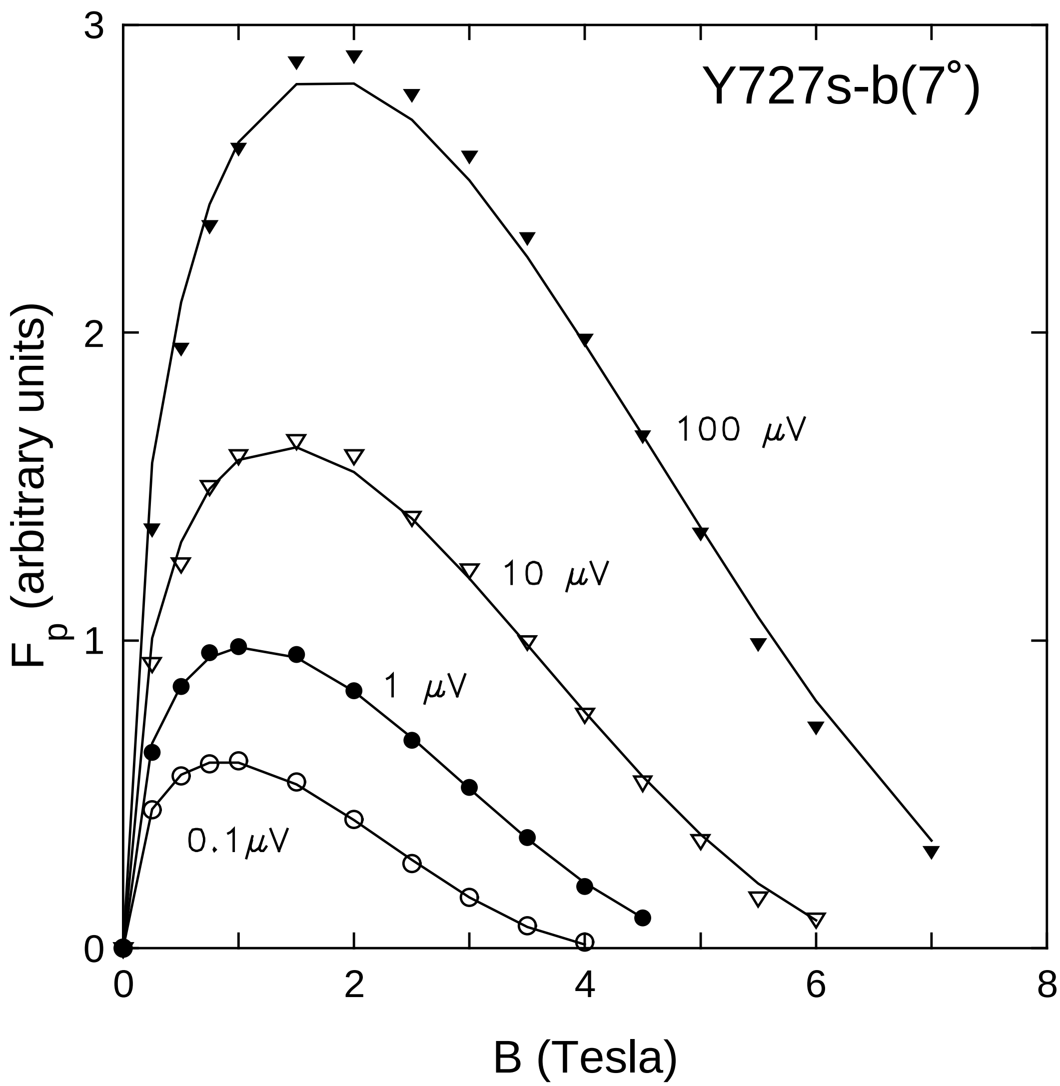

Figure 5.6 F_p versus B for a single intragrain link, calculated at different voltage criterions, all at 77 K and H||c. The symbols indicate the data, and the lines are fits to $F_p = Ab^{0.5}(1-b)^2$, b=B/B_n.

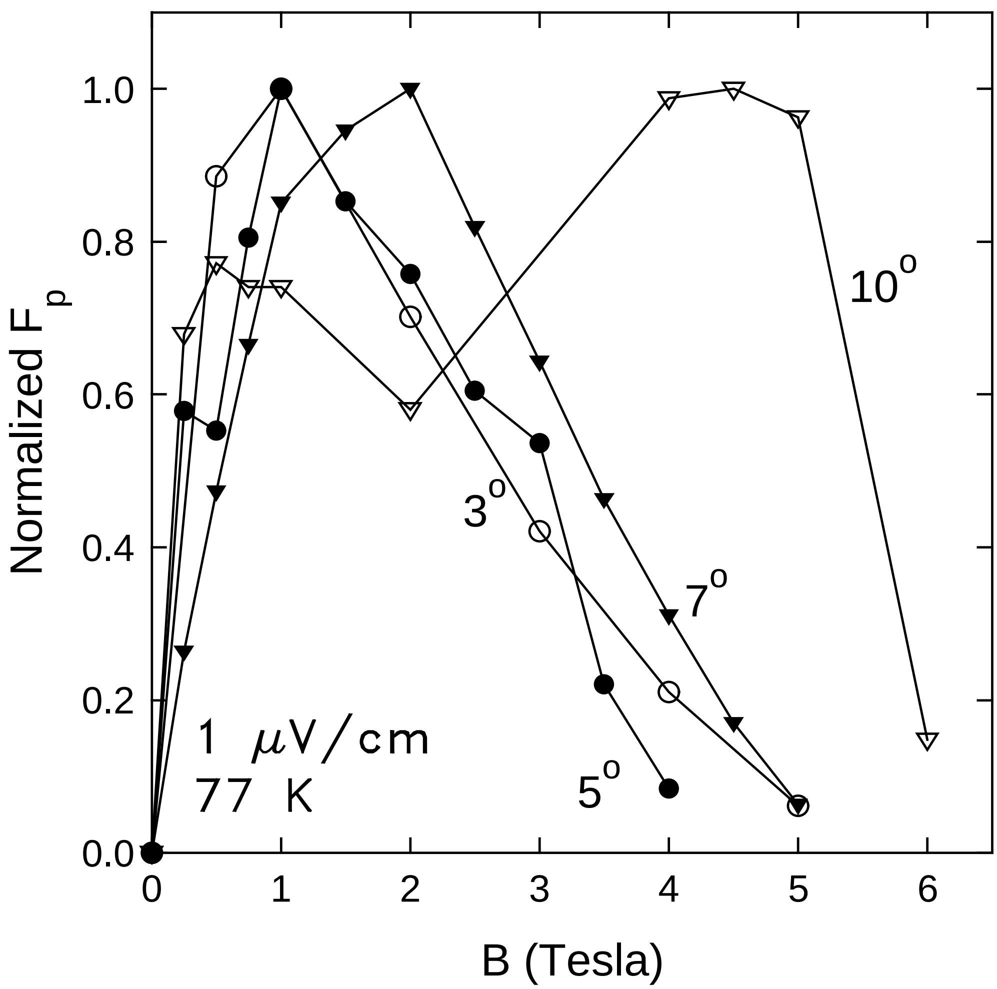

Figure 5.7 F_p versus B for the intergrain links in Y696s-b(3°), Y743s-b(5°), Y727s-b(7°), and Y695s-b(10°) bicrystal films. The voltage criterion is 1 μV/cm, T = 77K, H||c.

This simple electric field argument can explain how the intergranular $J_b(H)$ and $F_p(H)$ curves differ from their corresponding intragranular curves. However, for some samples like Y692s-b(7°), the inter and intragrain $J_c(H)$ are very similar, and the peak in the pinning force does not move appreciably. For these cases one can conclude that the grain boundary does not act to restrict the supercurrent. This may be due to a poorer quality intragrain region limiting the current fed into the grain boundary. In order to distinguish between a grain boundary consisting of strongly coupled channels in parallel with non-superconducting elements, and one consisting of a continuous weakly coupled barrier, it is necessary to look at the entire V-I curve, and how it evolves in field.

Extended E-J Curves

In order to better understand the high field transport behavior, the shape of the entire V-I curve and how it changes in applied magnetic field should be studied. In Chapter 4, the irreversibility field, H*, was defined as the field at which a measurable voltage across the superconductor is generated at vanishingly small currents. In bulk [76,77], and thin film single crystal [78, 79] high temperature superconductors, H* has been found experimentally by the change of curvature of the V-I curve, plotted on a double logarithmic scale. In single crystal $YBa_2Cu_3O_{7-x}$ thin films, H* occurs near 4 Tesla at 77 K [78]. This is somewhat smaller than the H*(77 K) values seen in bulk $YBa_2Cu_3O_{7-x}$, which may be due to the lower T_c values (89 K versus 92 K) of the films compared to the bulk.

Dislocation core models postulate that channels of undisturbed crystal lattice lie between the grain boundary dislocation cores, up to some critical misorientation angle, θ_c. Below this critical misorientation, the transport properties through the channels should be similar to that through the intragrain regions. At sufficiently low voltage dissipation levels across the grain boundary, the V-I characteristic will be controlled by the properties of these strongly coupled channels. By identifying H* from the low voltage intergranular V-I characteristic, and comparing it to the corresponding intragranular H*, the misorientation angle at which the intergrain H^*_{GB} becomes much less than H^*_{Grain} corresponds to θ_c and the closure of the strongly coupled channels in the grain boundary.

Magnetic Field Dependence of the E-J curves

In the following section, the voltage-current density (V-J) curves of the thin film bicrystals at 77 K are plotted on a double logarithmic scale. The shape of the V-J curve is discussed in terms of vortex motion. The effect of θ, sample growth, and link width on the V-J curve is discussed. Unexpected voltage oscillations were observed in moderate magnetic fields of 0.25 to 1.5 Tesla. H* was extracted by fitting the V-I curve and determining where the fitting function changes curvature. This procedure is discussed in greater detail in the next section.

In Figure 5.8, the extended V-J curves of an intragranular link at 77 K are plotted. The curves are smooth and almost linear on the double logarithmic scale, and there is a gradual transition from curving downwards at low fields, to curving upwards at high fields. The field at which the curvature changes sign, corresponding to H*, is near 3 Tesla, close to the value Koch et al. [78] measured in single crystal thin film $YBa_2Cu_3O_{7-x}$. Note that this H* of 3 Tesla corresponds to a $J_c(1\ \mu V/cm) \approx 10^4\ A/cm^2$ in Figure 5.3.

Figure 5.9 shows the intergranular V-J curves for a 3° bicrystal. Figure 5.10 and Figure 5.11 show the intergranular V-J curves for two different 5° bicrystals. The curves are already more closely spaced together in moderate fields than the intragranular curves, corresponding to the plateau in the $J_c(H)$ data discussed above. At low voltage levels, the V-J curves show the change in curvature displayed by the intragranular curves. However, at higher voltage levels the V-J curves also appear slightly bent in the double logarithmic plot. This corresponds to a cross-over to a linear, flux-flow type of vortex motion. At high magnetic fields above H*, the bend in the V-J curve disappears. This can be understood as due to increased dissipation in the intragranular portions of the link, which obscures the contribution from the boundary. These features became more pronounced as θ increased, being particularly easy to distinguish in the 10° bicrystal.

Figures 5.12, 5.13 and 5.14 are the V-J curves from three different 7° bicrystals. They show that the shape of the curves can vary considerable for different films with a given θ. Figure 5.12, from Y692s-b(7°) shows very little cross-over to a linear V-J curve, and also has a $J_c(H)$ curve, seen in Figure 5.2(a), quite similar to that of the intragrain. Figure 5.15 is from a 10° bicrystal and perhaps best displays the unique features of intergranular V-J curves. At this angle, voltage noise in the grain boundary becomes particularly noticeable between 0.25 and 2 Tesla.

In the higher angle 15° and 20° bicrystals, shown in Figure 5.16 and 5.17, the V-J curves have become qualitatively different. No evidence of a plateau in $J_c(H)$ is observed. Rather, the H* of the boundary is much depressed when compared to the intragrain regions: H* being between 0.5 and 1 Tesla for the 15°, and no low voltage downward curvature of the V-J curve was observed even at 0 Tesla for the 20°. The high angle GB V-J curves also rapidly became completely linear in field, indicating that the boundary had become resistive well before vortices in the intragrain region became unpinned. The voltage noise observed in the 10° bicrystal has also become much more pronounced, so much so that the 20° bicrystal was measured in liquid nitrogen, in a high stability 1 Tesla magnet, to reduce the noise.

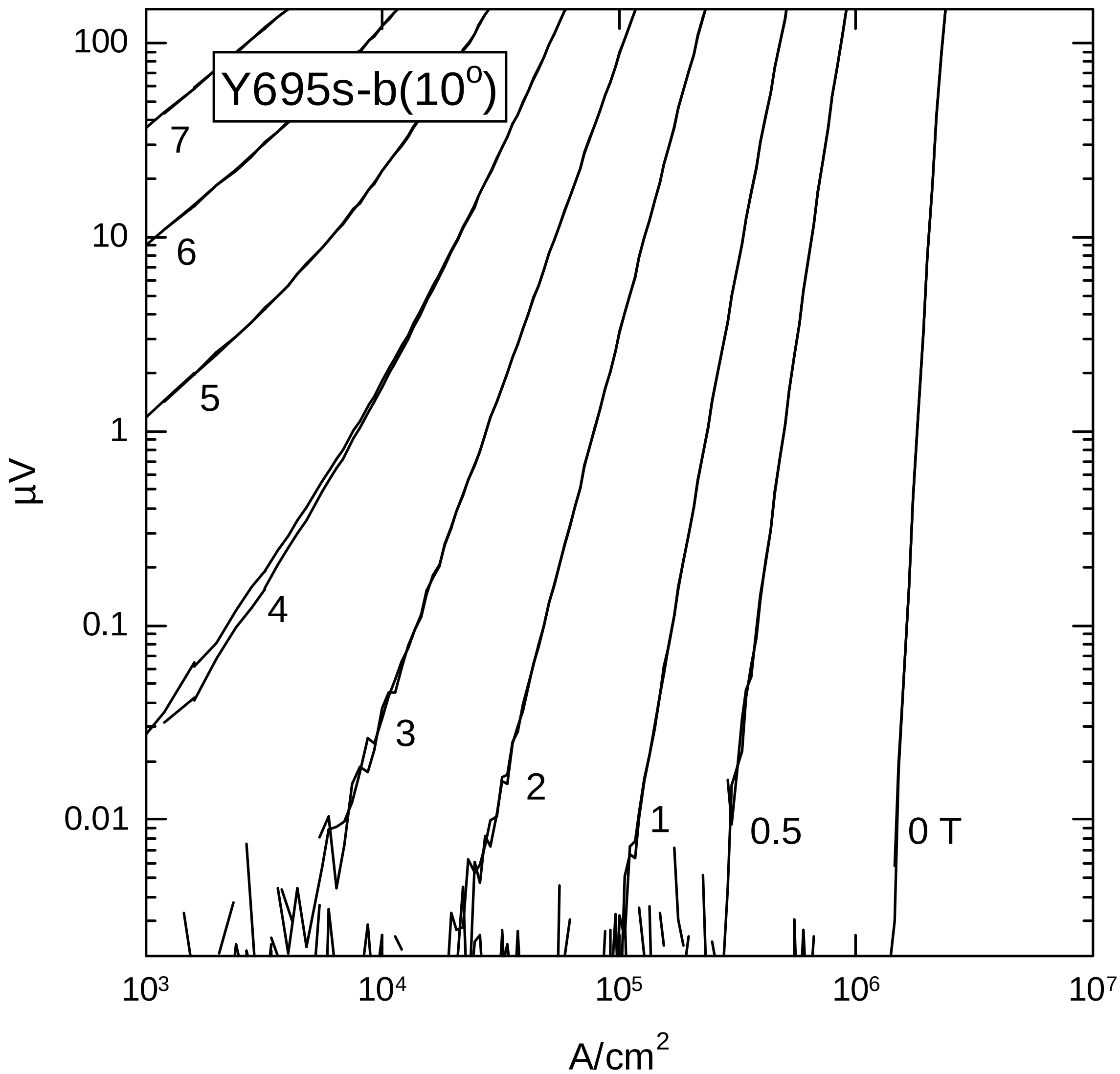

Figure 5.8 V-J curves for a 10 μm wide intragrain link at 77 K, H||c.

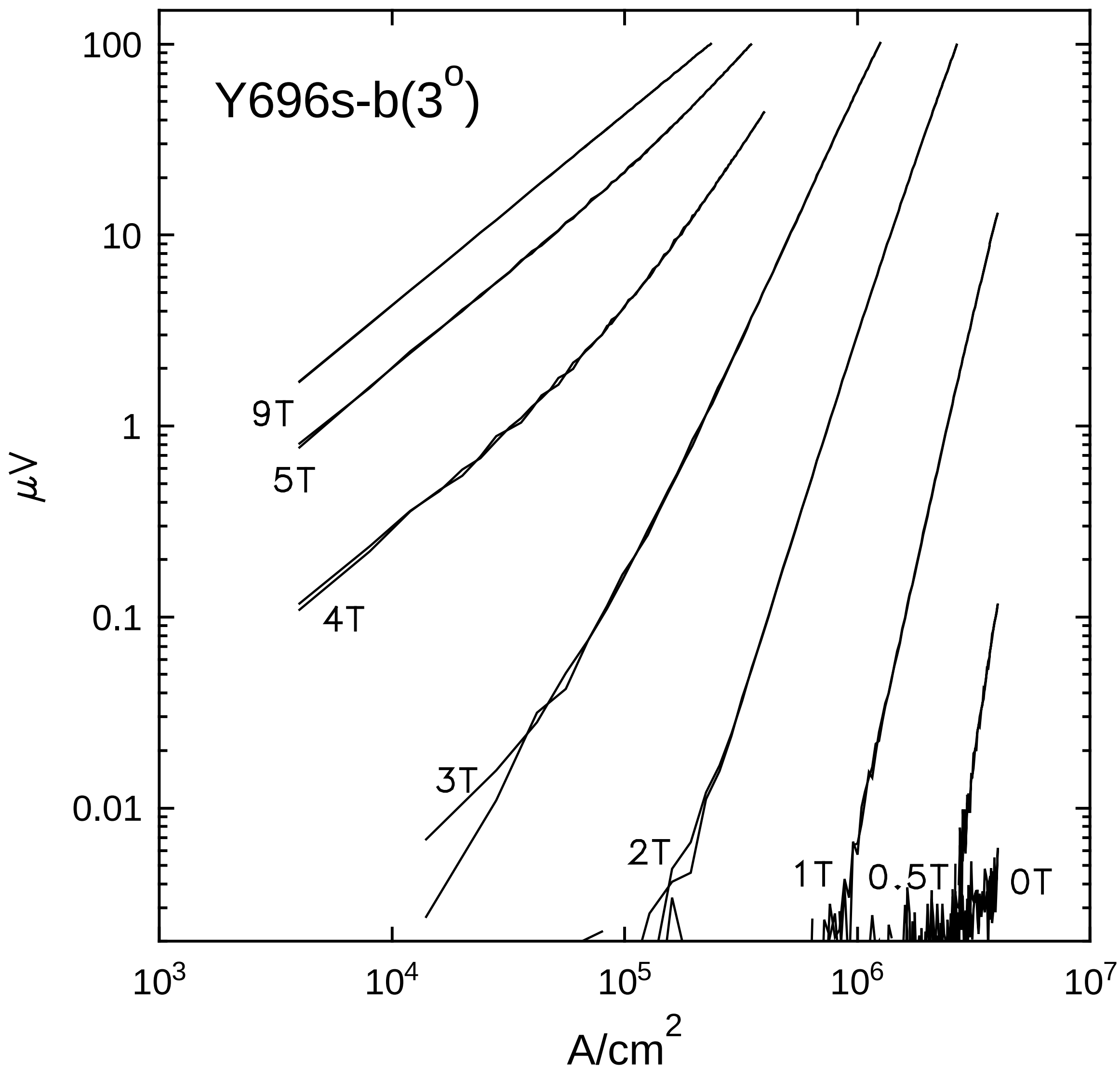

Figure 5.9 V-J curves for a 10 μm wide 3° intergrain link at 77 K, H||c.

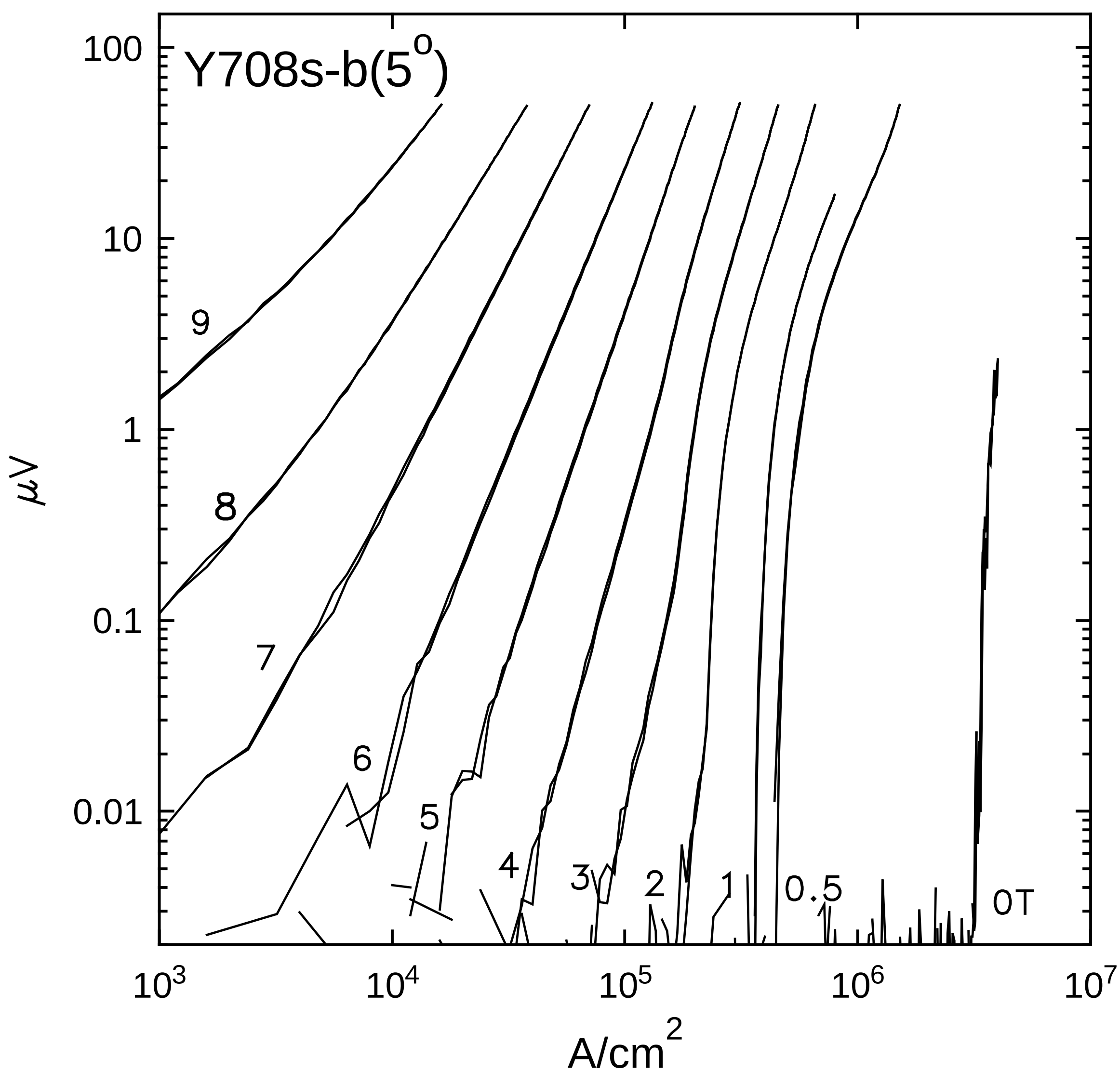

Figure 5.10 V-J curves for a 10 μm wide 5° intergrain link at 77 K, H||c.

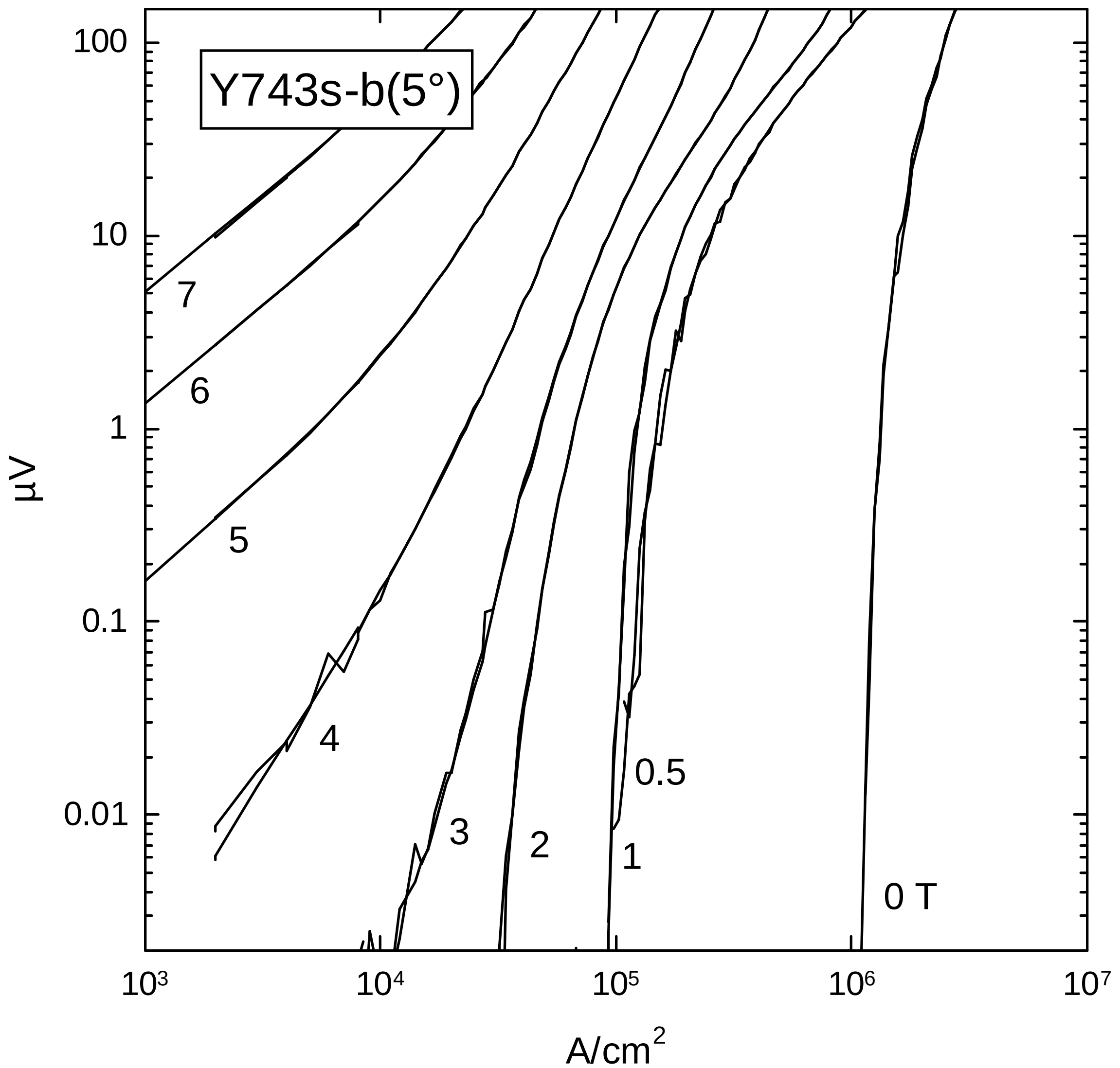

Figure 5.11 V-J curves for another 10 μm wide 5° intergrain link at 77 K, H||c.

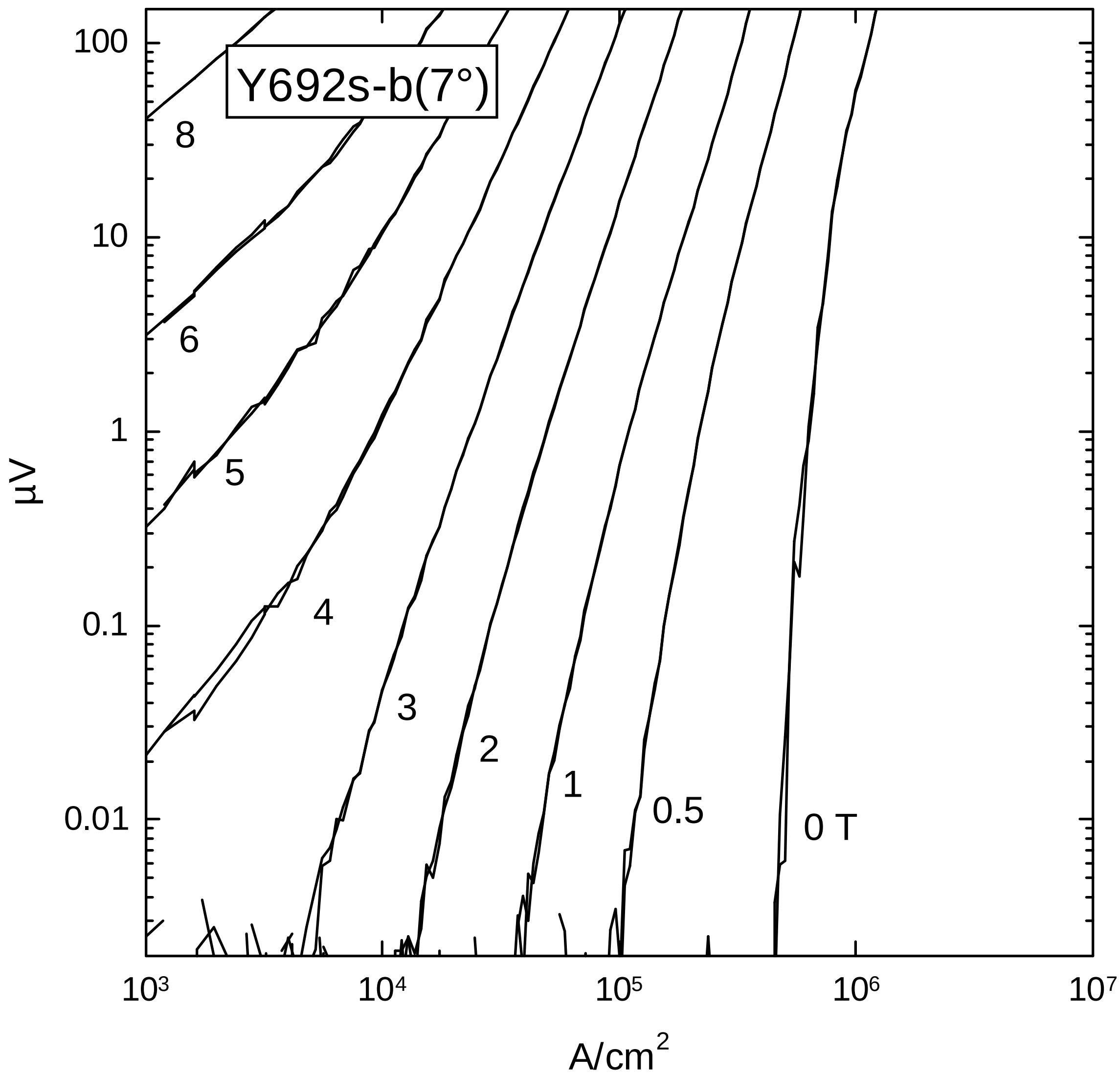

Figure 5.12 V-J curves for a 10 μm wide 7° intergrain link at 77 K, H||c.

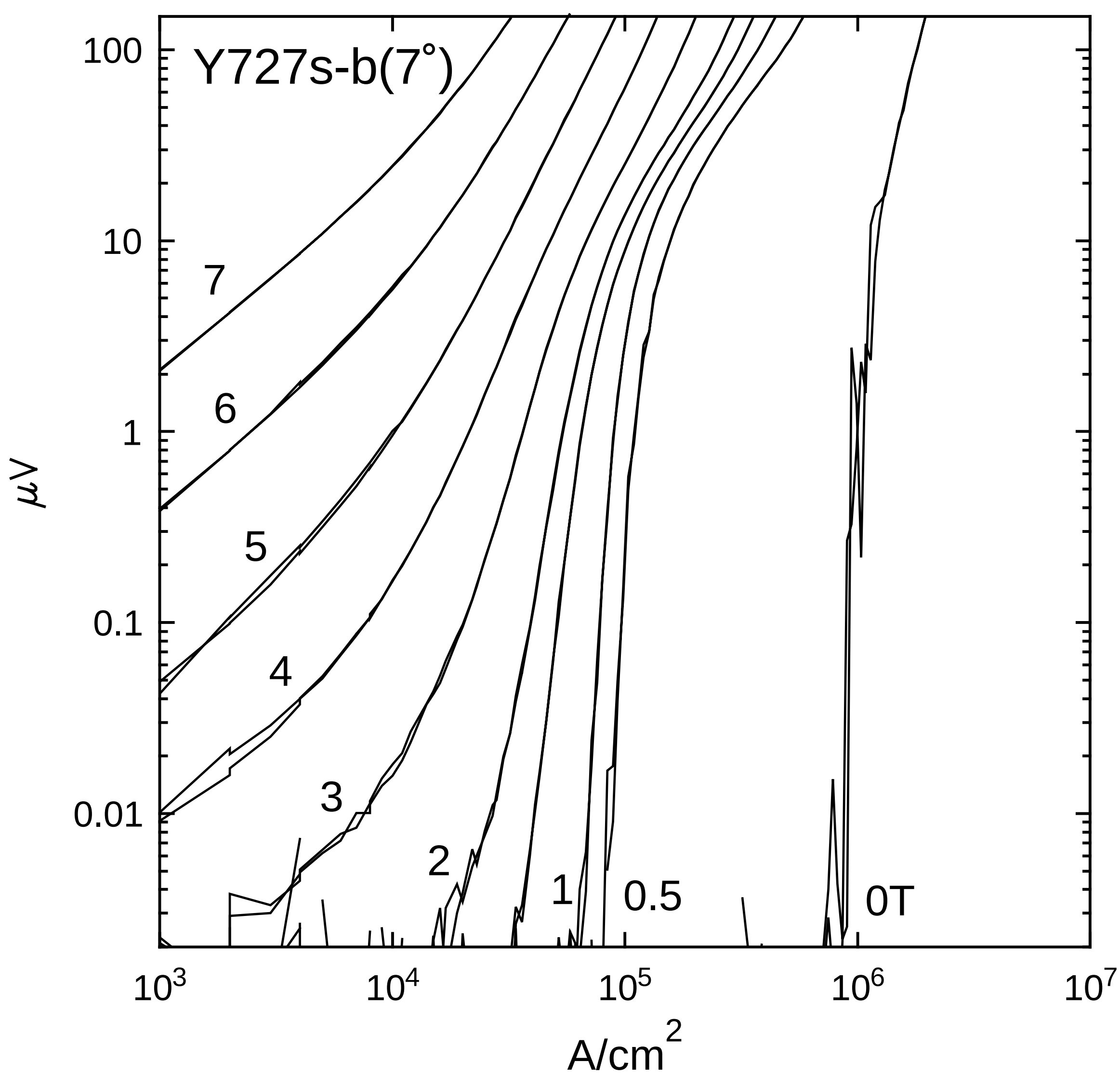

Figure 5.13 V-J curves for another 10 μm wide 7° intergrain link at 77 K, H||c.

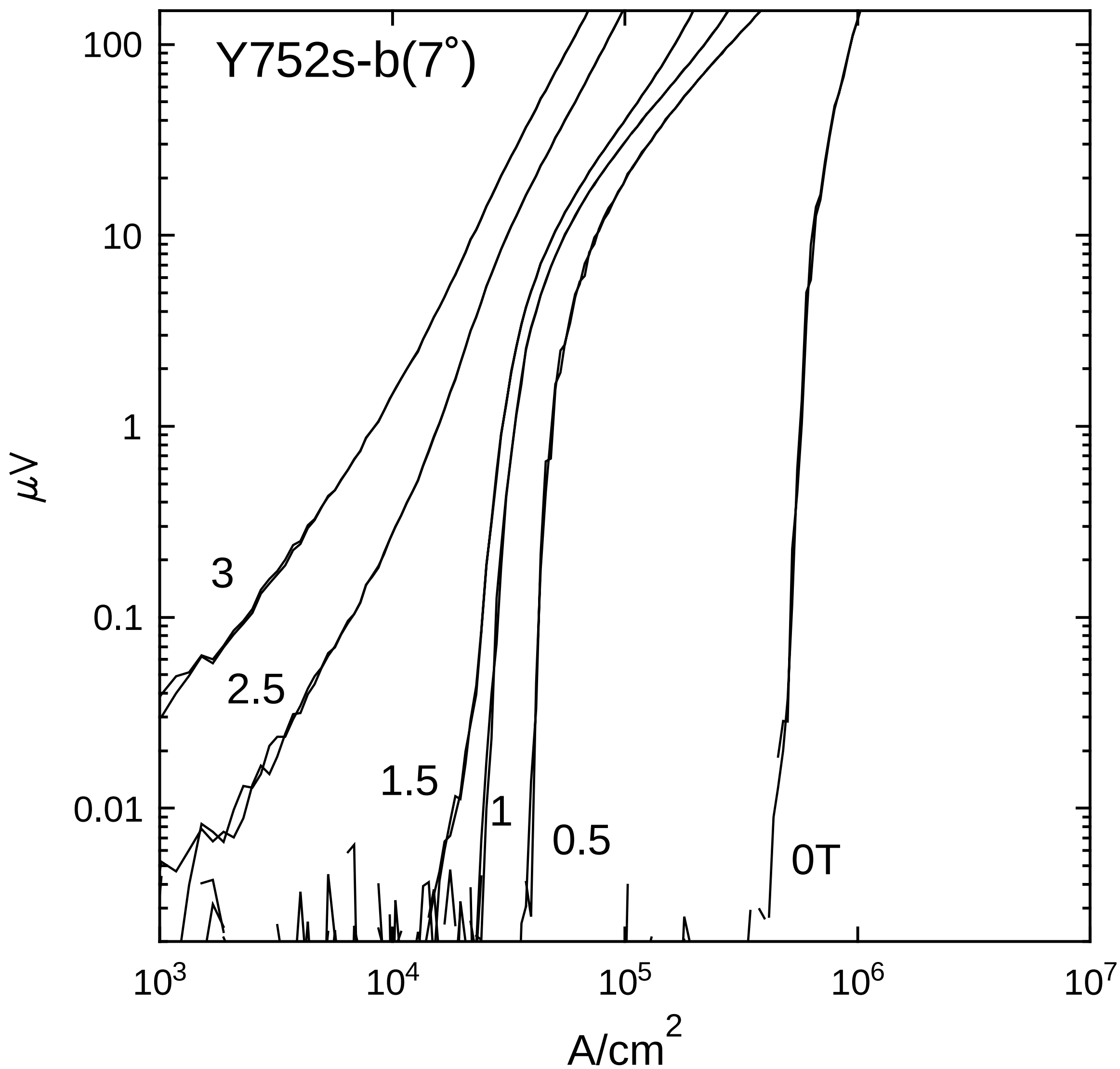

Figure 5.14 V-J curves of a 50 μm wide 7° intergrain link at 77 K, H||c.

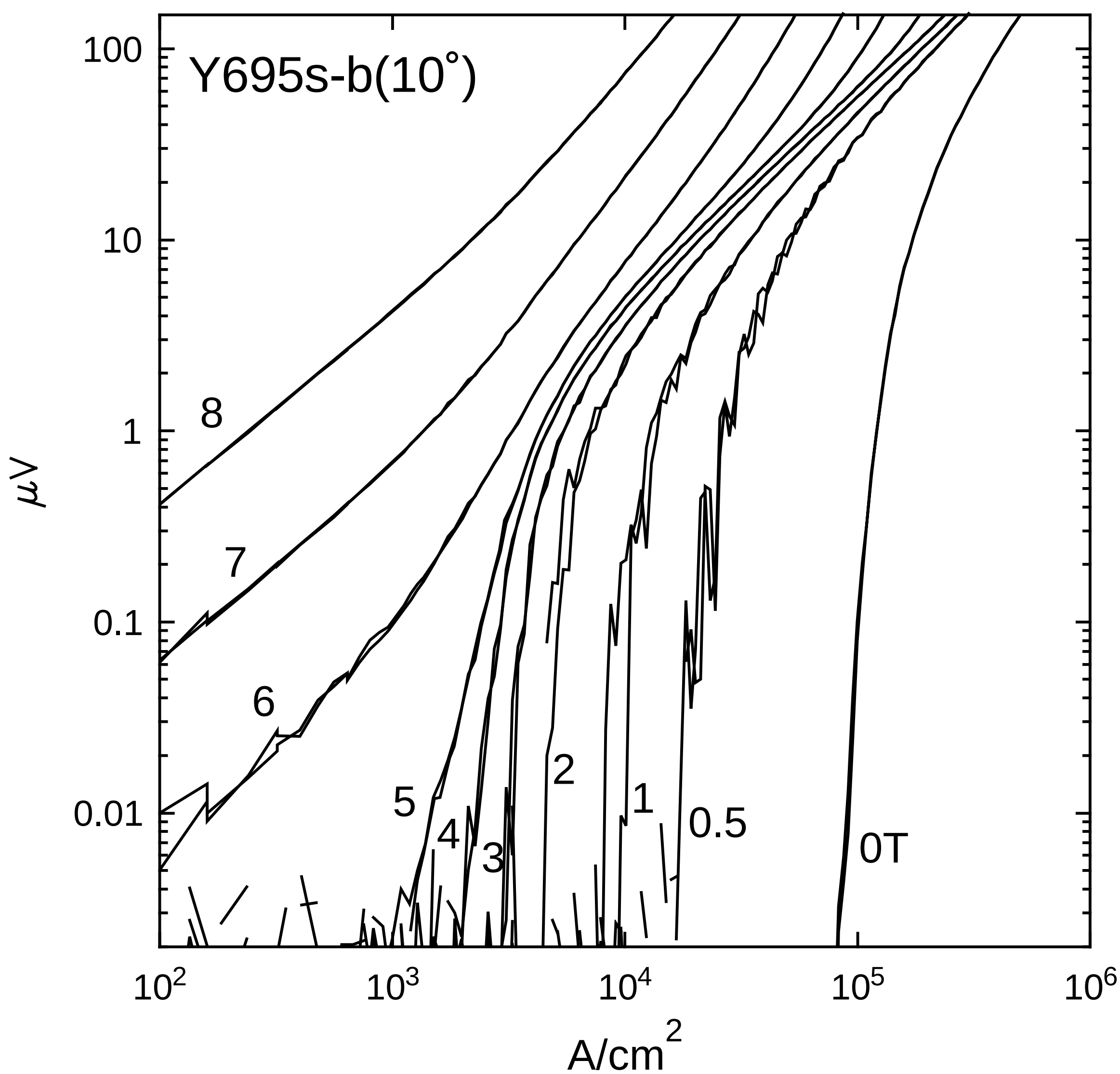

Figure 5.15 V-J curves of a 50 μm wide 10° intergrain link at 77 K, H||c.

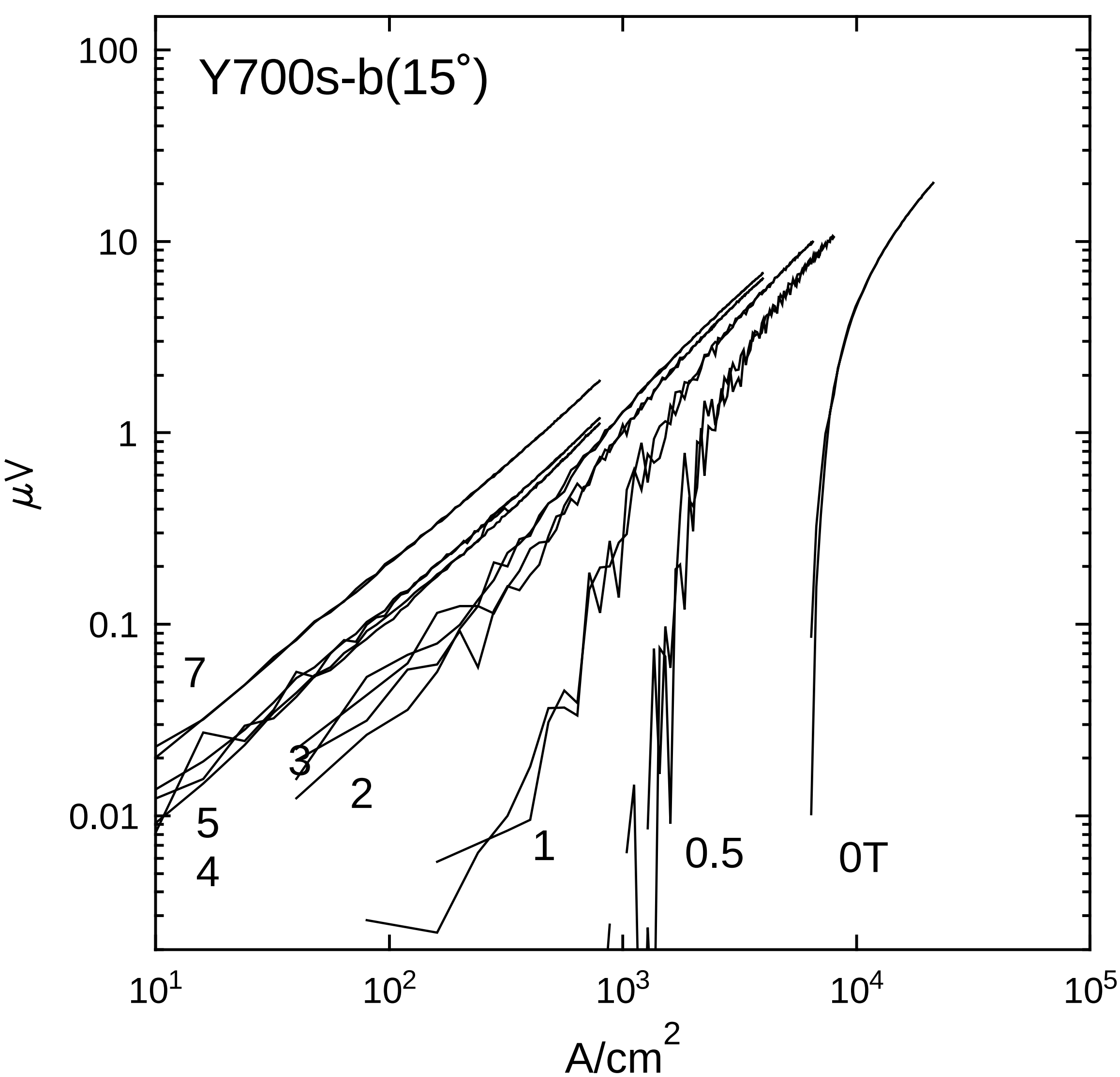

Figure 5.16 V-J curves of an 100 μm wide 15° intergrain link at 77 K, H||c.

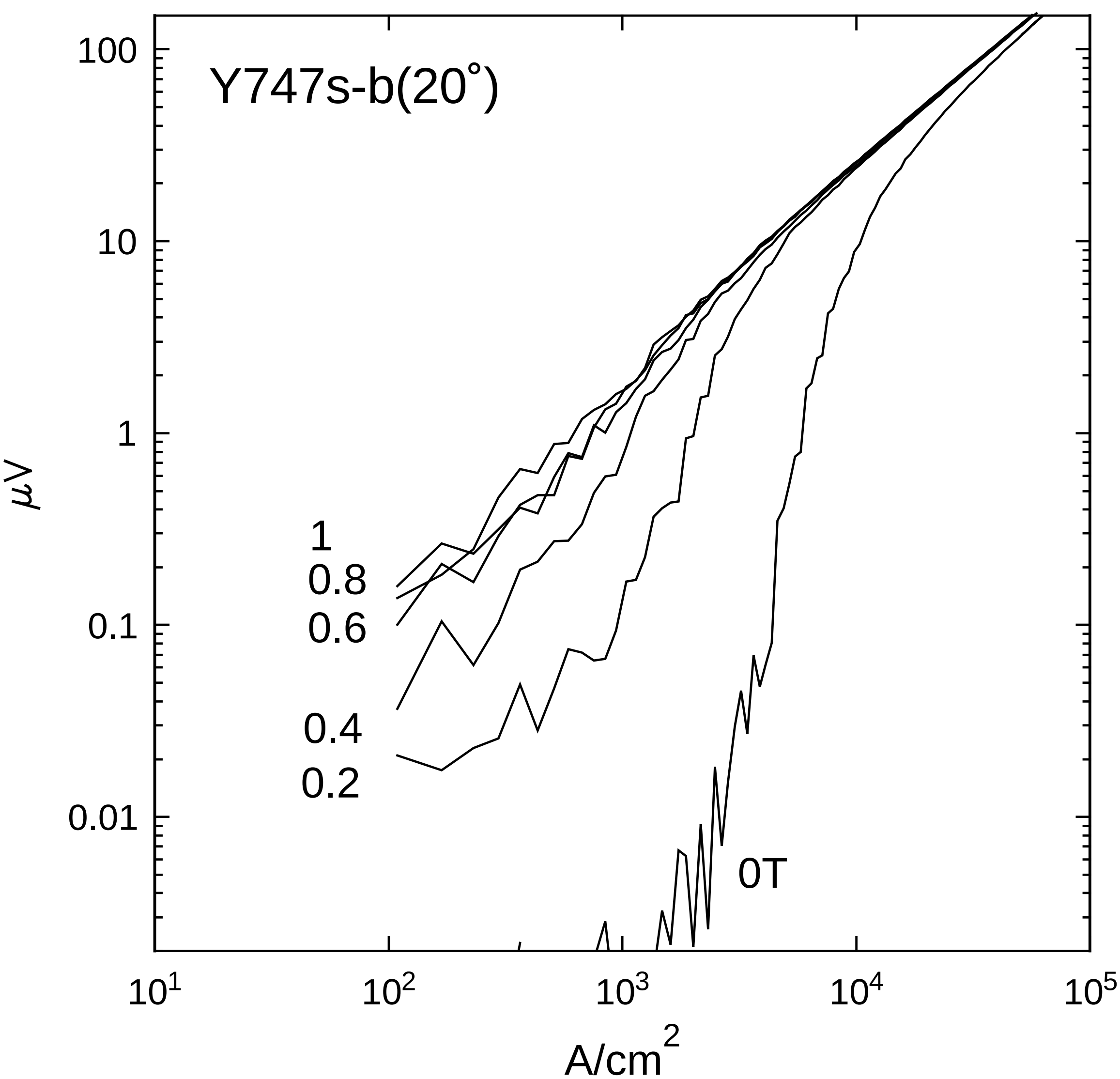

Figure 5.17 V-J curves of an 100 μm wide 20° intergrain link at 77 K, H||c.

The large voltage noise seen in the fields of 0.25 to 2 Tesla in many of the bicrystals deserves comment. These oscillations of several microvolts were particularly evident in higher angle bicrystals. This noise was not seen in the intragranular link, nor was it observed at currents below the critical current, and it also decreased gradually with increasing voltage. These effects were quantified in an experiment on Y743s-b(5°), done in the Oxford magnet. In this straight dc measurement, 200 data points were taken at a constant current, at one of three different average voltage levels, and the standard deviation calculated. All measurements were at 77 K. The standard deviation is plotted versus field in Figure 5.18, and the typical and maximum noise levels of the intragrain link are indicated by the horizontal straight lines.

The most likely source of this voltage noise appears to be field oscillations of less than a mT in the superconducting magnet. These small field variations could have a large effect on the J_c of any weakly coupled components of the grain boundary, producing the observed oscillations in voltage. At larger magnetic fields, any Josephson-type coupling would be suppressed, reducing the voltage noise. At higher voltage levels, a weakly coupled V-I curve more closely approximates a resistive line, and the voltage changes little as the critical current changes. Thus, magnetic field oscillations in the Oxford II magnet would explain the features observed in Figure 5.18. This led to the 15° and 20° bicrystals being measured in a 1 Tesla Cu magnet, stable to ±0.4 Gauss, which much reduced the anomalous voltage noise.

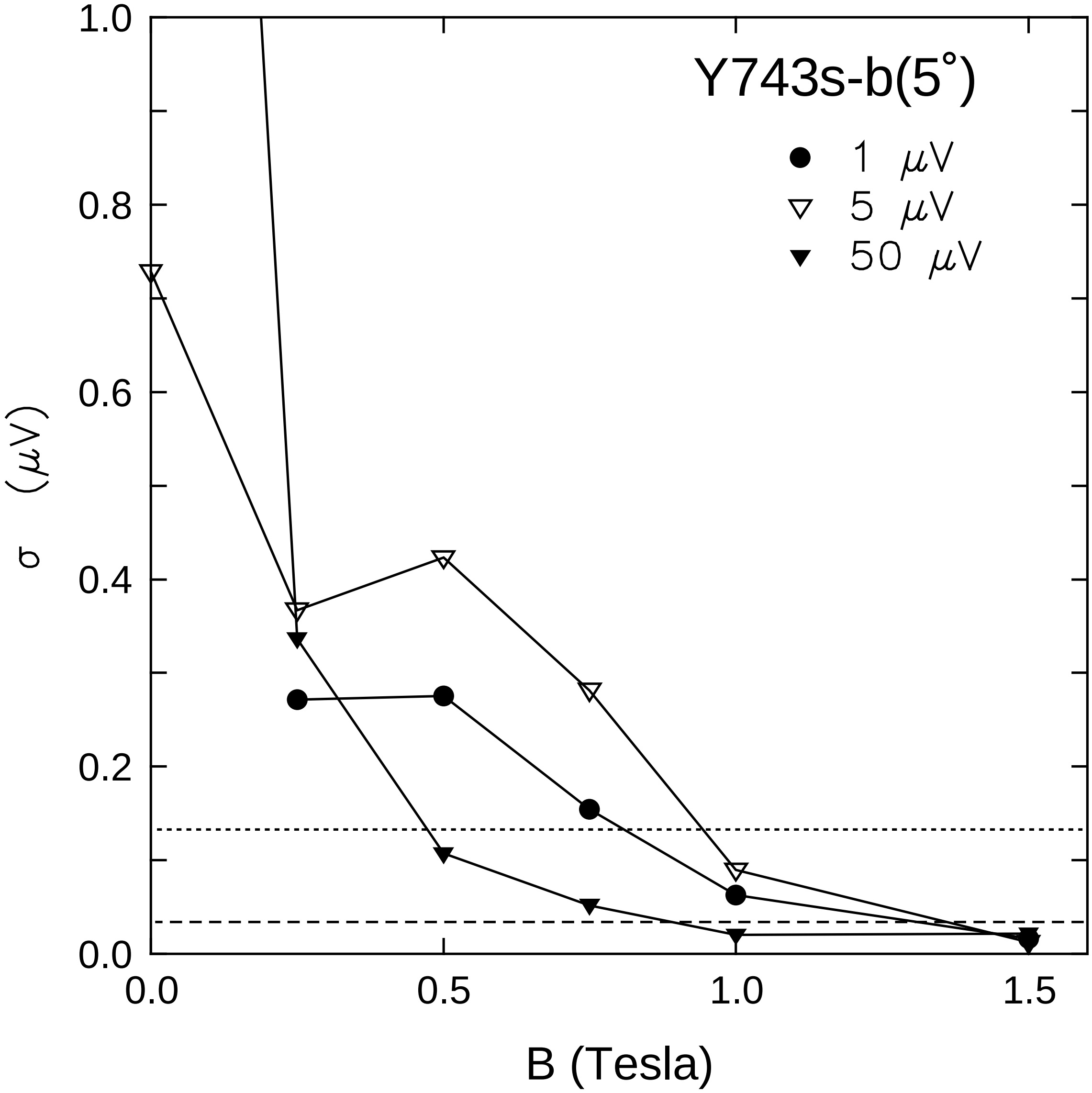

Figure 5.18 Standard deviation, σ, of the voltage across a 5° intergrain link as a function of applied field. A constant current was applied so that one of three average voltages was selected. The horizontal lines are the typical and maximum voltage deviations measured across the intragrain link. T = 77 K, H || c.

Fitting the E-J curves

While it is possible to estimate H* simply by looking at the change in the low voltage curvature in Figures 5.8-5.17, a more quantitative approach is desirable. Two techniques for analyzing single crystal and polycrystalline V-I data are: (i) normalizing the data so that the V-I curves collapse onto two universal curves [78,80] and, (ii) fitting the data to a modified Ambegaokar-Halperin function [81]. The first technique aims to collapse the V-I curves taken at constant field and varying temperature onto two branches of a scaling function, and the transition temperature occurs where the V-I curves switch from one branch to the other. This irreversibility temperature determines where the vortex glass/ vortex liquid phase transition occurs. This thesis work was more concerned with using H* and T* as material characterization parameters, rather than input in a vortex-lattice dynamics model, so a simpler approach was desired. In addition, the flux-flow, linear cross-over at higher voltages observed in the bicrystals with $\theta > 3°$ made collapsing the V-I data onto two curves problematic.

The original Ambegaokar-Halperin (A-H) model added the effects of thermal noise rounding to an ideal resistively shunted Josephson junction in zero magnetic field. The modified A-H model uses these equations to describe a superconductor in large magnetic field by replacing the noise parameter, $\gamma = E_J/(k_B T)$, with the pinning potential, U(H,T). The Josephson coupling energy is E_J, and $k_B T$ is the temperature multiplied by

Boltzmann's constant. Thus, this type of analysis presents the danger of mixing models when it is applied to the bicrystals in large magnetic fields.

In the end, a phenomenological approach was used [82, 83]. On a double-logarithmic scale, H* occurs when the V-I characteristic changes curvature. If the V-I characteristic is then fit to

$$\ln(V) = a + b\ln(I) + c(\ln(I))^2, \qquad (5.1)$$

where a, b, and c are fit parameters, H* occurs when c = 0, which corresponds to a straight line on a double logarithmic scale. This method finds H* as the field where the V-I curve most closely resembles a power-law.

This still leaves the problem of the cross-over to linear behavior at high voltages in the intergrain links. To resolve this, we note that there are two kinds of transport behavior across the grain boundary. At low voltage levels, the transport is characterized by the intragrain-like properties of any strongly coupled paths across the GB, while at higher voltages, flux flows along the boundary, giving rise to an ohmic, linear V-I characteristic. This resistive flux flow type of behavior should be visible even in an intragrain link at sufficiently high electric field levels. At still higher voltages, the intragrain regions on either side of the GB start to become dissipative, causing the V-I characteristic to cross-over from linear to power law. Since we were interested in determining the H* of any strongly coupled paths across the boundary, only data in the lower voltage regions of the V-I curve were fitted.

The fitting of the V-I curves to equation 5.1 was carried out using the *TableCurve* program by Jandel Scientific. Both intragrain and intergrain V-I curves were fit, and the results of plotting the fit parameter c versus field can be seen in Figures 5.19 - 5.21. The field at which the c(H) curve intersects the y-axis zero is H*. In each figure, (a) shows c(H) for the intragrain link, where the entire V-I curve was used to obtain a fit. In (b), the results of fitting the intergrain data are shown, and the maximum voltage included in the fit is indicated by the legend. The error bars are obtained from the standard deviation of c. The results of this analysis are summarized in

Table 5.3, which shows the inter- and intragrain H*.

Table 5.3 Irreversibility Fields

Sample	H^*_{GB} (Tesla)	H^*_{Grain} (Tesla)
Y696s-b(3°)	3.0	3.5
Y743s-b(5°)	3.5	2.6
Y692s-b(7°)	3.5	4.0
Y695s-b(10°)	5.5	3.8
Y700s-b(15°)	0.7	3.8
Y747s-b(20°)	0	--

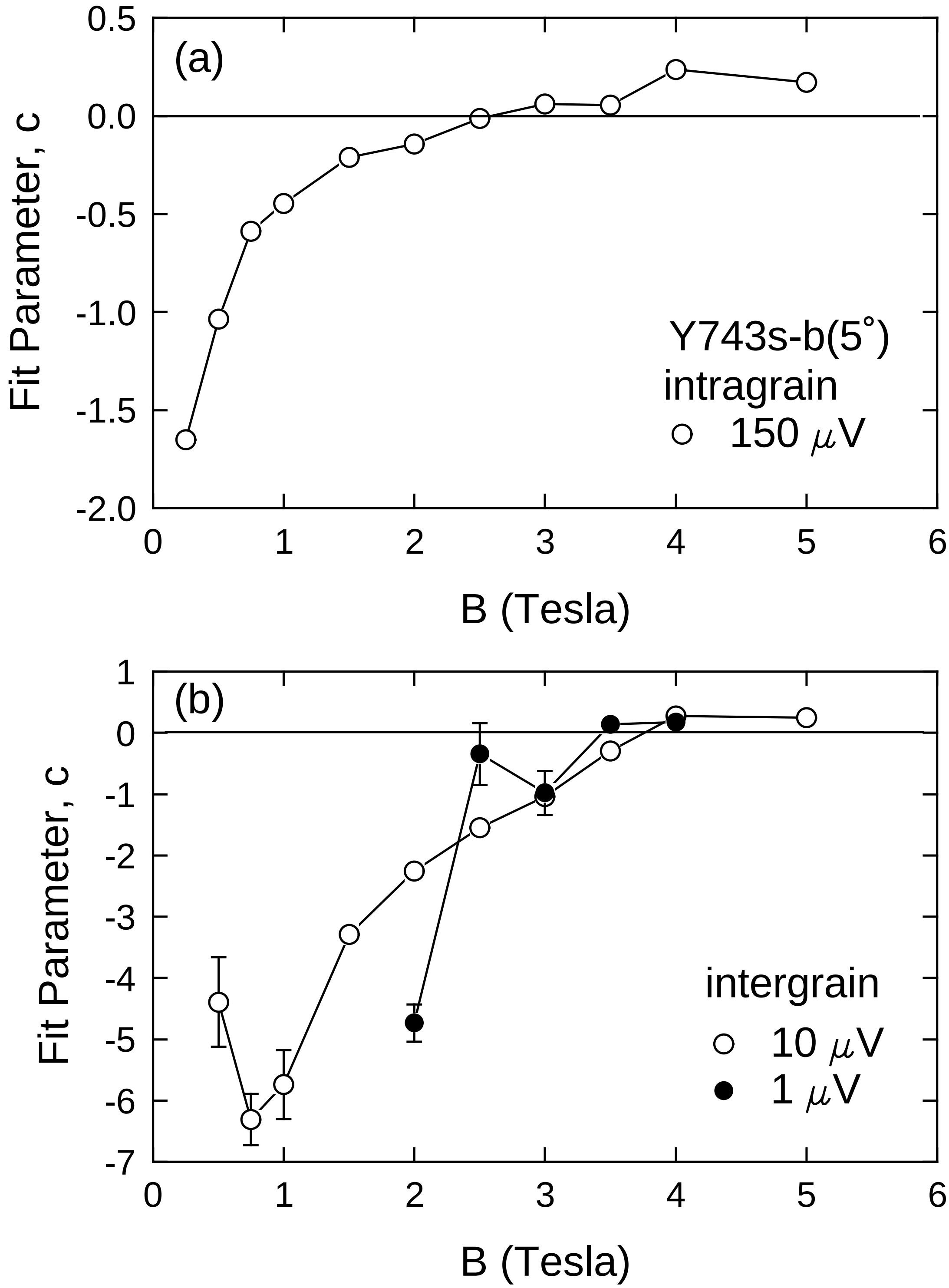

Figure 5.19 Results of fitting the Y743s-b(5°) V-J curves to a quadratic in log-log space.

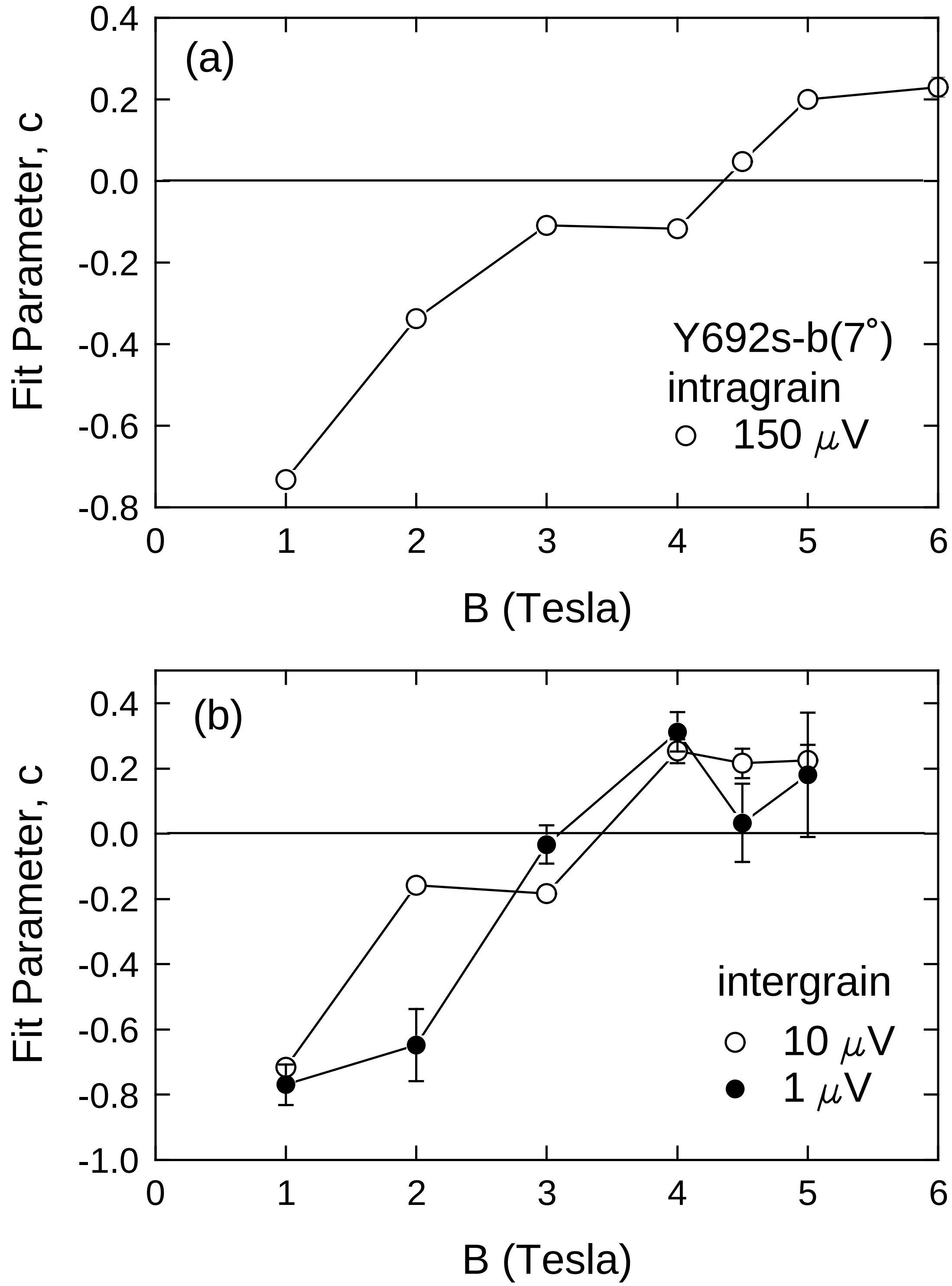

Figure 5.20 Results of fitting the V-J curves of Y692s-b(7°) to a quadratic in log-log space.

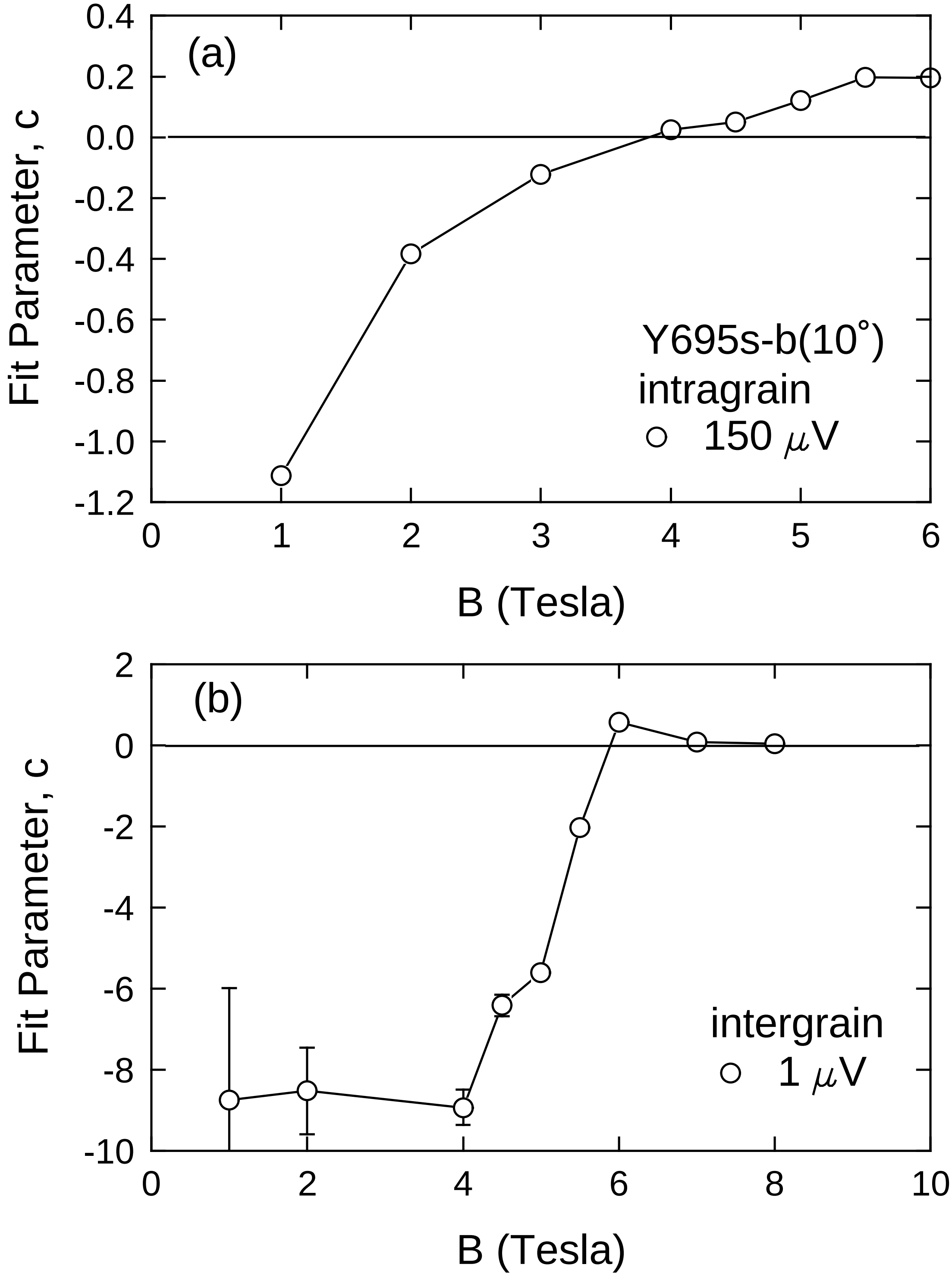

Figure 5.21 Results of fitting the V-J curves of Y695s-b(10°) to a quadratic in log-log space.

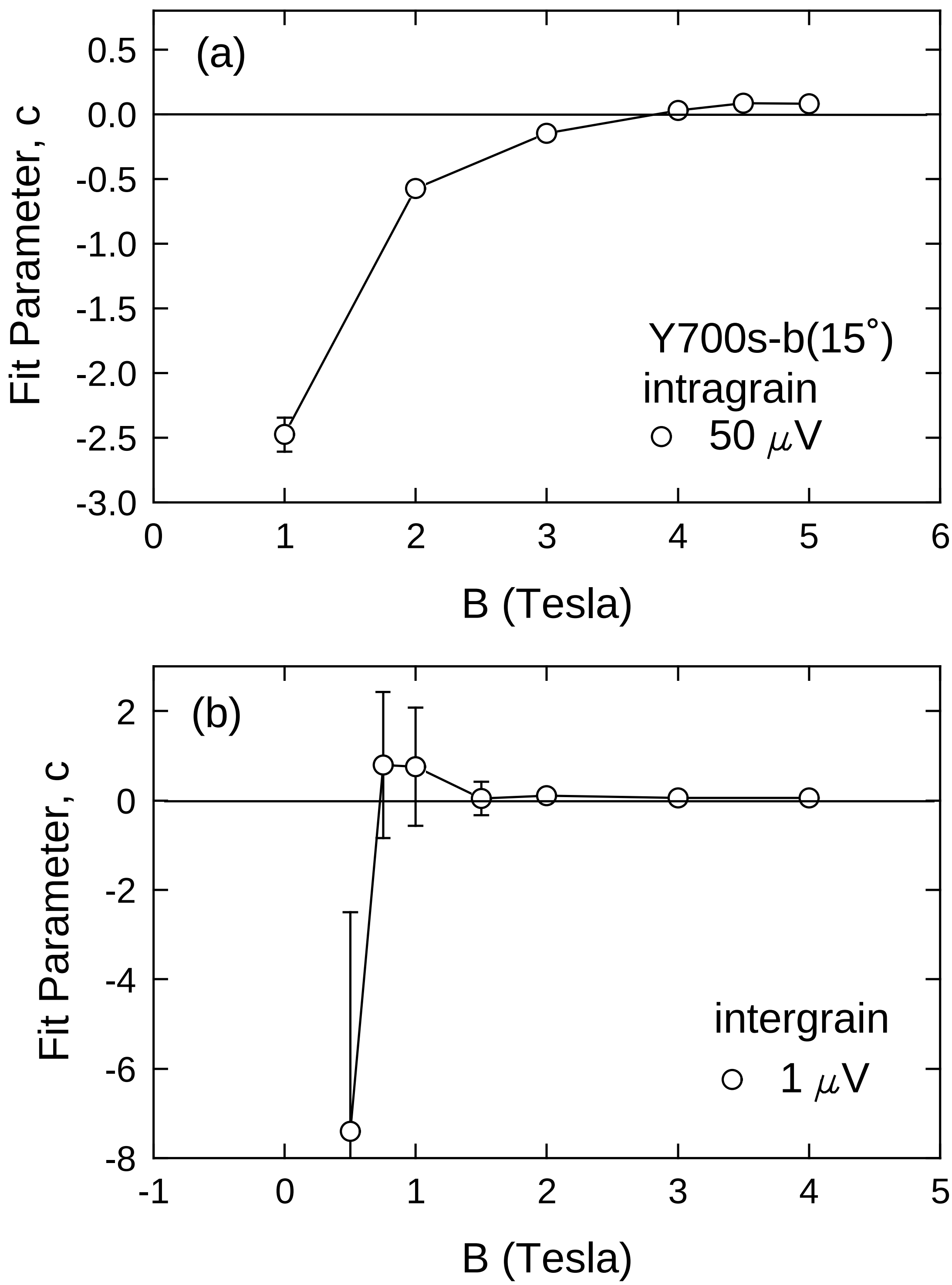

Figure 5.22 The results of fitting the V-J curves of Y700s-b(15°) to a quadratic in log-log space.

The main point of

Table 5.3 is the rapid change in H^*_{GB} between 10° and 15°. Below 10°, the inter- and intragrain irreversibility fields are similar. At 10°, the grain boundary H* is somewhat larger than the intragrain H*, which could be due to additional flux pinning by non-superconducting dislocation cores in the grain boundary. However, at 15°, H^*_{GB} abruptly drops to less than one quarter of the intragrain value, and by 20°, H^*_{GB} is zero. This is consistent with the closure of any strongly coupled channels across the grain boundary between 10° and 15°, since when the good channels close, H^*_{GB} should no longer be similar to H^*_{Grain}. This is compatible with the disappearance of the "plateau" in the $J_c(H)$ curves between 10° and 15° in Figure 5.1.

Temperature Dependence of the E-J curves

In Koch et al.'s [78] study of the epitaxial $YBa_2Cu_3O_{7-x}$ films, they measured the extended V-I curves as a function of temperature at a constant field. The irreversibility temperature, T*, was then found by scaling the V-I curves so that they lay on one of two universal curves. The fact that the curves scale was cited as evidence for a phase transition in the vortex lattice. However, in analogy with H*, the irreversibility temperature, T*, is more simply found by looking for the temperature at which the V-I curve most closely approximates a power-law behavior.

Figures 5.23, 5.24, and 5.25 are the extended V-J curves as a function of temperature for an intragrain, 5°, and 10° link. All measurements were in 1 Tesla applied field, and the V-J curves were taken at approximately 0.5 K intervals. By looking for the change in curvature at lower voltage levels, one can see that the 0°, 5°, and 10° links all show $T^*(1\ T) \approx 84.5$ K. This similarity in the $T^*(1$ Tesla) values, at or below 10°, is consistent with the results of the $H^*(77$ K) analysis above, which were also similar to one another below 10°. As might be expected, the general shape of the V-J curves are similar to the constant temperature curves discussed above.

These measurements are much more time consuming than those made at constant temperature because of the time required to come to thermal equilibrium. Since the meaning of a vortex lattice phase transition along an approximately 2-D defect like a grain boundary is difficult to theoretically formulate, these constant field measurements have little advantage over constant temperature ones in the bicrystal context.

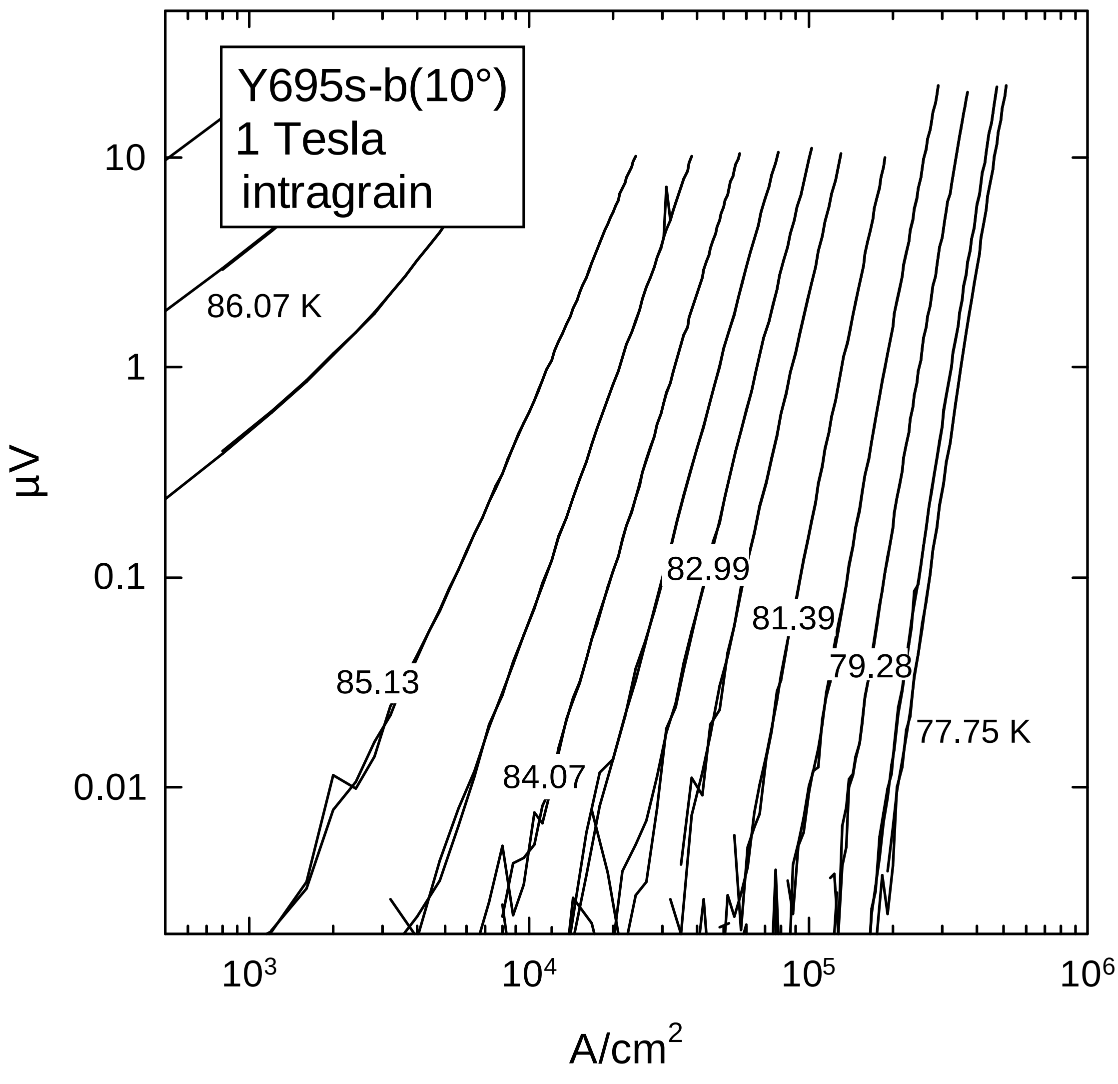

Figure 5.23 V-J curves for the 10 μm intragrain link of Y695s-b(10°) in 1 Tesla applied parallel to the c axes, and the temperature varying from 77.75 K to 86.5 K.

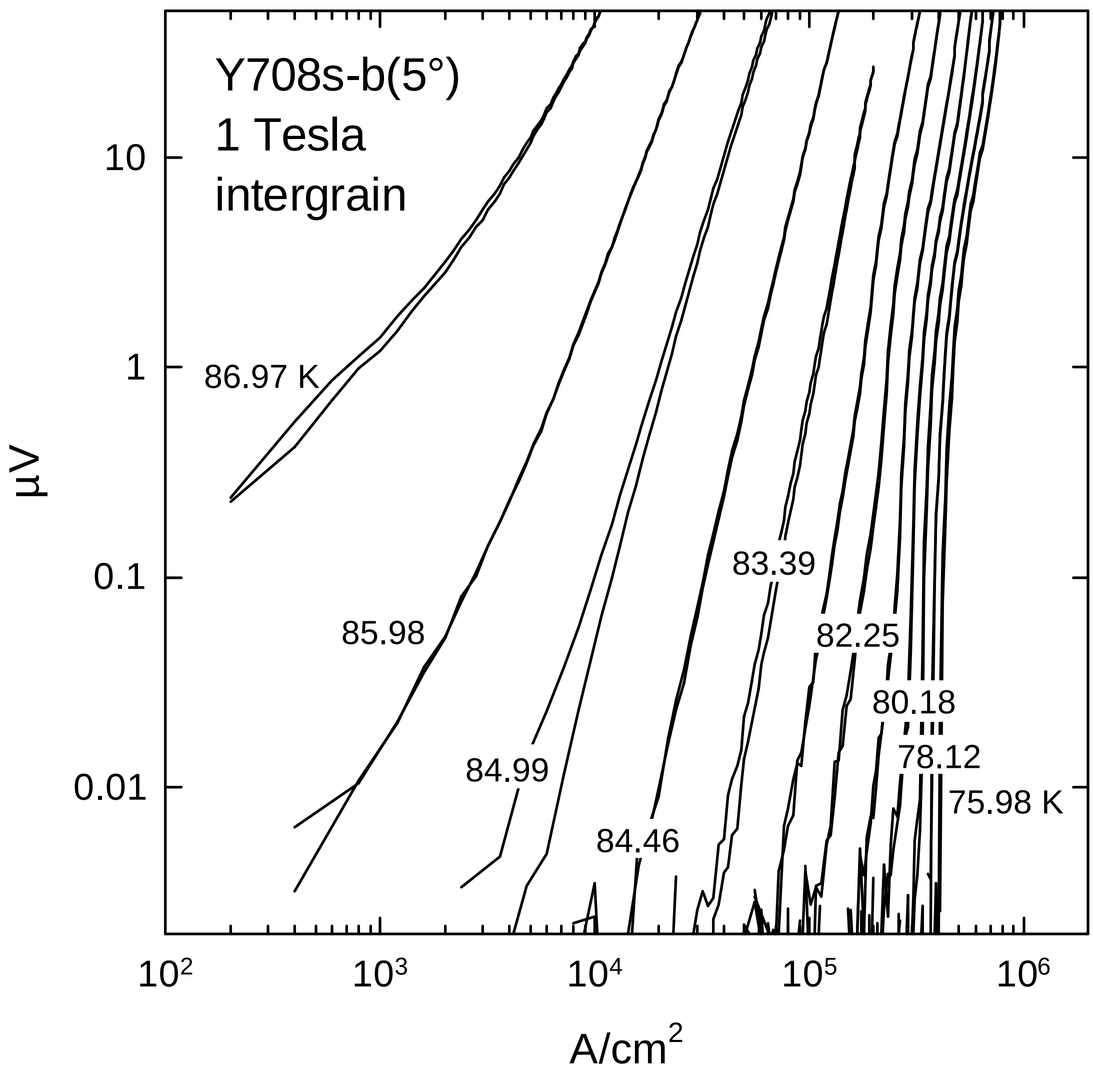

Figure 5.24 V-J curves for a 20 μm intergrain link on Y708s-b(5°) in 1 Tesla, and with the temperature varying from 75.98 K to 86.97 K.

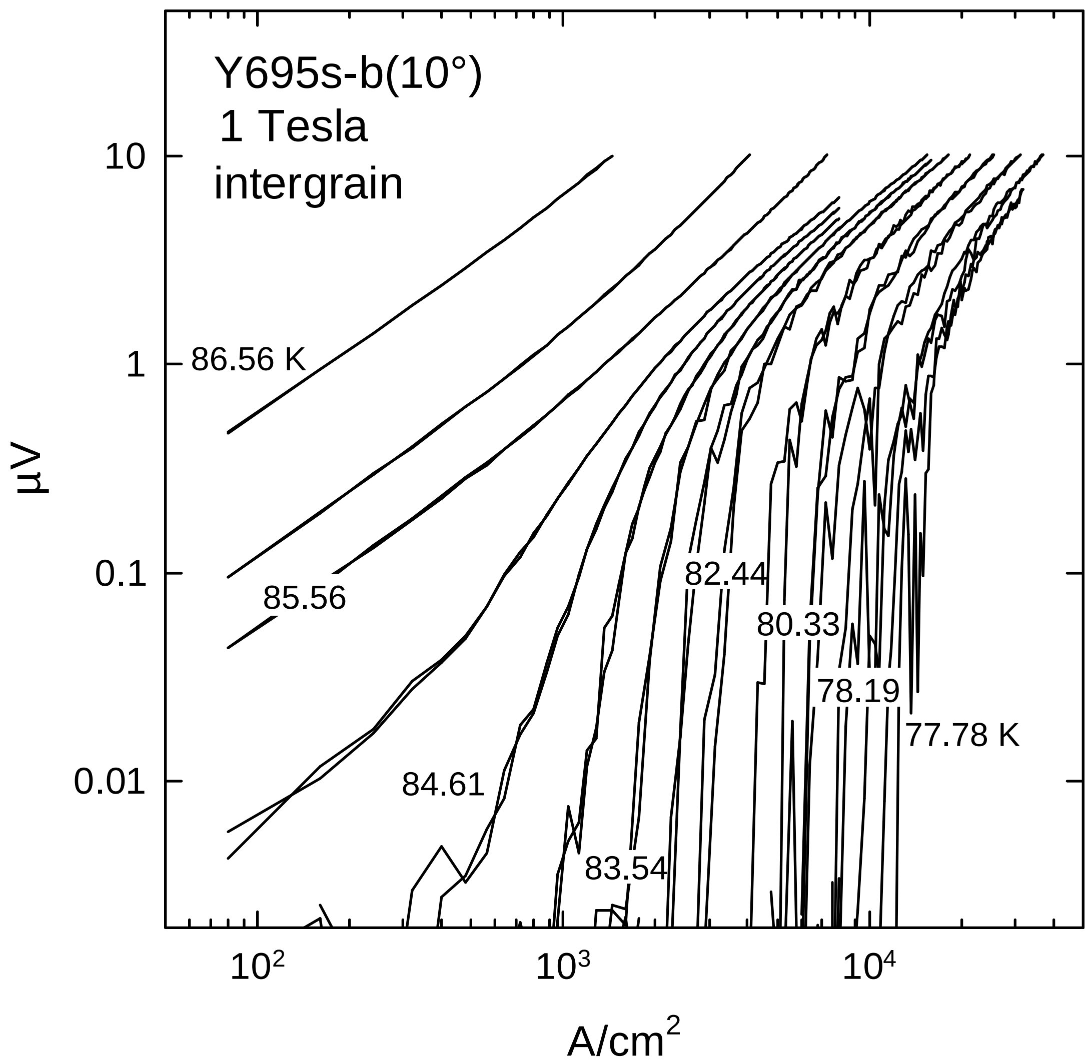

Figure 5.25 V-J curves for a 50 μm intergrain link on Y695s-b(10°), in 1 Tesla applied field, and the temperature varying from 77.78 K to 86.56 K.

Summary

Nanovolt sensitivity V-I characteristics of thin film $YBa_2Cu_3O_{7-x}$ bicrystals with misorientation angles between 3° and 20° were measured in magnetic fields of up to 10 Tesla at 77 K. For each film, the inter- and intragrain J_cs were plotted versus H, showing that the presence of the low angle grain boundary leads to significant changes in the shape of the J_c(H) curve. By studying the pinning force curves, these shape changes were demonstrated to be a result of larger electric fields at the boundary than in the intragrain regions. The peak in the intragrain pinning force curve moved to higher magnetic fields as the voltage criterion increased. The main intergrain pinning force curve also moved to higher magnetic fields as the misorientation angle increased, indicating the electric field at a given voltage level was becoming larger and more localized at the boundary with increasing θ.

The voltage-current density, V-J, curves were also studied to determine the irreversibility field, H*. The logV-logJ curves were fit to a quadratic equation and H* was determined as the point where the quadratic fit parameter went to zero. A rapid decrease in H* between 10° and 15° was seen. This decrease in H* coincides with the absence of a plateau in the J_c(H) curve above 10°. Since a decrease in H* could be reasonably expected upon the closure of any strongly coupled channels in the grain boundary, these results imply that the character of the coupling across the thin film boundaries changes from strongly to weakly coupled at misorientation angles above 10° to 15°.

Chapter 6 : Discussion

Introduction

The purpose of the research in this thesis was to understand the cross-over from strong-to-weak coupling in low angle grain boundaries of $YBa_2Cu_3O_{7-x}$. Both thin film and bulk scale bicrystals were studied, in order to see how intragrain properties and sample geometry influenced the intergrain transport. In this chapter, the results of these experiments are discussed in terms of the dislocation core model. Conclusions and implications for technological applications are also presented.

Low misorientation angle [001] $YBa_2Cu_3O_{7-x}$ bulk scale and thin film bicrystals have been characterized by transport in both low and high magnetic fields, and their properties compared to models of channel transport [1,33]. For both bulk scale and thin film bicrystals, there is qualitative agreement with the underlying “good channels plus barriers” premise of the dislocation core overlap model. However, the increased angular range of the present samples, their larger range of type (both bulk and thin film), the apparently better thin film quality (based on their higher J_c), and their much more detailed transport characterization all combine to show that the present form of the dislocation core overlap model is inadequate to explain the data.

The simple dislocation core overlap model predicts a linear decrease in J_b/J_c with θ, up to a critical angle, θ_c, at which the cores overlap. With the most generous estimates of the relevant parameters, ξ, $|\mathbf{b}|$ and r_m, this model predict the closure of the strong superconducting paths at an angle of 5° - 6°, since strong coupling should not be possible when the channels are smaller than the coherence length, ξ.

In contrast to the earlier IBM data, zero field measurements of J_b/J_c versus θ [001] tilt reveal that up to 7°, the best thin film bicrystals show almost no reduction in intergrain J_b with increasing angle. Above 7°, the data show the non-linear, exponential decrease in $J_b(\theta)$ seen by other thin film groups [12]. The bulk scale bicrystals showed a slower decrease in J_b versus θ than the thin film samples, but their larger scatter makes fitting the data to any particular function somewhat arbitrary. Thus, while all the data in this thesis show a general decline in zero field J_b/J_c with θ, the linear decrease predicted by the simple dislocation core model was not observed.

The second prediction of the dislocation core model was that the strongly coupled channels across the grain boundary would close above a critical misorientation angle, $\theta_c \approx$ 5°-6°. Extended E-J characteristics in fields up to and beyond the irreversibility field, H*, were used to identify strongly coupled components of the grain boundary. Measurements of the thin film bicrystals showed an intergrain H* that was essentially independent of θ up to 10°, and then showed a rapid decrease between 10° and 15°, indicating the closure of strongly coupled channels in this angular region. Bulk scale bicrystals were not studied in such detail. However, data in this thesis show the clear existence of strongly coupled channels in a 14°[001] tilt bulk scale boundary and the recent data of Cai et al. [68] show that the good channels do not close in the bulk bicrystals until substantially greater misorientation angles.

The data presented above clearly support the idea that low angle grain boundaries consist of strongly and weakly coupled segments in parallel, and that the size or number of the good channels decreases as the misorientation angle increases. However, the dislocation core overlap models cannot explain the shape of the J_b/J_c versus θ relationship or the existence of strongly coupled channels at misorientation angles well above 5°. It is thus clear that the dislocation core model as a simple proportional barrier is inadequate. Additional features of the grain boundary nanostructure must be introduced to explain the strong-to-weak transition in low angle YBCO grain boundaries.

Plausible alternative non-superconducting barriers in the boundary include the extended strain fields at nanofacet junctions recently observed in a 6°[001] tilt bulk $YBa_2Cu_3O_{7-x}$ bicrystal [40]. Strain can cause YBCO to lose oxygen, which degrades the hole density and the superconducting properties. These extended strain fields are large and closely spaced enough to provide a row of non-superconducting barriers at the grain boundary. Dislocation strain field analysis by Tsu et al. indicates that these long-range strain fields are caused by the summation of the individual, localized dislocation strain fields within each facet, implying that these long-range, facet-junction, strain fields may also have a θ and dislocation density dependence. Other possible barriers include misorientation angle dependent impurity segregation or contributions from $d_{x^2+y^2}$ order parameter effects, such as those discussed by Hilgenkamp et al. [84]. Possible impurity segregants include Sr and Ti diffusing up from the substrate. These hypotheses need to be verified by further careful electromagnetic and microstructural comparisons between bulk scale bicrystals and thin film bicrystals grown by different techniques. The effect of the anisotropic $d_{x^2+y^2}$ order parameter on the grain boundary transport in the low angle limit is largely unknown, but, as discussed by Hilgenkamp et al. for the higher angle region, order parameter effects can only partially explain the experimentally observed depression of J_b. While impurity segregation and order parameter effects may be contributing factors, collective dislocation strain field effects, like those found at facet-junction nodes are also probable contributors to the details of the low angle, strong-to-weak coupling transition.

Finally, it should be noted that the practical importance of the problem has recently increased with the development of methods of producing textured substrates for YBCO thick film growth. These methods are being considered as a basis for a new superconductor technology. Since such biaxial texturing will never be perfect, understanding the low angle bicrystal sample-to-sample variability in the high field transport properties becomes vital for optimizing the properties of coated $YBa_2Cu_3O_{7-x}$ conductors, like those formed by the IBAD and RABiTS processes.

Models and Microstructure

The basic idea behind the dislocation cores overlap model can be seen in the schematic of three low angle grain boundaries seen in Figure 6.1. The dislocation cores are shown as supercurrent-blocking, cylindrical defects lying along [001] in the GB plane. Using the approximation of a symmetrical tilt boundary and Frank's formula, their spacing as a function of increasing θ is sketched. The core radius is estimated to be the magnitude of the primary grain boundary dislocation, whose Burger's vector is **b** = [100]. This is the Burger's vector seen in the thin film bicrystals (Figure 1.4) In this simple model, non-superconducting dislocation cores act to decrease the strongly coupled superconducting cross section of the grain boundary, thus proportionately decreasing J_b [1,33]. When the channels of "good" superconductor between the cores become smaller than the coherence length, ξ_{ab}, only Dayem-bridge, weakly coupled superconductivity can exist across the GB. One can calculate ξ_{ab}(77 K) from the measured H_{c2} [85], getting a value of ξ_{ab}(77 K) ≈ 3.5 nm. By using the above numbers for ξ and |**b**|, and Frank's formula for the distance between GBDs, the cross-over between strong and weak coupling should occur at a misorientation angle of about 6°, between Figure 6.1(a) and 6.1(b).

In Dimos et al.'s original work, they postulate that the coherence length at the boundary, ξ_{GB}, is much smaller than the bulk value due to strong quasiparticle scattering at the boundary. They then extract a ξ_{GB}(4.2 K) ≈ 0.4 nm, from their measurements of the temperature dependence of the intergrain J_b. In the low angle grain boundary case, this means that along the boundary the coherence length and superconducting gap vary with position between and through the grain boundary dislocations, and this will have an uncertain effect on transport behavior.

Chisholm and Pennycook included the influence of individual dislocation strain fields as factors contributing to the depressed superconductivity at the boundary. These strain fields are oblong-shaped and extend rather far into each side of the grain, greatly increasing the effective width of the boundary. They neglect the influence of the coherence length in their analysis of the grain boundary, and had good supercurrent flowing through the boundary right up until the physical closure of the dislocation core channels, and independent of ξ.

At this point it is useful to compare the behavior of $YBa_2Cu_3O_{7-x}$ to that of Nb_3Sn ($\xi(4.2\ K) \approx 3$ nm) and $SnMo_6S_8$ ($\xi(4.2\ K) \approx 2.5$ nm) [74]. In spite of the fact that the 4.2 K coherence lengths in Nb_3Sn and $SnMo_6S_8$ are smaller than that of $YBa_2Cu_3O_{7-x}$ at 77 K, the grain boundaries in these low temperature superconductors are not weak links. Instead, the grain boundaries, most of which are high angle grain boundaries of arbitrary misorientation, act as the primary pinning centers, and increase the critical current density. This must mean that the grain boundary width is still small compared to the coherence length and superconductivity is not strongly depressed at the boundary. However, the grain boundary does act as a pinning site, indicating some change in the transport properties, and this is most likely a depression of the local mean free path at the boundary. This behavior in Nb_3Sn and $SnMo_6S_8$ makes it clear that the short coherence length is not, in itself, a sufficient reason for weak coupling, and that additional specific features of $YBa_2Cu_3O_{7-x}$, such as the anisotropic order parameter or the effect of strain on the hole concentration, must be incorporated.

In the simple dislocation core overlap model outlined above, the grain boundary dislocation core diameter of ≈ 1 nm is smaller than ξ_{ab}(77 K) of YBCO. This narrow grain boundary width, even when the dislocation cores overlap, should be insufficient to cause weak linked behavior. It thus becomes necessary to either increase the width of the boundary by including the influence of the dislocation strain fields in the model, as was done by Chisholm and Pennycook, or to include the evidence of long range hole density depression [39]. Alternatively, the anisotropy of the order parameter may [illegible] produce misorientation angle effects that are not present in the low temperature superconductors. In any case, adding to the size of the dislocation cores by including their accompanying strai[illegible]ase the θ dependence of J_c, and decrease θ[illegible]. It is not at all clea[illegible]tually happen[illegible]

These simple dislocation core models may well oversimplify the real grain boundary microstructure. Impurity segregation, faceting, and nano-faceting of the boundary are not included in the models. These microstructural differences become impo[illegible]ing the electron[illegible] bicr[illegible] in Chapter 1, [illegible] dislo[illegible] to have Burgers [illegible] **b** = [100] and **b** = [010]. However, dissociation into partial dislocations with **b** = ½[100] cannot be ruled out, producing regions of the GB having stacking faults.

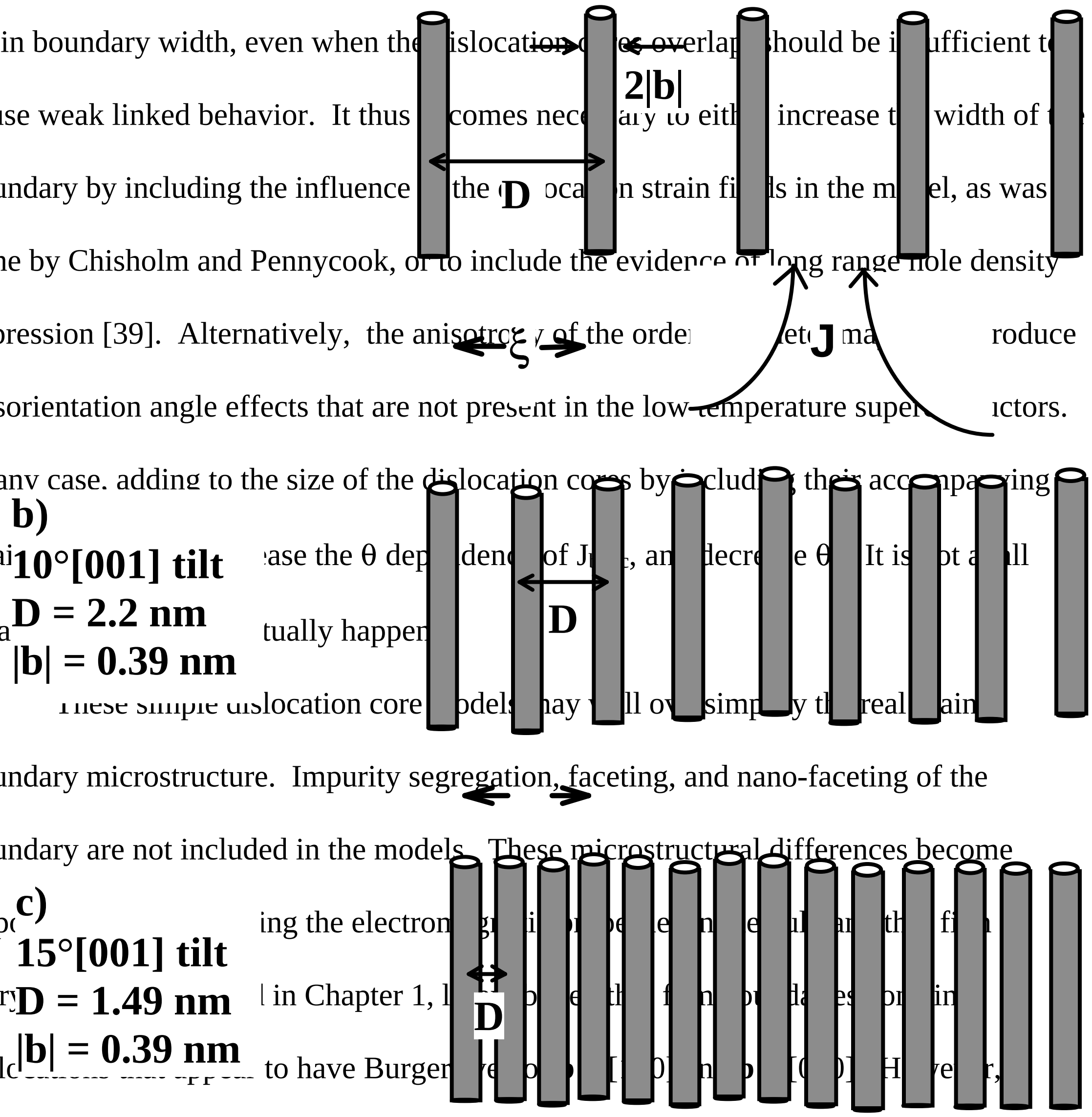

a)
5°[001] tilt
D = 4.5 nm
ξ ≈ 3.5 nm

ξ

Figure 6.1 Sketches of the idealized dislocation structure of a) 5°, b) 10°, and c) 15° [001] tilt grain boundaries. The boundary can be visualized as arrays of dislocation cores, which are seen here as columnar defects, of width ≈ 2|b|, and spacing D = |b|/(2sinθ/2).

Both thin film and bulk grain boundaries show evidence of non-ideal morphology. The boundary plane of the thin films meanders tens of nanometers away from the straight substrate plane, introducing nanoscale faceting that can modify the GBD spacing and introduce variable strain fields along the boundary. Bulk scale bicrystal grain boundaries are not straight either. Their boundaries are macroscopically curved on the scale of hundreds of microns, and also contain facets and nanofacets. As a whole though, their GB structure appears more regular than the corresponding thin film boundaries. These bulk grain boundaries appear to consist primarily of partial dislocations with **b** = ½[110], (and thus each pair of partial dislocations has a stacking fault between them) with a Burgers vector magnitude of |**b**| = 0.27 nm. This is smaller than the thin film Burgers vectors, which have |**b**| = 0.39 nm. This produces a smaller dislocation core and spacing, which should lead to a steeper decrease in J_b/J_c with θ, and a smaller predicted value of θ_c. These expectations are directly contradicted by the data.

As well as the effects of faceting and a complex grain boundary dislocation structure, impurity segregation may also play a role in affecting the grain boundary electromagnetic properties. Interdiffusion between $YBa_2Cu_3O_{7-x}$ and $SrTiO_3$ is well known, and it may be that the thin film YBCO GBD cores may act as an easy diffusion path for Sr and Ti from the substrate. This is a mechanism for increasing the effective size of the dislocation cores and reducing the size of the good channels. Impurity segregation effects should be important when comparing the pulsed laser deposition (PLD) thin film bicrystals in this thesis, and the electron beam evaporated (EBE) bicrystals, from [1]. Although EBE films are made at lower temperatures (≈ 550°C) than the PLD films (≈ 800°C), the EBE films must be post-annealed at a higher temperature (≈

925°C) to produce the $YBa_2Cu_3O_{7-x}$ structure, introducing opportunities for greater substrate/film interdiffusion.

Dislocation core overlap models provide a simple visualization of the transition between strong and weak coupling seen in low angle bicrystals of YBCO. The enlargement of the non-superconducting dislocation cores by adding their accompanying strain fields, as done by [33], is necessary to increase the width of the non-superconducting GB barriers so that they act as weak links instead of as pinning centers. These dislocation core models predict a steep decrease in J_b/J_c versus θ, and a closure of any strongly coupled channels across the GB at a critical angle, $\theta_c \approx 6°$. The effects of complex GB morphology and dislocation network structure, as well as GB impurity segregation, may play important roles in modifying the basic dislocation core overlap model.

The Grain Boundary Cross Sectional Area

A large number of thin film and bulk samples were measured in zero and low magnetic fields. These data were used to test the prediction of the dislocation core model that there should be a linear decrease in J_b/J_c with θ in the low misorientation angle region. This linear decrease should follow the expression,

$$J_b/J_c = 1 - (2r_m/|\mathbf{b}|)\, \theta,$$

derived from the proportional decrease of the cross-sectional area of good superconductor in the grain boundary as θ increases. Figure 6.2 presents data from the PLD thin film bicrystal data (also seen in Figure 3.8) and compares them to the original EBE [001] tilt bicrystal data from Dimos et al.[1]. The reduced scatter and increased number of data points of the present work reveal that the PLD bicrystals do not show a linear decrease in J_b/J_c with θ. Rather, the ratio of J_b/J_c is almost unity between 0° and 7°. Careful inspection of Figure 6.2 shows that J_b/J_c can be as high as 0.95 for θ = 7°. As first observed by Ivanov et al. [9], the intergranular critical current density shows an exponential decrease with θ at higher angles, as is shown clearly in the semi-logarithmic inset plot. One can conclude that there are two distinct regimes of behavior, one at low angles where there in no depression of J_b under the best circumstances, and one at higher angles, where the weak link properties dominate the grain boundary behavior and produce a J_c which is exponential in θ.

Comparison of the two data sets in Figure 6.2 show that they are qualitatively similar. For a given θ, J_b/J_c is somewhat larger for the PLD films than for the EBE films, but both data sets lie within the scatter of each other. It is also possible to compare the thin films with the bulk scale bicrystals. In the bulk scale bicrystal data a comparable, somewhat slower, decrease in J_b with θ was seen (Figure 3.4). So while all three sample sets: the PLD films, the EBE films, and the bulk scale bicrystals, show a similar general decrease in J_b with θ, the actual rate of decrease is not the same. A most noticeable feature is that the J_b values of the bulk bicrystals decrease more slowly than either thin film set, although the |**b**| values most commonly seen were smaller in the bulk than in the films, which should lead to a steeper decline of J_b with θ.

Differences between the sample sets become more obvious when the low magnetic field dependence of the bicrystals are compared. In studies of the EBE bicrystal films by Mannhart et al. [1], the half width of the main peak in $J_b(H)$ of a 5°[001] tilt bicrystal (10 μm wide link) was only about 0.7 mT. Our PLD bicrystals appear to have a gradually increasing field sensitivity as θ increases. The strong low field sensitivity seen in the 5° EBE bicrystal was not seen in the PLD bicrystals until the misorientation angle had reached 10° (see Figure 3.7 and accompanying text), indicating that this low magnetic field sensitivity is processing dependent.

In the bulk bicrystals, no low magnetic field sensitivity of J_b was seen when θ was less than 10°. Between 10° and 16°, individual samples either displayed no magnetic field sensitivity of J_b, or significant low field dependence. Direct comparisons of the relative low field sensitivity between bulk and thin film bicrystals are difficult because of the large difference in grain boundary area between the two types of samples. Nevertheless, these results suggest that the bulk bicrystals are less affected by impurity segregation than either the EBE or PLD bicrystal films.

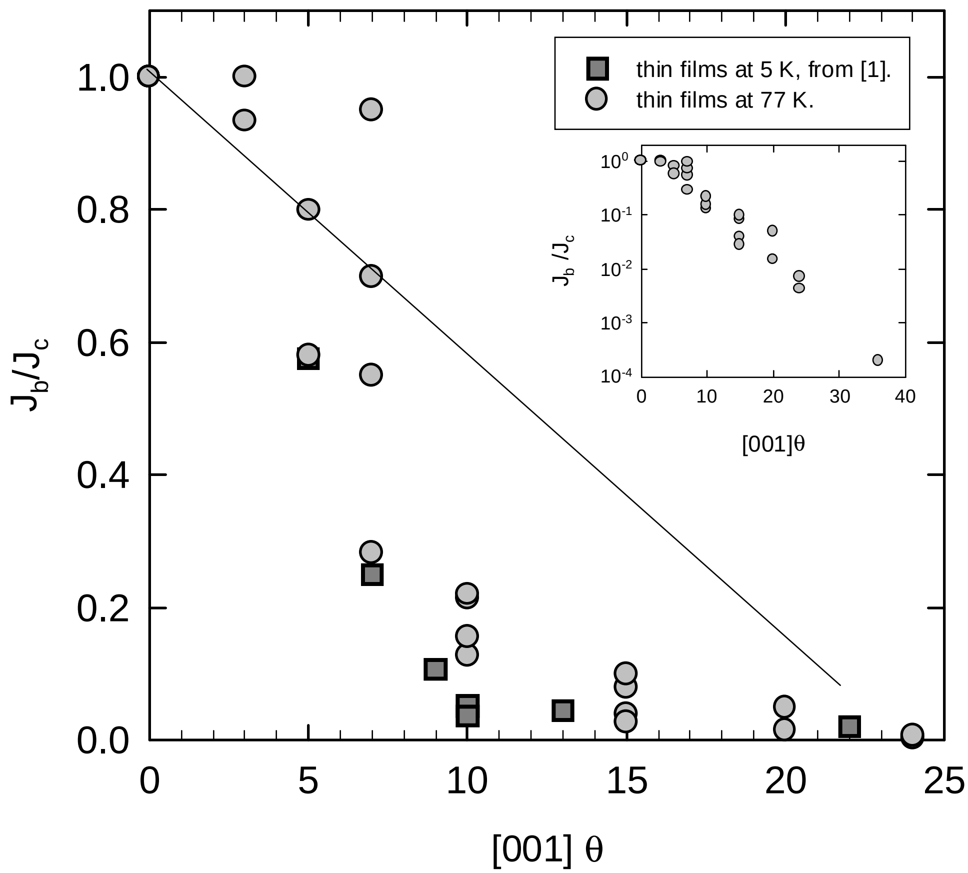

Figure 6.2 Normalized J_b/J_c(0T) versus [001]θ using electron beam deposited thin film data from Dimos et al. [1], at 5 K, and pulsed laser ablated thin films from this work, at 77 K. The inset shows the exponential behavior of the laser ablated films.

Zero field measurements of J_b/J_c versus θ in the PLD films show that in the best samples, there is no appreciable decrease in J_b/J_c up to 7°, and then J_b/J_c decreases exponentially with misorientation angle. Comparisons of the EBE, PLD, and bulk scale bicrystals all show a general decrease in J_b/J_c with increasing θ, but the bulk scale bicrystals show a slower fall off in J_b/J_c, contradicting the expectation that the relatively small Burgers vector magnitude in the bulk would lead to a more rapid decrease in J_b/J_c.

Low magnetic field transport measurements show further differences between the sample sets, indicating that impurity segregation effects may be significant. All these features are unaccounted for within the simple dislocation core overlap model.

Strongly Coupled Channels

The second significant prediction of the dislocation core model is that a well-defined transition angle, θ_c should exist, and that the closure of any strongly coupled channels across the grain boundary should occur at $\theta_c \approx 6°$. Before the work in this thesis, this prediction had not been specifically tested in the low-to-high misorientation angle regime. To explicitly determine θ_c, we needed to establish a criterion for open channels. This was the existence of *intergrain* V-J characteristics that exhibited qualitatively similar properties to the *intragrain* characteristics. More specifically, by analyzing the high magnetic field V-J characteristics to determine the irreversibility field, H*, of both grains and grain boundary, the misorientation angle at which H^*_{GB} became much less than H^*_{Grain} corresponds to the closure of any open channels, and the transition angle, θ_c.

In the thin film bicrystals, both inter and intragranular irreversibility fields, H*(77 K) were extracted by finding the change in curvature of the double logarithmic V-I characteristics as a function of field. For misorientation angles at or below 10°, the inter and intragranular H*(77 K) values were very similar. Between 10° and 15°, the H^*_{GB}(77 K) becomes much less than that of the intragranular region, and by 20° no downward curvature of the double-logarithmic V-I characteristic was seen, even at zero field. Since H* is measured from the low voltage regions of the V-I curve that are dominated by transport through the strongly coupled GB segments, the disappearance of an H* characteristic indicates that strongly coupled channels no longer exist across these grain boundaries. This analysis indicates $10° < \theta_c \leq 15°$ for the PLD films.

The bulk bicrystals were also measured in high fields. However, the bulk bicrystal data are less extensive than those taken on the thin film bicrystals because of the difficulties in putting leads on these small samples, and because the V-I curves were measured before the nanovoltmeter was set up. Despite this, an lower estimate for θ_c is possible by observing the change in shape of $J_b(H)$ with increasing θ. Low angle, strongly coupled bulk bicrystals had a roughly linear decrease in $J_b(H)$, while the apparently weakly coupled bulk bicrystals had an initially rapid decrease in $J_b(H)$ before it became approximately constant in higher fields. This cross-over from primarily strong to primarily weak coupling occurred at misorientation angles between 10° and 15°. Later nanovolt level H^*_{GB} measurements by X.Y. Cai [68] suggest that strongly coupled channels exist even in 15°, 18°, and 27°[001] tilt bulk bicrystals, which is a significantly higher angle for θ_c than what was observed in the thin films bicrystals.

For both the bulk scale and the thin film bicrystals, these high field measurements of θ_c are much larger than what is expected within the dislocation core models.

Electric Field Effects

A further striking result from the PLD thin films is that there is a gradual shape evolution of the high magnetic field $J_b(H)$ as θ increases. One qualitative reason for this has already been suggested. There are significant proximity coupled components of the grain boundary, and these are quickly suppressed in fields below 1 Tesla, leaving only the strongly coupled grain boundary segments to contribute to the J_b in higher magnetic fields.

Because $J_b(H)$ is measured at a constant voltage criterion, this picture is complicated by the effect of the local electric field at the grain boundary. In a polycrystalline material, one assumes that the electric field is constant between the voltage leads, making it possible to calculate the electric field as the voltage divided by the distance between the voltage leads. Across a grain boundary, the electric field is clearly not constant. If the grain boundary critical current, I_b, is less than the grain current, I_c, most of the voltage dissipation will be generated at the boundary. The smaller I_b is relative to I_c, the more the voltage drop and the electric field becomes localized at the boundary. This has some interesting consequences.

In higher magnetic fields, the suppression of the weaker proximity coupled components of the grain boundary leads to a rapid decrease in J_b in magnetic fields below 1 Tesla. This decrease in $J_b(0.01\ \mu V)$ becomes more pronounced with increasing θ , suggesting it is due to some aspect of the grain boundary structure. The narrowing of the "good" channels with increasing θ, and the increased normal state resistance (Figure

3.10) of the grain boundary both act to increase the electric field at the grain boundary. Thus, to properly interpret the change of shape of the $J_b(H)$ characteristic with increasing θ requires a full analysis of the effect of the local electric field on the magnitude of J_b.

In our transport experiments, just as those of Dimos et al. and Ivanov et al, the *inter*granular properties are measured in series with the *intra*granular. Dissipation will be first produced by whichever is weaker, and at higher applied currents, the voltage dissipation will have contributions from both the inter- and intragrain sections. There are two possible approaches to understanding the effect of the local electric field. One method is by quantitative analysis of the magneto-optic data (see Appendix A), where analysis of the magnetic fields induced by the Meissner screening currents make it possible to derive J_b/J_c, where both J_b and J_c are at the same electric field values. The other way to extract information is by analyzing the electric field dependence of the intragranular $F_p(H)$ characteristic (seen in Figure 5.5). The effect of taking this data at 0.2 mV/cm instead of 2 μV/cm is to raise the field at which $F_p(max)$ occurs by almost a factor of two (from 0.86 T to 1.38 T). Thus, since the "plateau" in the intergranular $J_c(H)$ curves correspond to an $F_p(max)$ at higher magnetic fields (see Figure 5.6), one factor in the development of the "plateau" is the increased localization of the electric field at the grain boundary. This makes it possible to make an estimate of the enhanced electric field at the boundary.

This "plateau" in $J_b(H)$ was seen in 5°, 7°, and 10° [001] tilt thin film bicrystals. It was not observed in the 3° or 15° bicrystals, and one of the 7° bicrystals also showed no evidence of a "plateau". In the 3° bicrystal, it appears the grain boundary did not have any weakly coupled components, and there was thus no excess electric field at that grain boundary. In the 15° bicrystal, the grain boundary appeared not to have any strongly coupled components, and so no "plateau" feature was observed.

In Figure 5.2(a) and Figure 5.11, the data from the 7° thin film bicrystal (Y692s-b(7°)) shows no apparent excess electric field at the boundary. This particular film had a relatively low intragrain J_c (J_c(77 K, 0T) = 1.2 MA/cm^2, from Table 3.2), and it may be that the non-superconducting parts of the GB acted as pinning centers, increasing the grain boundary J_b so that it was higher than the intragrain J_c. This variation in the high field intergrain properties between bicrystals with the same misorientation angle indicate the need for more in-depth studies on how growth and processing affects grain boundary transport and microstructure.

Conclusions

Extensive characterization of both PLD and bulk scale [001] tilt bicrystals in the low angle to high angle misorientation range were carried out in this thesis. These measurements were made to test the validity of dislocation core overlap models. The specific predictions of this model are that there should be a linear decrease in J_b/J_c with θ that depends on the GBD Burgers vector, and that a critical misorientation angle of $\theta_c \approx$ 6° existed, above which strongly coupled channels across the boundary no longer existed. These model features were not observed in the data.

Zero field measurements of J_b/J_c versus θ reveal that there are two different regimes of behavior in the PLD bicrystal films. From 0° to 7°, $J_b/J_c \approx 1$, with essentially no misorientation angle dependence. Above 7°, J_b/J_c shows an exponential dependence on θ. The bulk scale bicrystal data had substantial scatter, but a generally slower decrease of J_b with θ than in the films was seen. Both sets of data show surprising features in the context of the dislocation core models. The thin films do not show the linear decrease of J_b/J_c with θ predicted by the model, and the bulk bicrystals show a more gradual decrease in J_b/J_c with θ than the films. This more gradual decrease is unexpected, because microstructural analysis of both film and bulk grain boundaries indicates that the bulk GBDs are more closely spaced than the film GBDs.

High magnetic field measurements of H*(77 K) were made to determine the closure of the strongly coupled channels across the grain boundary. In the PLD thin films, $10° < \theta_c \leq 15°$. In the bulk bicrystals, θ_c is at least 15°, and may be as high at 27°. These much higher than expected values of θ_c imply that strongly coupled supercurrent is flowing through channels between the dislocation cores that are much narrower than the coherence length.

Variations in the behavior of samples with the same misorientation angle illustrate the importance of microstructure and growth issues to optimizing the high field properties of these materials. Study of the extended voltage-current curves of several 7° thin film bicrystals indicate that one of these shows no evidence of weak coupling or elevated grain boundary electric fields in high fields. This variability between samples with the same misorientation angle and macroscopic grain boundary plane indicate that materials science issues like GB impurity segregation and GB facet structure can significantly change the electromagnetic transport properties. In order to fully understand these issues, further correlation of microstructure and transport properties in these materials is necessary.

Appendix A: Magneto-optic Imaging

Identifying large scale inhomogeneities in the electromagnetic properties of a superconductor is an important step in optimizing these materials. In the bicrystal experiments, being able to distinguish intra- and intergranular contributions to the current transport requires homogeneous intragranular properties. In our thin film $YBa_2Cu_3O_{7-x}$, a homogeneous sample on length scales smaller than the patterned links was an important goal during growth optimization. The homogeneity of the films was checked by comparing a number of patterned links on a single sample, but this is quite labor intensive. In bulk scale $YBa_2Cu_3O_{7-x}$ bicrystals, understanding how the current path is affected by twin boundaries, local variations in oxygen content, and local defects is a prerequisite to interpreting the intergranular transport data. Magneto-optic imaging (MO) uses the Faraday effect [86,87,88] to quickly and non-destructively yield information on the local magnetic field above a sample.

Magneto-optic imaging consists of placing a field sensitive detector film on top of the sample to be imaged, and observing the changes in the detector film in a polarized light microscope. The iron garnet detector film consists of in-plane polarization domains that are sensitive to the local magnetic field, and appear to change color under polarized light as the magnetization changes. Typically, the detector film also has a layer of Al between the sample and the iron garnet to improve the contrast. For studying superconductors, the samples are placed in a small evacuated cryostat with a quartz window that fits under a polarized light microscope, and the temperature is controlled by flowing cold He gas through the copper sample mount. This technique, using an iron garnet detector film, has a resolution of several microns.

An MO study on the effect of grain boundaries on the Meissner screening ability of bulk scale $YBa_2Cu_3O_{7-x}$ polycrystals was carried out by M. Turchinskaya et al. [89]. They found, in increasing magnetic field, that flux first penetrated high angle grain boundaries with $\theta \geq 10°$, then along low angle grain boundaries, and then along the twin boundaries. Very low angle grain boundaries, $\theta \leq 4°$, would trap flux when the applied magnetic field was reduced to zero, indicating that pinning exists along these boundaries.

Within our Applied Superconductivity Center, Dr. Anatolyii Polyanskii and Alexander Pashitskii have developed a magneto-optic imaging apparatus, and used it to look at the low angle $YBa_2Cu_3O_{7-x}$ thin film bicrystals [73]. Bicrystals with [001] misorientation angles of 3°, 5°, 7°, and 10° were studied in magnetic fields of up to 80 mT. The resulting images fit the Bean model, and show a 'cusp' at 5° and 7°, where the intergrain J_b is some large percentage of the intragrain J_c. Because transport measurements across adjacent grain boundary links in similar films have very comparable J_bs, we know this 'cusp' is not due to a strongly coupled region across the center of the grain boundary. Later computer modeling of low grain boundaries within the Bean model produced a 'cusp'-like feature as an artifact of the large percentage of total intragrain current crossing the grain boundary.

It is also possible to extract relative values of J_b from the experimentally determined local magnetic field. These derived values of J_b are in very good agreement with those determined by transport. Another key result is that the magneto-optic images clearly show that the $YBa_2Cu_3O_{7-x}$ films are of a uniform quality throughout. During film growth, uniform, consistent heating of the sample substrates was a constant concern, and one that was difficult to check. The symmetric Bean model patterns observed by MO

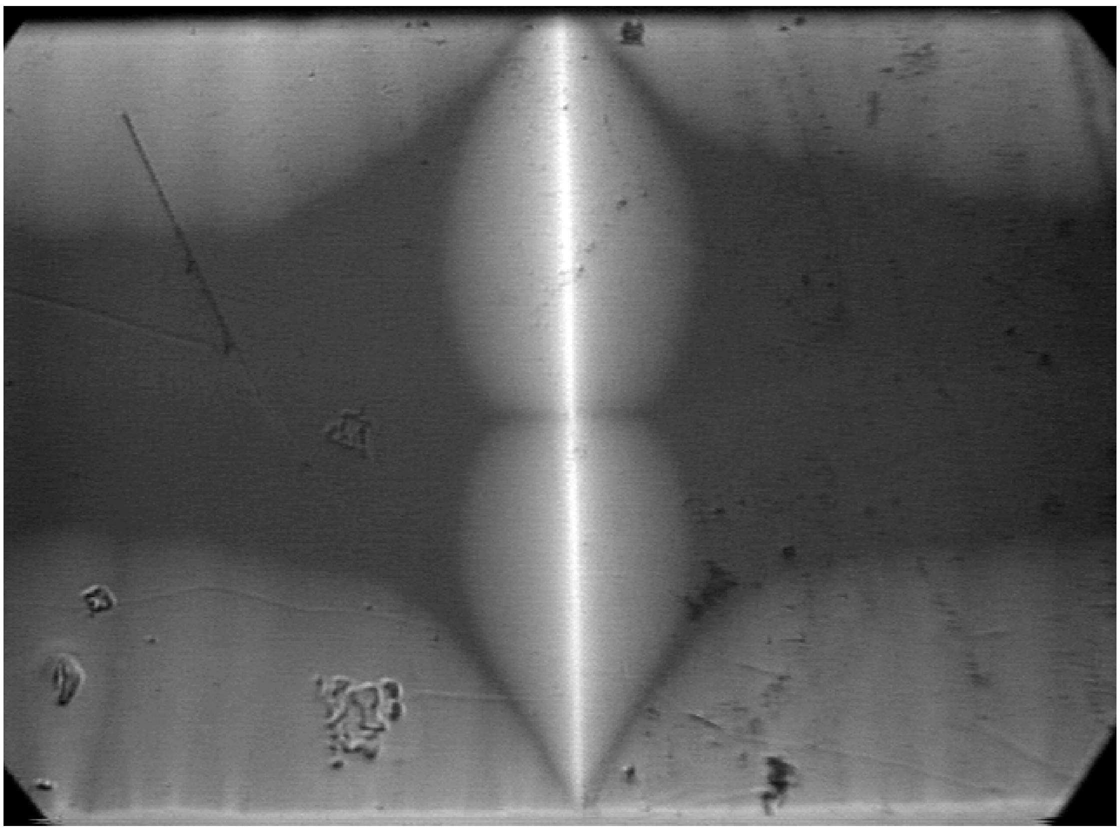

Figure A.1 A 5° thin film bicrystal MO image in 40 mT applied field. The lighter regions indicate areas where the magnetic flux has penetrated, so the grain boundary is the bright vertical line in the center. Note the "cusp" in the middle of the grain boundary.

show that the small variations in deposition temperature across the sample had little effect on the final film quality.

Magneto-optic imaging is a useful, non-destructive technique. It can be done quickly and simply, obtaining information on the spatial variation of the electromagnetic properties that would be impossible, or extremely tedious, to otherwise acquire. Thin film $YBa_2Cu_3O_{7-x}$ bicrystals were studied by MO imaging, confirming that the films were homogeneous and that even a 5° grain boundary limits the critical current density. In conjunction with transport measurements, MO imaging can provide valuable information on the electromagnetic heterogeneity in a superconductor.

Appendix B: $Bi_2Sr_2CaCu_2O_x$ Thin Film Bicrystals

Introduction

While this thesis work focused on the low- to high-angle transition in $YBa_2Cu_3O_{7-x}$, the weak-link problem in other high temperature superconductors is also of great interest. In particular, because of their use in tape and wire conductors, much research has been done to study the coupling in the bismuth based compounds, in particular $Bi_2Sr_2CaCu_2O_x$. Within our Materials Research Group, Jyh Lih Wang has studied the coupling across artificial and naturally occurring bulk scale bicrystals of $Bi_2Sr_2CaCu_2O_x$ [90], illustrating some of the differences between the $YBa_2Cu_3O_{7-x}$ and $Bi_2Sr_2CaCu_2O_x$ systems. Looking at the properties of low angle thin film grain boundaries in $Bi_2Sr_2CaCu_2O_x$ and comparing it to what is known about YBCO would be very interesting.

For this reason, some low angle thin film bicrystals of $Bi_2Sr_2CaCu_2O_x$ on $SrTiO_3$ were studied. Dr. James Eckstein of Varian Associates, Inc. grew the $Bi_2Sr_2CaCu_2O_x$ films by MBE (Molecular beam epitaxy) onto a 10° and a 15° $SrTiO_3$ bicrystal substrate. They were then sent to Wisconsin, where gold for the contact pads was sputtered onto the films, using a shadow mask. Before any patterning was carried out the bicrystals were studied by magneto-optic imaging,. After patterning, R-T and V-I curves were measured in zero field. Some high magnetic field V-I curves were also measured at 26 K. Unfortunately, $Bi_2Sr_2CaCu_2O_x$ thin films appear much more susceptible to environmental degradation and variations in the oxygen content than $YBa_2Cu_3O_{7-x}$, leading to less consistent results. Nevertheless, some low field data on the 10° $Bi_2Sr_2CaCu_2O_x$ bicrystal is quite intriguing.

Growth and Processing

Growing epitaxial, single phase $Bi_2Sr_2Ca_2Cu_3O_x$ films is very difficult, requiring fine control of the amounts of the precursor substances during growth. Dr. Eckstein's system has an in-situ RHEED which measures the film composition during growth. To get a good signal from the RHEED, the back side of the bicrystal substrates was coated with Ti/Pt/Au. The samples are grown at 740°C, and oxygenated by placing them in an ozone beam at 625°C and again at 500°C. The films are then rapidly cooled to room temperature. The 10° and 15° bicrystal films were grown side by side, with an absolute stoichometric variation across the samples of 2% to 3%. Over part of 10° bicrystal, including the grain boundary, occasional CaO precipitates were observed by light microscopy. No CaO precipitates were seen in the 15° bicrystal film.

After we received the films, gold for contacts was sputtered onto them, while the grain boundary region was protected by a stainless steel shadow mask. The sputtering chamber was pumped down to 10^{-6} Torr, and to remove surface moisture from the films, the system was kept at high vacuum for two hours. The samples were then cooled to -

25°C, by flowing liquid nitrogen through the copper sample-mounting plate. Unlike the $YBa_2Cu_3O_{7-x}$ films, the film surface was *not* cleaned by ion beam evaporation (IBE) before the gold was sputtered, as Dr. Eckstein felt IBE was detrimental to the films. The bicrystals were warmed to room temperature and then MO imaged by Dr. Polyanskii and Alexander Pashitskii.

The bicrystals were then photolithographically patterned and dry etched, similar to what was done to the YBCO thin films. The gold contacts did not adhere uniformly to the $Bi_2Sr_2CaCu_2O_x$ surface, leading to some contact resistances two or three times higher than typical for the YBCO bicrystals, and in some areas the gold peeled off the $Bi_2Sr_2CaCu_2O_x$ entirely.

Magneto-Optic Imaging

The $Bi_2Sr_2CaCu_2O_x$ bicrystals were studied by magneto-optic imaging, and the results can be seen in Figures B.1 and B.2. There are a number of unusual features. Figure B.1 shows an image of the 10° bicrystal, and has reasonably good contrast. The brighter, higher contrast regions are the parts of the film that are covered by a layer of gold. The higher contrast and presence of Bean model type patterns indicates the Meissner screening ability of the superconductor lying under the gold was much better than the parts of the film that were left exposed.

The grain boundary is also evident in Figure B.1 as a vertical line of dark contrast in the center of the image. More surprising was the dark line of escaped flux just visible in the upper left hand corner of Figure B.1. This straight line extended almost entirely across the bicrystal, and was not visible with light microscopy. This line of easy flux motion is perhaps indicative of a stacking fault or twin boundary in the BSCCO. A final point is that the regular 'roof-top' shape of the Bean flux profile seen in the $YBa_2Cu_3O_{7-x}$ thin film bicrystals is much more irregular in these $Bi_2Sr_2CaCu_2O_x$ bicrystal films.

In Figure B.2, the magneto-optic imaging results for the 15° bicrystal can be seen. The beneficial effects of a gold layer are again obvious, as is the preferential flux penetration along the grain boundary. The contrast of the underlying bare $Bi_2Sr_2CaCu_2O_x$ film is quite poor, indicating a poorer ability to shield flux than the 10° bicrystal. However, or perhaps because of this, the Bean flux profiles in the gold coated regions are much more regular than those seen in Figure B.1.

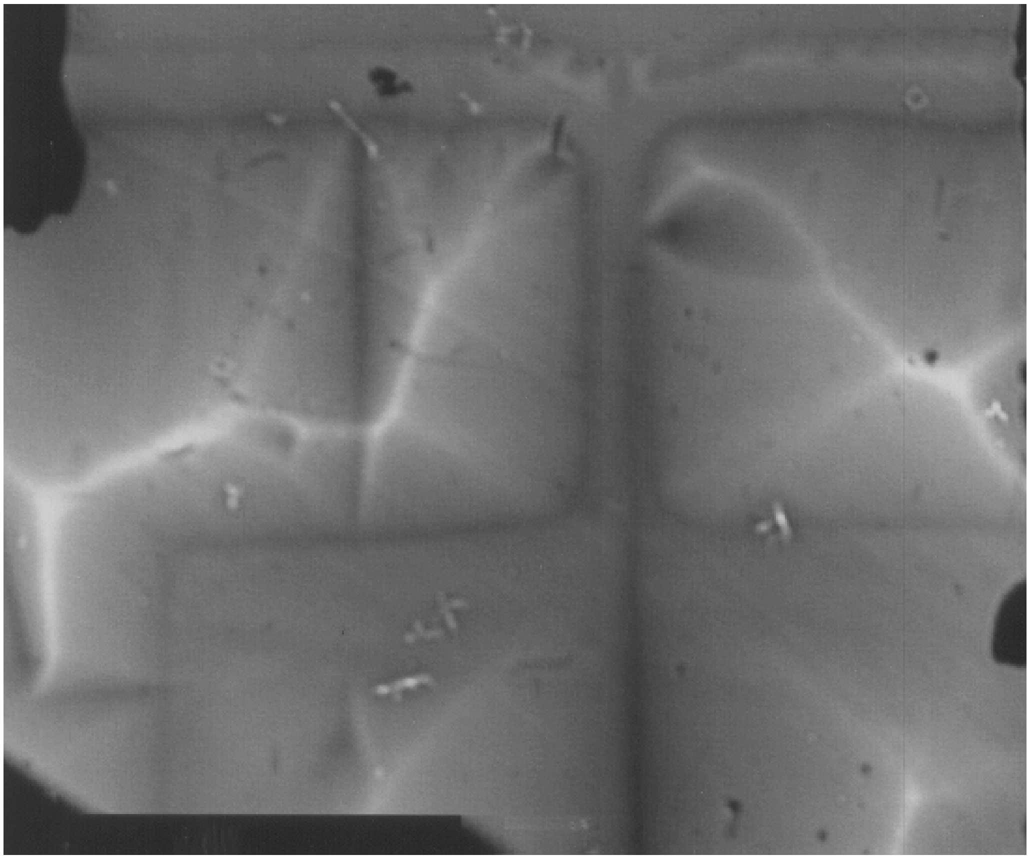

Figure B.1 Field cooled MO image of B1s-b(10°).

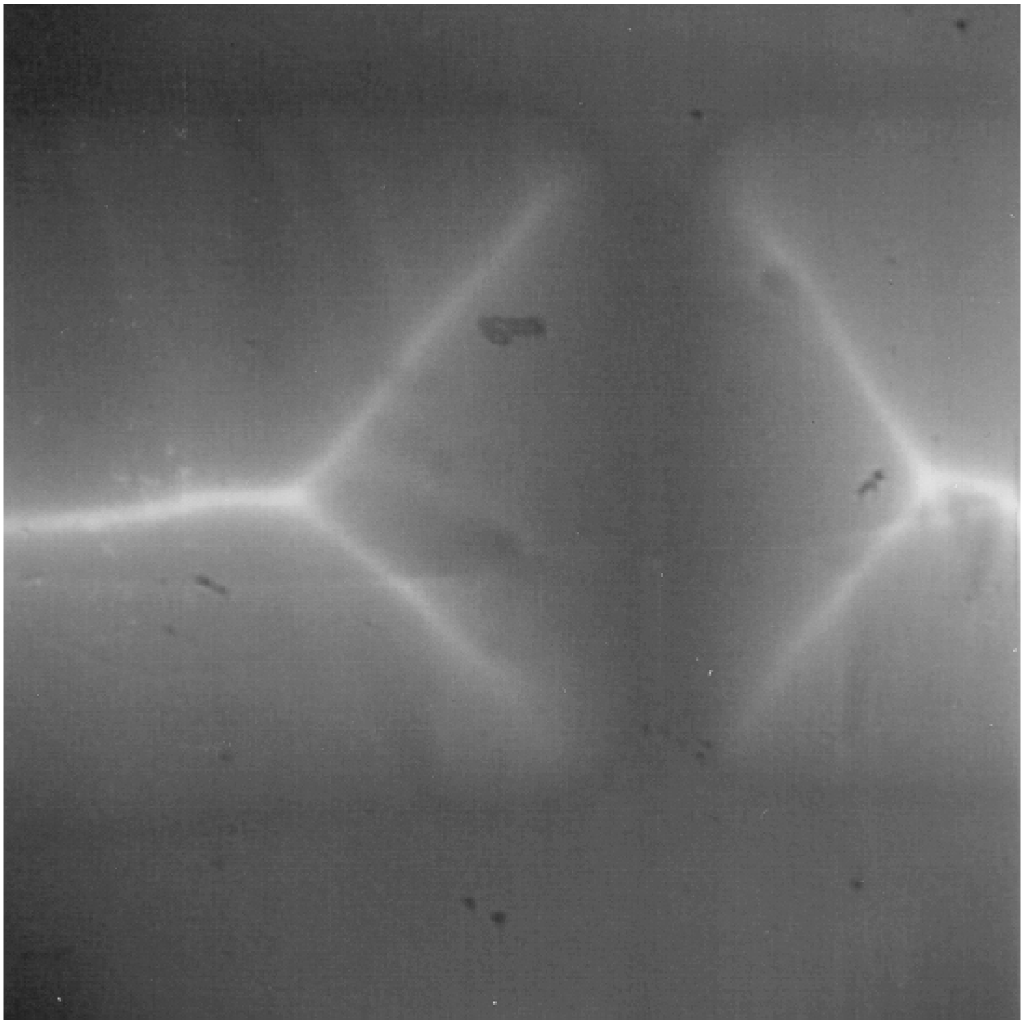

Figure B.2 Field cooled MO image of B2s-b(15°).

Electromagnetic Measurements

The 10° bicrystal, B1s-b(10°), was the first to be patterned and measured by transport. Figure B.3 shows the intergranular resistance versus temperature, where the T_c across the GB is about 87 K. The superconducting transition is broad and smooth, with no evidence of the distinct "foot" below the intragranular T_c characteristic of weakly coupled YBCO grain boundaries. The resistance versus temperature for the 15° bicrystal, B2s-b(15°) is shown in Figure B.4. This intragranular measurement shows no superconducting transition above 74 K.

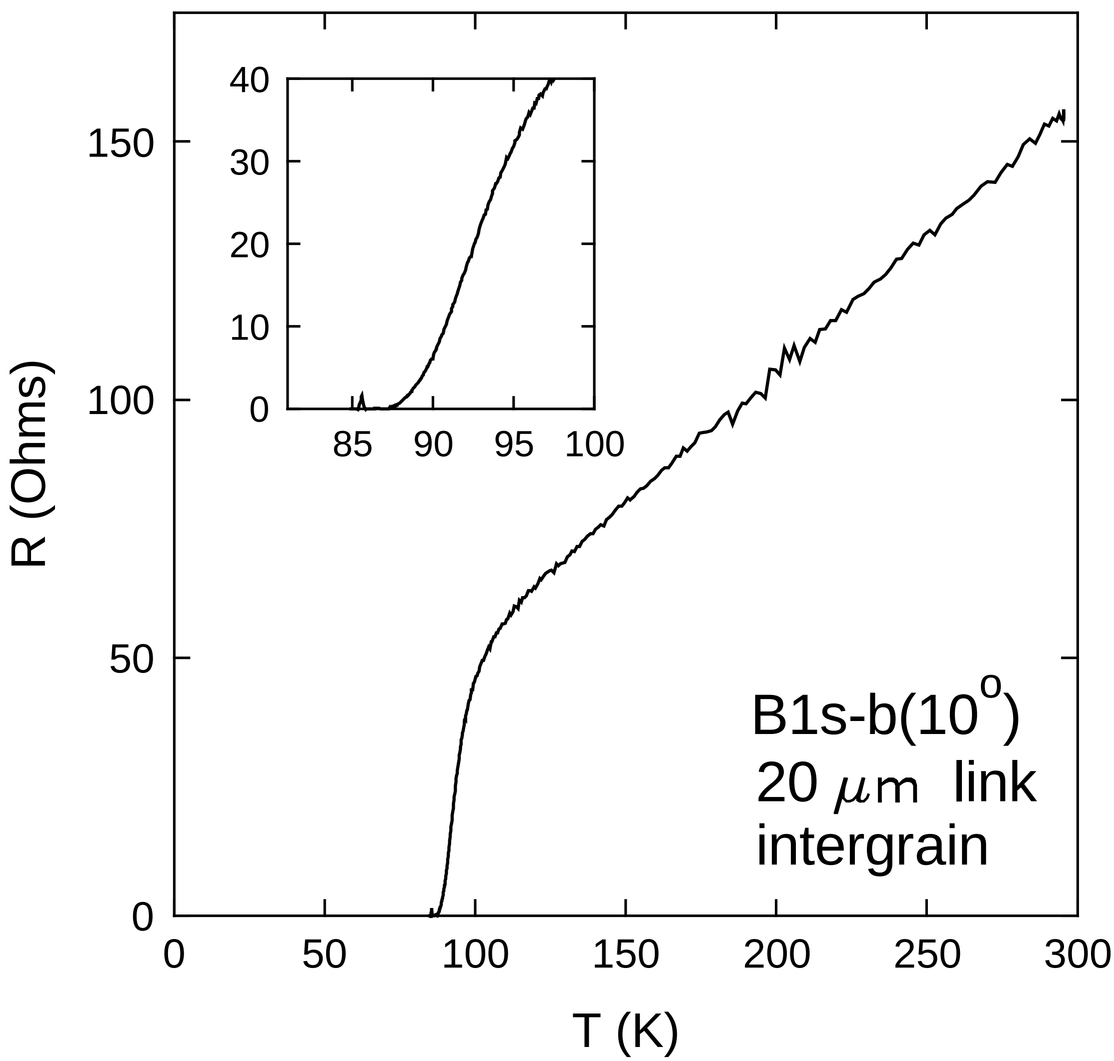

Figure B.3 Resistance versus temperature across an intergranular link of B1s-b(10°).

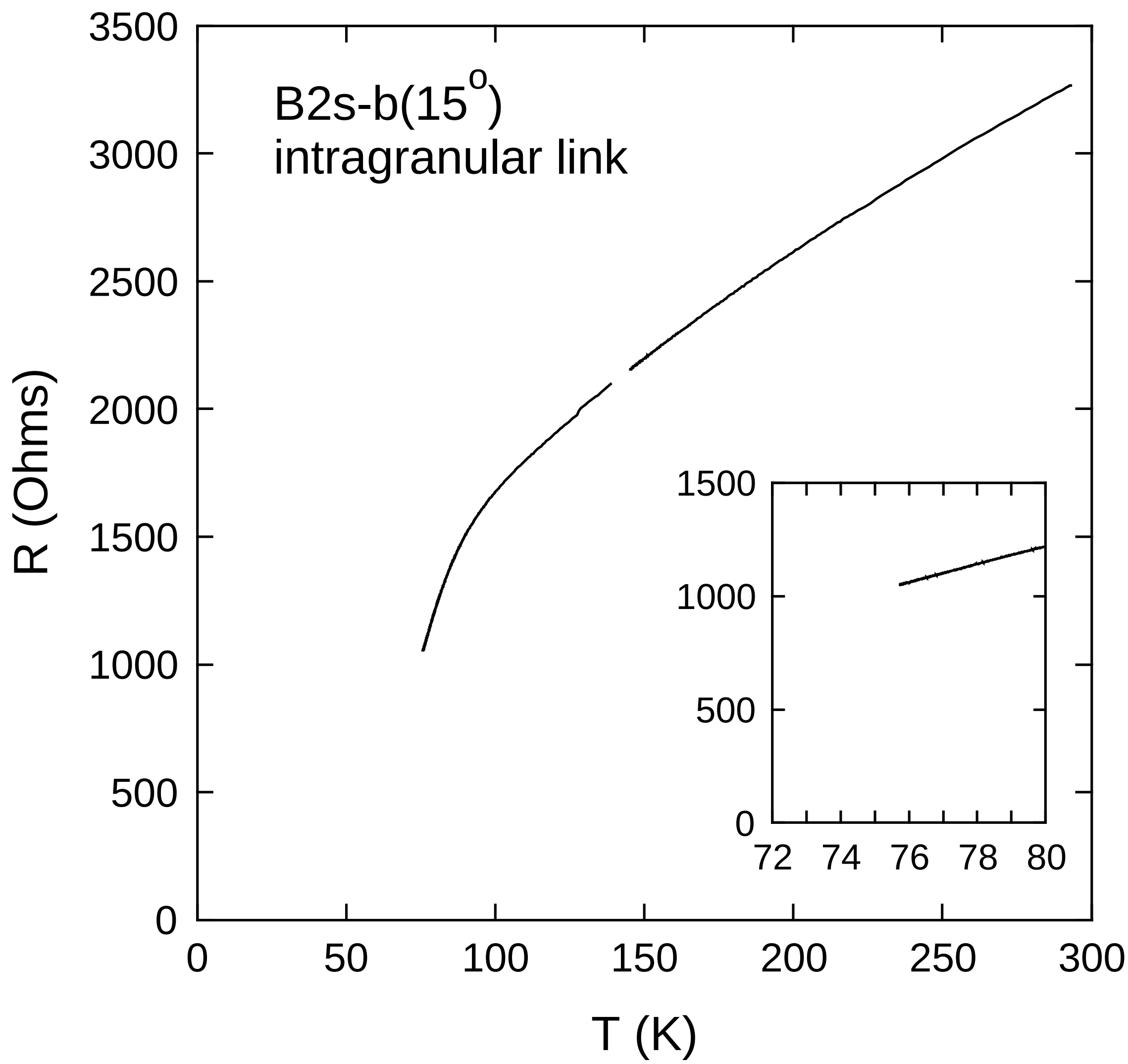

Figure B.4 Resistance versus temperature across the intragranular link of B2s-b(15°).

Figures B.5 and B.6 show the zero field V-J intergranular characteristics are at 77 K and 84 K, respectively. These measurements were done by using the ac+dc technique discussed in Chapter 3, so that one also obtains the differential resistance curve, dV/dI versus J. One important point relates to the shape of the dV/dI versus J curve shown in Figures B.5(b) and B.6(b). At 77 K, the dV/dI curve has shape reminiscent of flux-flow behavior, with no peaks in dV/dI above J_b. At 84 K, there are small, broad peaks in dV/dI above J_b, and these peaks are characteristic of Josephson coupling. This suggests that strongly coupled channels exist across the 10° $Bi_2Sr_2CaCu_2O_x$ bicrystal grain boundary, based upon previous low field experiments on YBCO.

In studies of 10° YBCO bicrystals [64], where this same evolution of shape with temperature was observed, it was argued that these changes are due to the increasing size of the coherence length, ξ, with temperature. At lower temperatures, ξ is small with respect to the size of any strongly coupled channels and mainly flux-flow, strongly coupled behavior is observed. As the temperature increases, so does ξ, and the junction starts to behave more and more like an ideal Josephson junction. In the YBCO case, it was only possible to see this cross-over between flux-flow and Josephson-like V-I curves in 7° and 10° thin film bicrystals, as at higher misorientation angles no flux flow behavior was observed even at 20 K.

This explanation of the flux flow V-I curve in YBCO was confirmed by high field experiments determining H*, which showed that any strongly coupled channels across the grain boundary closed between 10° and 15° at 77 K. So even though the 10° $Bi_2Sr_2CaCu_2O_x$ bicrystal had a zero field $J_b(77K) = 7.5 \times 10^4$ A/cm^2, almost an order of magnitude smaller than the corresponding YBCO junctions, the same type of channel conduction appears to exist. Unfortunately, it was not possible to verify this in high magnetic fields because of the extreme environmental sensitivity of these $Bi_2Sr_2CaCu_2O_x$ films.

In Figure B.7, extended V-J curves for the 10° $Bi_2Sr_2CaCu_2O_x$ bicrystal are shown in fields ranging from 0 to 11 Tesla. The data was taken at 26 K, as there was no supercurrent at 77 K, and the very weakly coupled nature of the boundary even at this temperature is apparent. This data was taken after that shown in Figure B.5 and B.6, and subsequent resistance versus temperature measurements confirmed the grain boundary was no longer superconducting above 67 K.

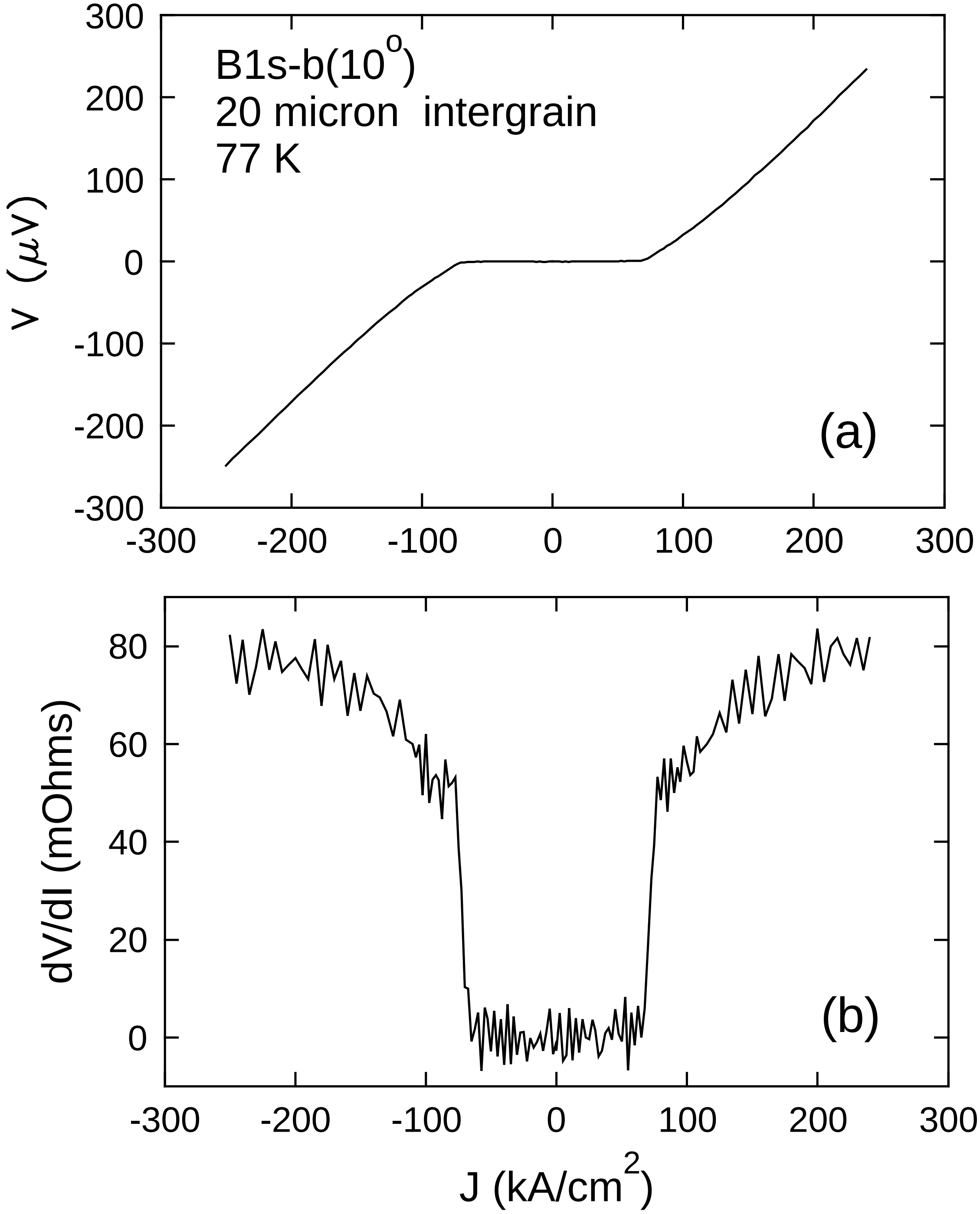

Figure B.5 V - J and dV/dI - J across a 20 μm intergranular link in B1s-b(10°) in zero applied field at 77 K.

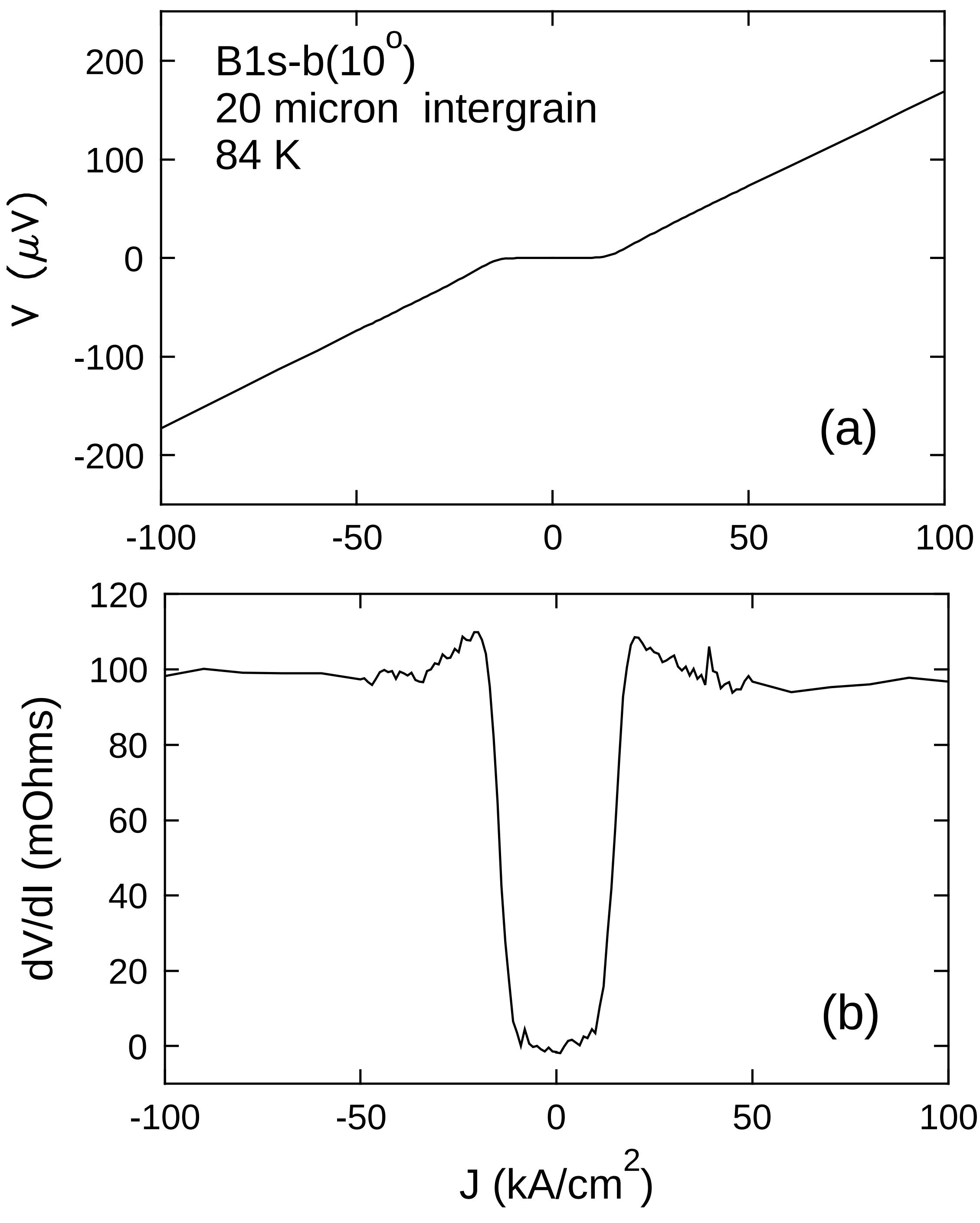

Figure B.6 V - J and dV/dI - J across a 20 μm intergranular link in B1s-b(10°) in zero applied field at 84 K.

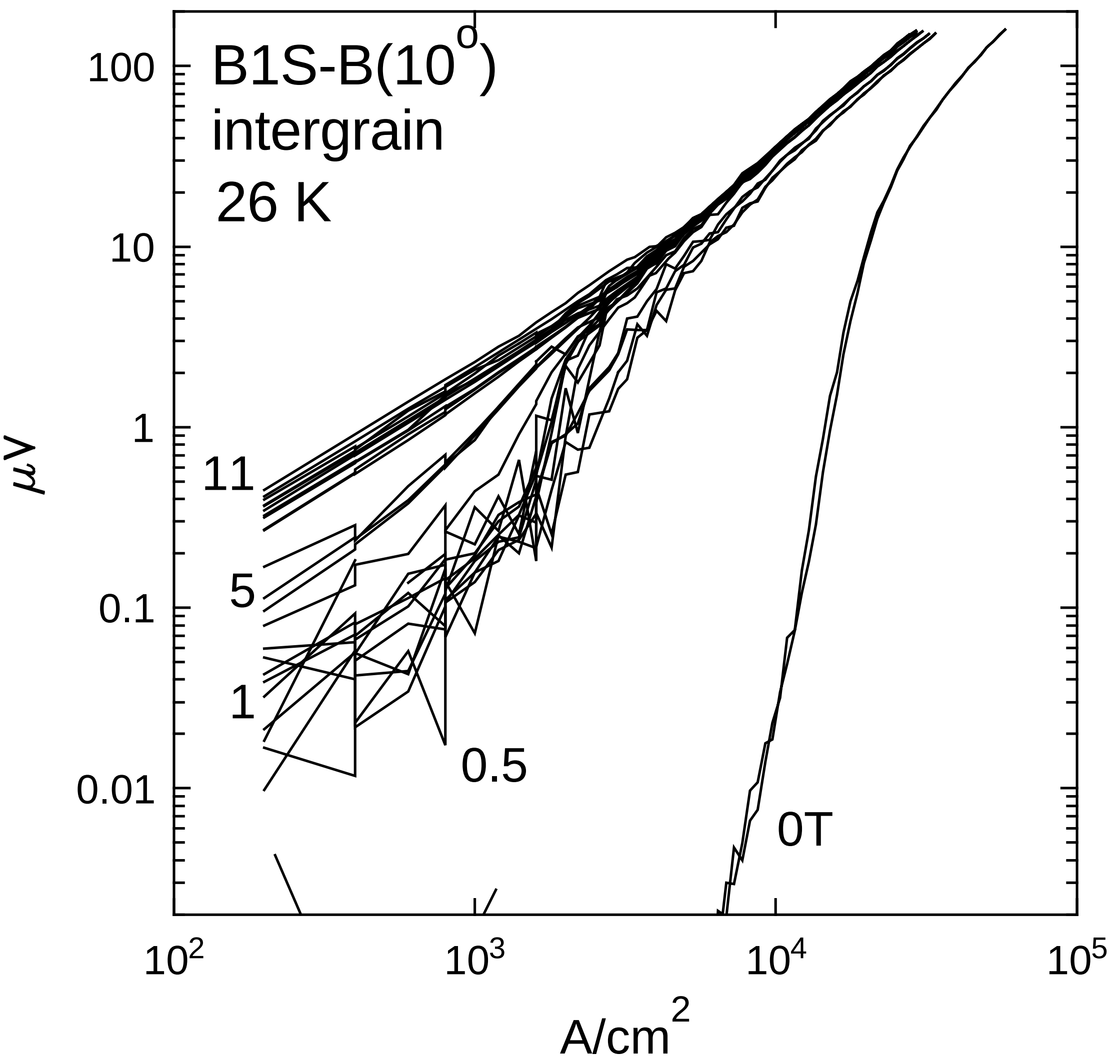

Figure B.7 Extended V-J curves for an intergranular link in B1s-b(10°) at 26 K and fields between 0 and 11 Tesla.

This sensitivity of the $Bi_2Sr_2CaCu_2O_x/SrTiO_3$ epitaxial films to the environment is in contrast to the relatively robust behavior of bulk scale single crystals and polycrystalline tapes of $Bi_2Sr_2CaCu_2O_x$. Evidence of damage is also seen by the distinct contrast in the MO image between the gold-covered and uncovered regions of the films. One should note that this different MO contrast due to gold was not observed in YBCO.

Despite these problems, there is evidence that good quality thin film 10° grain boundaries of $Bi_2Sr_2CaCu_2O_x$ consists of strongly and weakly coupled channels in parallel, and this model of low angle grain boundary behavior is applicable to both YBCO and $Bi_2Sr_2CaCu_2O_x$.

1 D. Dimos, P. Chaudhari, and J. Mannhart, Phys. Rev. B, **41**, 4038-4049, (1990); D. Dimos, P. Chaudhari, J. Mannhart, and F.K. LeGoues, Phys. Rev. Lett., **61**, 219, (1988); J. Mannhart, P. Chaudhari, D. Dimos, C.C. Tsui, and T.R. McGuire, Phys. Rev. Lett. **61**, 2476, (1988).

2 M.T. Naus et al., submitted to IEEE Transactions.

3 B. Batlogg, Physics Today, p48, June 1991.

4 Y. Iijima, N. Tanabe, O. Kohno, Y. Ikeno, Appl. Phys. Lett. **60**, 769 (1992).

5 R.P. Reade, P. Berdahl, R.E. Russo, S.M. Garrison, Appl. Phys. Lett. **61**, 2231 (1992).

6 X.D. Wu, S.R. Foltyn, P. Arendt, J. Townsend, C. Adams, I.H. Campbell, P. Tiwari, Y. Coulter, D.E. Peterson, Appl. Phys. Lett. **65**, 1961 (1994).

7 S.R. Foltyn, P.N. Arendt, X.D. Wu, W.R. Blumenthal, J.D. Cotton, J.Y. Coulter, W.L. Hults, H.F. Safar, J.L. Smith, and D.E. Peterson, in Extended Abstracts, 1995 International Workshop on Superconductivity, June 18-21, 1995.

8 A. Goyal, D.P. Norton, J.D. Budai, M. Paranthaman, E.D. Specht, D.M. Kroeger, D.K. Christen, Q. He, B. Saffian, F.A. List, D.F. Lee, P.M. Martin, C.E. Klabunde, E. Hartfield, and V.K. Sikka, Appl. Phys. Lett., **69**, 1795, (1996).

9 Z.G. Ivanov, P.A. Nilsson, D. Winkler, J.A. Alarco, G. Brorsson, T. Claeson, E.A. Stepantsov, and A.Ya. Tzalenchuk, Superconducting Sci. and Tech., **4,** 439-441, (1991).

10 Z.G. Ivanov, P.A. Nilsson, D. Winkler, J.A. Alarco, T. Claeson, E.A. Stepantsov and A.Ya. Tzalenchuk, Appl. Phys. Lett. **59**, 3030, (1991).

11 D. Winkler, Y.M. Zhang, P.A. Nilsson, E.A. Stepantsov and T. Claeson, Phys. Rev. Lett. **72**, 1260, (1994).

12 R. Gross, *Interfaces in High-T_c Superconducting Systems*, S.L. Shindé and D.A. Rudman, eds., Springer-Verlag, N.Y. (1994), 176-209.

13 H. Suzuki, H. Kurasawa, J. Chen, Y. Hirotsu, K. Nakajima, T. Yamashita, H. Myoren, and Y.Osaka, Superconducting Sci. and Tech. **4**, 479-481, (1991).

14 T. Amrein, L. Schultz, B. Kabius, and K. Urban, Phys. Rev. B, **51**, 6792, (1992).

15 M. Kawasaki, E. Sarnelli, P. Chaudhari, A. Gupta, A. Kussmaul, J. Lacey, and W. Lee, Appl. Phys. Lett. **62**, 417, (1993).

16 T. Nabatame, S. Koike, O.B. Hyun, I. Hirabayashi, H. Suhara, and K. Nakamura, Appl. Phys. Lett. **65**, 776, (1994).

17 H. Suhara, T. Nabatame, O.B. Hyun, S. Koike, and I. Hirabayashi, Superconducting Sci. and Tech. **8**, 443-447, (1995).

18 E. Sarnelli, P. Chaudhari, W.Y. Lee, and E. Esposito, Appl. Phys. Lett. **65**, 362 (1994).

19 B.H. Moeckly, D.K. Lathrop, and R.A. Buhrman, Phys. Rev. B, **47**, 400, (1993).

20 D.K. Lathrop, B.H. Moeckly, S.E. Russek, and R.A. Buhrman, Appl. Phys. Lett., **58**, 1095, (1991).

21 E.A. Early, A.F. Clark, and K. Char, Appl. Phys. Lett., **62**, 3357, (1993).

22 A.H. Miklich, J. Clarke, K. Char, and M.S. Colclough, Appl. Phys. Lett. **59**, 1899, (1992).

23 R. Gross and B. Mayer, Physica C, **180**, 235, (1991).

24 R. Gross, HTSED Workshop 1994, May 26-28, 1994 in Whistler, British Columbia, Canada.

25 A. Marx, U. Fath, L. Alff, and R. Gross, Appl. Phys. Lett., **67**, 1929, (1995).

26 M. Däumling, E. Sarnelli, P. Chaudhari, A. Gupta, J. Lacey, Appl. Phys. Lett. **61**, 1355, (1992).

27 E. Sarnelli, P. Chaudhari, J. Lacey, Appl. Phys. Lett. **62**, 777 (1993).

28 O.M. Fröhlich, H. Schulze, A. Beck, B. Mayer, L. Alff, R. Gross, R.P. Huebener, Appl. Phys. Lett. **66**, 2289, (1995).

29 S.E. Babcock, X.Y. Cai, D.L. Kaiser, and D.C. Larbalestier, Nature, **347**, 167-169, (1990)

30 D.C. Larbalestier, S.E. Babcock, X.Y. Cai, M.B. Field, Y. Gao, N.F. Heinig, D.L. Kaiser, K. Merkle, L.K. Williams, and N. Zhang, Physica C, **185-189**, 315-320, (1991).

31 C.B. Eom, A.F. Marshall, Y. Suzuki, B. Boyer, R.F.W. Pease, and T.H. Geballe, Nature, **353**, 544, (1991); C.B. Eom, A.F. Marshall, Y. Suzuki, T.H. Geballe, B. Boyer, R.F.W. Pease, R.B. van Dover, and J.M. Phillips, Phys. Rev. B, **46**, 11902-11913 (1992).

32 X.Y. Cai, I F. Tsu et al., in preparation.

33 M.F. Chisholm, S.J. Pennycook, Nature, **351**, 47 (1991).

34 Y. Gao, K.L. Merkle, G. Bai, H.L.M. Chang, and D.J. Lam, Ultramicroscopy, **37**, 326-340, (1991); Physica C, **174**, 1-10, (1991).

35 E.Z. Meilikhov, to appear in J.E.T.P. (1996).

36 J. Evetts, ed. *Concise Encyclopedia of Magnetic and Superconducting Materials*, Pergamon Press, Ltd., N.Y., 1992.

37 S.E. Babcock and D.C. Larbalestier, Appl. Phys. Lett. **55**, 393, (1989); S.E. Babcock and J.L. Vargas, Annu. Rev. Mater. Sci., **25**, 193-222, (1995).

38 Na Zhang, Masters thesis, University of Wisconsin-Madison (1995).

39 S.E. Babcock, X.Y. Cai, D.C. Larbalestier, D.H. Shin, N. Zhang, H. Zhang, D.L. Kaiser and Y. Gao, Physica C, **227**, 183-196, (1994).

40 I F. Tsu, S.E. Babcock, and D.L. Kaiser, J. of Mat. Res., **11**, 1383-1387, (1996).

41 J.A. Alarco, E. Olsson, Z.G. Ivanov, P.A. Nilsson, D. Winkler, E.A. Stepantsov and A.Ya. Tzalenchuk, Ultramicroscopy, **51**, 239, (1993).

42 C. Traeholt, J.G. Wen, H.W. Zandbergen, Y. Shen, and J.W.M. Hilgenkamp, Physica C, **230**, 425, (1994).

43 T. Amrein, L. Schultz, B. Kabius, and K. Urban, Phys. Rev. B, **51**, 6792, (1995).

44 D.J. Miller, T.A. Roberts, J.H. Kang, J. Talvacchio, D.B. Buchholz, and R.P.H Chang, Appl. Phys.
Lett., **66**, 2561, (1995).

45 I Fei Tsu, Ph.D. thesis, University of Wisconsin-Madison, (1996).

46 M. Ece, E.G. Gonzalez, H.U. Habermeier, and B. Oral, J. Appl Phys. **77**, 1646-1653, (1995).

47 M.G. Norton and C.B. Carter, in *Interfaces in High-T_c Superconducting Systems*, eds. S.L. Shindé and D.L. Rudman, Springer-Verlag, NY, 1994.

48 I.D. Raistrick and M. Hawley, in *Interfaces in High-T_c Superconducting Systems*, eds. S.L. Shindé and D.L. Rudman, Springer-Verlag, NY, 1994.

49 O. Eibl and B. Roas, J. Mater. Res., **5**, 2620, (1990).

50 K. Verbist, A.L. Vasiliev and G. Van Tendeloo, Appl. Phys. Lett., **66**, 1425, (1995); K. Verbist, A. Kühle, A.L. Vasiliev, Physica C, **269**, 131-138, (1996).

51 Jeanne Ayotte, private communication.

52 D.L. Kaiser, F. Holtzberg, B.A. Scott, and T.R. McGuire, Appl. Phys. Lett. **51**, 1040-1042, (1987).

53 D.L. Kaiser, F. Holtzberg, M.F. Chisholm, and T.K. Worthington, J. of Crystal Growth, **85**, 593-598 (1987).

54 J.R. LaGraffe and D.L. Payne, Phys. Rev. B, **47**, 3380-3390, (1993).

55 J.R. LaGraff, and D.A. Payne, Physica C, **212**,470-477, (1993).

56 J.L. Vargas and D.C. Larbalestier, Appl. Phys. Lett. **60**, 1741-1743, (1992).

57 H.C. Montgomery, J. of Appl. Phys. **42**, 2971-2979, (1971).

58 L.J. van der Pauw, Phillips Research Reports, **16**, 301-306, (1961).

59 J.D. Wasscher; Philips Research Reports, **16**, 301-306, (1961).

60 J.M. Phillips, J. Appl. Phys. **79**, 1829-1848, (1996).

61 R. Gross, P.Chaudhari, D.Dimos, A.Gupta and G.Koren, Phys.Rev.Lett. **64**, 228, (1990)

62 A. Barone and G. Paterno, *Physics and Applications of the Josephson Effect*, John Wiley and Sons, N.Y. 1982.

63 J.M. Phillips, J. Appl. Phys., **79**, (1996), 1829-1848.

64 R.D. Redwing et al., "Observation of Strong to Josephson Coupled Transition in Low Angle [001] Tilt $YBa_2Cu_3O_{7-x}$ Bicrystal Junctions", in preparation.

65 C.S. Owen and D.J. Scalapino, Phys. Rev. **164**, (1967), 538.

66 T. Amrein, L. Schultz, B. Kabius, and K. Urban, Phys. Rev. B, **51**, (1995),6792-6795.

67 X.Y. Cai, M.B. Field, N.F. Heinig, H. Zhang, N. Zhang, S.E. Babcock, D.L. Kaiser, and D.C. Larbalestier, Extended abstracts at the ISTEC conference, Hakodate, Japan, June 1993.

68 X.Y. Cai, I F. Tsu et al., in preparation.

69 J.L. Vargas, S.E. Babcock, N. Zhang, N.F. Heinig, X.Y. Cai, D.C. Larbalestier, and D.L. Kaiser, "Periodic Oscillations in the Excess Copper Concentration along Grain Boundaries in Flux-Grown $YBa_2Cu_3O_{7-x}$ Bicrystals", in preparation.

70 X.Y. Cai, private communication.

71 N.F. Heinig, R.D. Redwing, I F. Tsu, A. Gurevich, J.E. Nordman, S.E. Babcock, and D.C. Larbalestier, Appl. Phys. Lett. **69**, 577, (1996).

72 *Low Level Measurements, 4th ed.*, Keithley Instruments, Inc., 1992, Cleveland, Ohio, pp3-17.

73 A.A. Polyanskii, A. Gurevich, A.E. Pashitski, N.F. Heinig, R.D. Redwing, J.E. Nordman, and D.C. Larbalestier, Phys. Rev. B, **53**, 8687-8697, (1996).

74 Laura A. Bonney, Ph.D. thesis, University of Wisconsin-Madison, (1994).

75 R. Wördenweber, Phys. Rev. B, **46**, 3076-3083, (1992); R. Wördenweber, Cryogenics, **32**, 1098, (1992).

76 Q. Li, H.J. Weismann, M. Suenaga, L. Motowidlo, and P. Haldar, Phys. Rev. B **51**, 701, (1995).

77 V. Bekeris, R. Schifini Gladchtein, H. Ferrari, G. Polla, and F. de la Cruz, "Inhomogenous current density transport properties in isotropic HTS", Czechoslovak J. of Physics, **46**, 1549, Suppl. S3, (1996).

78 R.H. Koch, V. Foglietti, W.J. Gallagher, G. Koren, A. Gupta, M.P.A. Fisher, Phys. Rev. Lett. **63**, 1511, (1989).

79 H. Yamasaki, K. Endo, S. Kosaka, M. Umeda, S. Yoshida, K. Kajimura, Cryogenics **35**, 263, (1995).

80 G. Blatter, M.V. Feigel'man, V.B. Geshkenbein, A.I. Larkin, and V.M. Vinokur, Rev. Mod. Phys., **66**, p1137, 1254, (1994).

81 R.J. Soulen, Jr., T.L. Francavilla, W.W. Fuller-Mora, M.M. Miller, C.J. Joshi, W.L. Carter, A.J. Rodenbush, M.D. Manlief, and D. Aized, Phys. Rev. B, **50**, 478-487, (1994).

82 H.S. Edelman, Ph.D. thesis, University of Wisconsin-Madison (1995).

83 J.A. Parrell, D.C. Larbalestier, G.N. Riley, Jr., Q. Li, R.D. Parrella, and M. Teplitsky, to appear in Appl. Phys. Lett., Nov. (1996).

84 H. Hilgenkamp, J. Mannhart, and B. Mayer, Phys. Rev. B, **53**, 14586, (1996).

85 U. Welp, W.K. Kwok, G.W. Crabtree, K.G. Vandervoort, and J.Z. Liu, Phys. Rev. Lett., **62**, 1908, (1989).

86 P.B. Alers, Phys. Rev., **105**, 104, (1957).

87 M.V. Indenbom, N.N. Kolesnikov, M.P. Kulakov, I.G. Naumenko, V.I. Nikitenko, A.A. Polyanskii, N.F. Vershinin, and V.K. Vlasko-Vlasov, Physica C, **166**, 486, (1990).

88 M.R. Koblischka and R.J. Wijngaarden, Supercond. Sci. Technol., **8**, 199, (1995).

89 M. Turchinskaya, D.L. Kaiser, F.W. Gayle, and A. Roytburd, Physica C, **221**, 62-70, (1994).

90 J.L. Wang, I F. Tsu, X.Y. Cai, R.J. Kelley, M.D. Vaudin, S.E. Babcock, and D.C. Larbalestier, J. Mater. Res., **11**, 868, (1996).